This is to certify that the
dissertation entitled

DYNAMIC-ABSORPTION CONTOURS: ANALYSIS OF WAVE-PACKET MOTION ON GROUND-STATE AND EXCITED-STATE POTENTIAL ENERGY SURFACES

presented by

ELIZABETH CARSON GOLOVICH

has been accepted towards fulfillment
of the requirements for the

Ph.D. degree in Physical Chemistry

Warren F. Beck
Major Professor's Signature

1 March 2005
Date

DYNAMIC-ABSORPTION CONTOURS: ANALYSIS OF WAVE-PACKET MOTION ON GROUND-STATE AND EXCITED-STATE POTENTIAL ENERGY SURFACES

By

Elizabeth Carson Golovich

A DISSERTATION

Submitted to
Michigan State University
in partial fulfillment of the requirements
for the degree of

DOCTOR OF PHILOSOPHY

Department of Chemistry

2005

ABSTRACT

By

Elizabeth Carson Golovich

A variety of biological molecules involved in photochemical reactions, such as rhodopsin and the photosynthetic reaction center, are characterized by resonance Raman spectroscopy. This technique provides a great deal of information on the ground-state and excited-state potential-energy surfaces, but this approach has limitations. Only information from the Franck-Condon region can be obtained. Additionally, for molecules that have small Stokes shifts, the ground-state depletion and stimulated-emission signals overlap. This prevents the ability to distinguish between ground-state and excited-state vibrational coherence solely by probe wavelength.

Using ultrafast dynamic-absorption spectroscopy, we have determined a new approach to distinguish the phase relationship between the coherent wave-packet motions on the ground-state and excited-state potential-energy surfaces. Analysis of contour surfaces can provide information beyond the Franck-Condon region. We use this approach to examine the ground-state and excited-state vibrational coherence of two carbocyanine dyes, IR144 and DTTCI.

The results presented in this dissertation show that the structures of the carbocyanine dyes are not static after excitation, as previously thought in solvation-dynamics studies. We propose that the vibrational modes observed in the vibrational coherence from IR144 and DTTCI obtain Raman activity through mixing of nearby excited states. Vibrational coherence with rapidly-damped and long-lived components is observed. The origin of the two damping time scales is proposed.

TABLE OF CONTENTS

LIST OF TABLES

LIST OF FIGURES

INTRODUCTION

A variety of biological molecules involved in photochemical reactions, such as rhodopsin and the photosynthetic reaction center, are characterized by resonance Raman spectroscopy. This technique provides a great deal of information on the ground-state and excited-state potential-energy surfaces, but this approach has limitations. Only information from the Franck-Condon region can be obtained. Additionally, for molecules that have small Stokes shifts, the ground-state depletion and stimulated-emission signals overlap. This prevents the ability to distinguish between ground-state and excited-state vibrational coherence solely by probe wavelength.

Using ultrafast dynamic-absorption spectroscopy, we have determined a new approach to distinguish the phase relationship between the coherent wave-packet motions on the ground-state and excited-state potential-energy surfaces. A contour surface is obtained from a set of single-wavelength dynamic-absorption transients. Visual analysis of the contour surfaces allows for simple separation of ground-state and excited-state vibrational coherence signals. We use this approach to examine the ground-state and excited-state vibrational coherence of two carbocyanine dyes, IR144 and DTTCI. These dyes were chosen because of their similarity in structure to retinal.

The dissertation is organized as follows:

Chapter 1 begins with a short discussion of important biological reactions. Followed by an explanation of vibrational coherence. A comparison of experimental techniques used to examine wave-packet motions is next. Finally, the model experimental systems are presented.

In Chapter 2, a detailed description of the laser system used in the experiments discussed in this dissertation will be presented. The modified Mach-Zehnder interferometer with novel signal-detection mechanism will be discussed. The chapter concludes with a discussion of signal processing.

In Chapter 3, a new approach to distinguish the phase relationship between coherent wave-packet motions on ground- and excited-state potential-energy surfaces using contour surfaces is discussed. This method is used to examine the ground-state and excited-state vibrational coherence from IR144 in methanol.

In Chapter 4, the dynamic-absorption spectra of DTTCI in methanol are presented. A comparison of the ground- and excited-state vibrational coherence is made and many new peaks are observed in the excited state. Polarization experiments help to show that the observed vibrational modes gain Raman activity through the Albrecht *B*-term mechanism, mixing to nearby excited states.

In Chapter 5, the results from DTTCI in various polar solvents are presented. Vibrational coherence with two different damping time scales is observed from DTTCI in all three solvents. The rapidly-damped vibrational coherence of DTTCI in each solvent is separated from the long-lived vibrational coherence. The rapidly-damped vibrational coherence is solvent dependent. The differences observed from the ground-state and excited-state spectra are compared to results observed from the solvated electron.

CHAPTER 1

INTRODUCTION

1.0 Importance of Photochemical Reactions

1.0.1 Charge-Transfer Reactions in the Photosynthetic Reaction Center

An intense topic of research is that of the primary charge-separation photochemistry exhibited by the photosynthetic reaction center after the absorption of a photon.[1-3] The X-ray crystal structures of the reaction centers of *Rhodopseudomonas viridis* (see figure 1.1) and *Rhodobacter sphaeroides* have been known for almost fifteen years. Reaction centers have two chromophore branches (L and M) that can serve as electron acceptors for the primary electron donor, P, which is a strongly coupled pair of bacteriochlorophyll (Bchl) molecules. These branches are found alongside the vector between P and the non-heme Fe ion (see figure 1.2). It is not fully understood how the charge separation events are initiated at P or why initial electron-transfer reactions only occur along one branch (L). There is good reason to believe that the protein-derived surroundings of P and of the adjacent monomeric Bchls B_L and B_M contribute to the breaking of symmetry that results in the charge separation reaction in a given direction. Bchl dimers may be favored as primary electron donor structures in reaction centers due to their charge-transfer properties, which might contribute to the high quantum efficiency and spatial directionality of the initial electron-transfer events.

1.0.2 Isomerization Reactions in Rhodopsin

Another popular topic of research is that of the isomerization reaction that occurs in the visual pigment, rhodopsin.[5-7] Rhodopsin is a seven α-helical membrane-bound

Figure 1. The photosynthetic reaction center from *Rhodopseudomonas viridis*.[4]

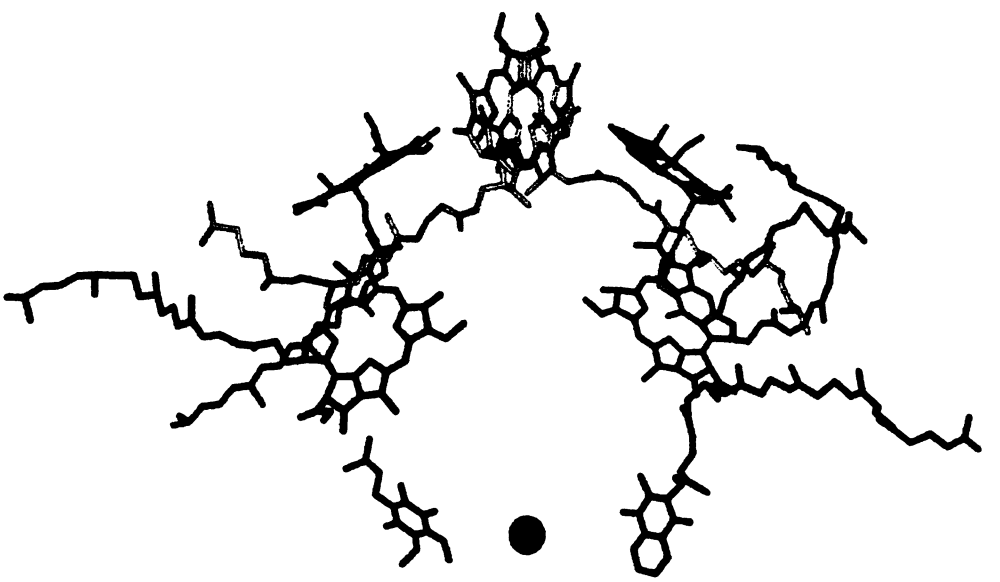

Figure 2. Chromophores in the reaction center from *Rhodopseudomonas viridis*.[4]

protein (see figure 1.3). After optical excitation, the chromophore in rhodopsin, 11-*cis*-retinal is converted to the all-*trans* photoproduct in a highly efficient isomerization reaction.

1.1 Approach to the Problem

Examination of vibrational modes coupled to optically driven electronic transitions can give information on the dynamics of photochemical reactions. It has been suggested that low-frequency protein motions may play an important role in the observed dynamics.[7,9] Below are the theory and experimental techniques necessary for such studies.

1.1.1 Wave-Packet Theory

The development of lasers capable of producing femtosecond pulses, allows one to excite samples using pulses that are short when compared to a vibrational period. Due to the Heisenberg Uncertainty principle, a temporally short pulse encompasses a broad range of frequencies which can excite molecules within a distribution of instantaneous nuclear geometries. When a vibrationally abrupt pulse is used for excitation, molecules do not have time to move into or out of the range of internuclear geometries sampled by the pulse[10] which results in the formation of a coherent superposition of states or vibrational wave packets.[11]

Vibrational wave packets have been described both quantum mechanically and semi-classically. This discussion of vibrational wave packets will be constrained to the semi-

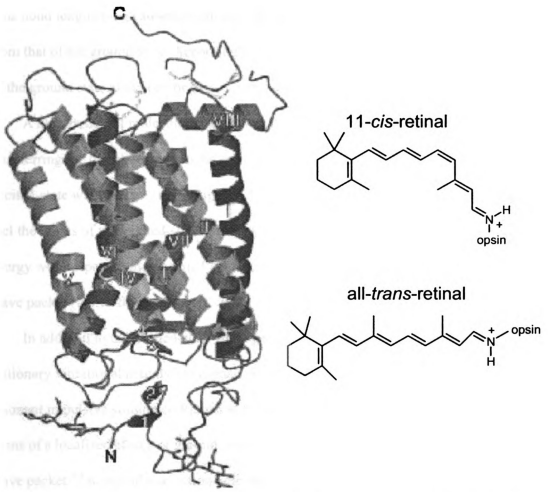

Figure 3. Transmembrane protein rhodopsin (right) shown with retinal chromophore in both *cis* and *trans* configurations (left).[8]

classical description by Lee and Heller,[12-14] as the classical description is often easier to visualize conceptually.

In a system where a $\pi \rightarrow \pi^*$ transition occurs, an electron is moved from a bonding orbital to an antibonding orbital, lengthening of one or more bonds in the excited state. This bond lengthening causes the equilibrium structure of the excited state to be different from that of the ground state. Accordingly, the excited-state surface is displaced from that of the ground state along one or more normal coordinates as illustrated in figure 1.4.[12-14]

A distribution of molecules within the sample interact with the pump field, vertically transferring the distribution from the ground state to the excited-state surface, creating an excited-state wave packet (t=1 in figure1.4). The newly formed wave packet will begin to feel the forces of the excited-state surface and will move in an attempt to minimize its energy with respect to their excited-state geometry. This gives rise to a moving vibrational wave packet (t=3 in figure1.4).

In addition to the excited-state wave packet, short pulses also establish non-stationary vibrational activity via Raman mechanisms.[10,15] Ground-state wave packets, or resonant impulsive stimulated Raman scattering (RISRS), have often been explained in terms of a localized bleach or ground-state hole that is the complement of the excited-state wave packet.[10] A second interaction with the pump pulse transfers part of the excited-state wave packet back to the ground-state surface at a displaced geometry (t=2 in figure1.4). Since the displaced wave packet is not at equilibrium with respect to the ground-state geometry, the interaction creates a ground-state wave packet that evolves in time according to the forces arising from the ground-state potential-energy surface (t=3 in figure1.1).[15]

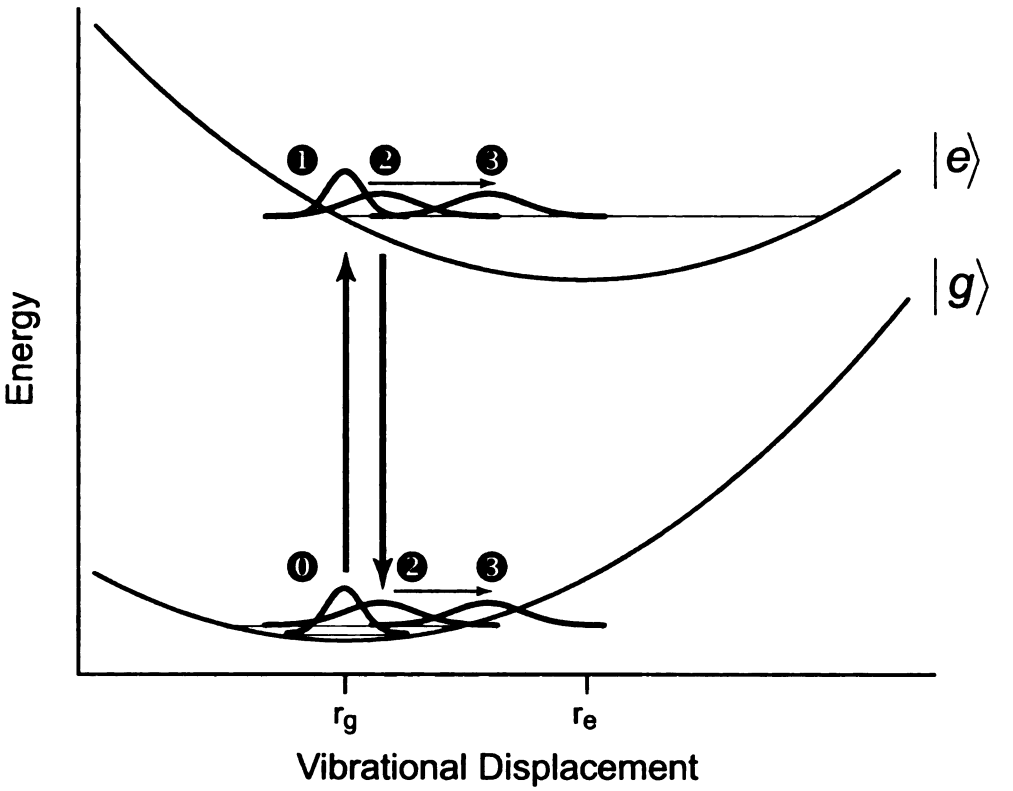

Figure 4. Excited-state and ground-state coherent wave-packet motion in the dynamic-absorption experiment. The excited-state and ground-state potential-energy surfaces are drawn as parabolas that are displaced with respect to a generalized multimode coordinate; r_g and r_e mark the equilibrium ground-state and excited-state geometries, respectively. Thick arrows represent the resonant pump-laser field; thin arrows show the direction that the wave packets evolve during the first passage on the two surfaces. The numbers indicate event times, starting with the ground-state probability density, creation of the excited-state wave packet by the pump field, creation of the ground-state wave packet by the pump field, and evolution during the first vibration.

Vibrational wave packets manifest in time-domain experiments, such as pump–probe and fluorescence spectroscopies, as recurring oscillations. These oscillations have periods which correspond to displaced vibrational modes excited by the electronic transition. As the internuclear distances oscillate about the equilibrium geometries of the ground and excited states, the energy gap between the ground- and excited-state surfaces modulates causing the energies absorbed by the molecule to modulate at a given instant.[10,16] This modulation of the absorption spectrum manifests as cosine-like oscillations detected in the time-domain signal.[16] An analysis of the oscillations yields the frequencies of the vibrational modes that are perturbed as a result of the optical excitation.[16] Because of the information content obtained, these experiments are often described as the time domain analogue of resonance Raman spectroscopy.[17]

1.1.2 Resonance Raman Spectroscopy

Resonance Raman spectroscopy is an effective technique for studying the structure of biological molecules. The vibrational frequencies give specific information about geometry and electronic structure of the chromophore in the ground state while the intensities of resonance Raman lines give information about the symmetry, equilibrium geometry and dynamics of the chromophore in the excited state.[18] In order for an electronic transition to have resonance Raman intensity, there must be a significant shift of the excited-state potential minimum along the normal coordinates. These Franck-Condon active modes are totally symmetric and are considered to be of Albrecht *A*-term origin. Transitions of Albrecht *B*-term origin are non-totally symmetric modes which receive resonance Raman intensity through vibronic mixing to nearby excited states.[19,20] The

portion of the excited-state potential-energy surface probed by resonance Raman is limited to the Franck-Condon region.

1.1.3 Dynamic-Absorption Spectroscopy

Shank, Mathies and co-workers[5-7,16,21-25] showed more than ten years ago that resonant impulsive excitation of large electronic chromophores in condensed phases and in proteins results in a nonstationary absorption/stimulated-emission spectrum. When monitored with a short, delayed probe pulse that is resonant with the ground-state absorption spectrum, the intensity of the transmitted probe light is modulated at the normal-mode frequencies that would appear in the resonance Raman spectrum. If the probe pulse is resonant with the stimulated-emission spectrum, the modulation frequencies are those of the excited electronic state. This so-called dynamic-absorption spectroscopy was described by Pollard and Mathies[26-29] in terms of coherent motion of vibronic wave packets (vibrational coherence) on the resonant electronic excited-state and ground-state potential-energy surfaces, the latter produced by stimulated-Raman transitions.

Both high time resolution and wavelength resolution can be obtained from dynamic-absorption spectroscopy.[28,29] In dynamic-absorption spectroscopy, the transmitted probe beam is spectrally dispersed before striking the detector. The transient absorption of the sample is obtained by measuring how the spectrum of the probe pulse is changed by transmission through the sample.[28] The pump–probe signal is displayed as the ratio of the intensity of the probe pulse in the presence and the absence of the pump pulse. Fragnito and coworkers observed vibrational wave packet motion on the ground and excited-state

surfaces of nile blue (an organic dye) in solution, while retaining 6-fs time resolution using dynamic-absorption.[16]

In dynamic-absorption spectroscopy, high time and frequency resolution is possible because the actual measurement of the spectrum for a given probe delay is not time resolved. The interaction of the probe pulse with the sample creates a transient oscillating dipole moment whose subsequent emission is in the same direction as the probe pulse.[28] As the probe-pulse spectrum is not time resolved, any emission from the sample is measured together with the probe pulse at the same time. A net absorption of energy from the probe pulse will result if there is destructive interference between the probe pulse and the emission from the sample.

1.1.4 Frequency Domain vs. Time Domain

The main limitation of resonance Raman spectroscopy is that low-frequency modes are difficult to detect due to Rayleigh scattering at the excitation wavelength. Whereas dynamic-absorption spectroscopy is not affected by Rayleigh scattering, low-frequency vibrational modes can easily be detected, as long as the time record of the data is of sufficient length. Higher frequency modes are obtained easier through resonance Raman spectroscopy. The frequency information returned is from dynamic-absorption spectroscopy is affected by the pulse duration. In order to observe wave-packet motion at a given frequency, the excitation pulse has to be much shorter than the vibrational period. This means that the duration of the pulses used can be adjusted to prevent the observation of higher frequency modes, if one is only interested in the low-frequency vibrational modes of a system.

An additional limitation of resonance Raman spectroscopy is the limited probe region. Resonance Raman is only able to probe the Franck-Condon region of the excited-state potential-energy surface. In dynamic-absorption spectroscopy, one can probe outside the Franck-Condon region. There is even the possibility to investigate product states.

1.1.4.1 Limitations of Current Techniques

Unfortunately, for large molecules with small Stokes shifts, a clear distinction between the ground-state and excited-state vibrational coherence cannot be made solely on the basis of probe wavelength because the ground-state depletion and stimulated-emission signals overlap near the 0–0 vibronic transition. A more powerful approach employs the distinct phase of the vibrations on the two surfaces. Owing to the back-and-forth motion by a wave packet on a particular surface, the pump–probe signal exhibits a sweep of the modulation time maxima with respect to the probe wavelength between two limits that correspond to a phase shift.[7,9,30-34] So, one might expect to be able to define the spectral regions corresponding to the motions of the excited-state and ground-state wave packets on the basis of their expected shifts of phase. In practice, a mode-specific analysis of the phase in pump–probe transients is very difficult where spectral overlaps occur.[35]

1.1.5 Review of Wave Packet Vibrational Work

The development of femtosecond laser systems capable of emitting very short, vibrationally impulsive pulses has led to many advances in the understanding of condensed phase chemical dynamics. Coherent wave-packet motion (vibrational coherences) has been reported by several investigators in both condensed-phase[5-

[7,9,10,16,17,23-26,28,31-33,36-56] and gas-phase systems.[57-85] Vibrational wave packets have been reported in pump–probe experiments, for example in the work by Vos *et. al.*[9,86,87] on the reaction center, by the Scherer group[37] in their work on Prussian Blue, and the work by Kumble *et al.*[88] on B820. Stanley and Boxer[89] observed wave-packet motion in the fluorescence emitted from the photosynthetic reaction center.

1.1.5.1 Myoglobin

Champion and coworkers observed vibrational coherences following the photodissociation of NO bound to myoglobin (MbNO) forming deoxymyoglobin (Mb).[17,31,43] Oscillations arising from the coherent nuclear motion of the heme group were observed in both the MbNO absorption band and the Mb absorption band. Observation of the 220 cm^{-1} mode (Fe-N_{His} bond) in the MbNO absorption band was of interest because MbNO does not have a resonance Raman-active mode associated with the Fe-N_{His} motion.[17] This work showed that dynamic absorption spectroscopy could be used to excite and probe vibrational modes that lacked Franck-Condon activity. The photodissociation of the NO group from the heme resulted in the coupling of the non-Franck-Condon-active vibrational modes to vibrational modes that were electronically excited.

1.1.5.2 Photosynthetic Reaction Center

Low- frequency resonance Raman work done by Boxer, Mathies and coworkers[90,91] suggests that electronic and dynamical properties of the special pair, P, are more complicated than generally thought. Vos et al. observed coherent vibrational wave packet

motion in the pump-probe transients for reaction center preparations.[9,92-95] This work detected low-frequency modes at 15–30 cm^{-1} and 70–150 cm^{-1} . Vos and Martin suggest that these low-frequency modes are from protein-derived modes. Similar low-frequency modes were observed by Stanley and Boxer in modulations of the spontaneous fluorescence from P*.[89]

1.1.5.3 Rhodopsin

Mathies and coworkers used 10-fs pulses to investigate the *cis-trans* isomerization of the retinal chromophore in the visual pigment protein rhodopsin.[5-7] Oscillations with a period of 550 fs (60 cm^{-1}) were attributed to nonstationary vibrational motion in the ground state of the photoproduct; i.e. vibrational coherence persisted throughout the time course of the photochemical reaction. The 60 cm^{-1} mode oscillation was attributed to a torsional mode of the retinal chromophore.It was proposed that the isomerization reaction is so efficient because the 200-fs reaction time is comparable to or less than the period of torsional vibrations of retinal that are associated with the isomerization reaction.[5-7]

1.2 Carbocyanine Dyes as Model Systems

IR144 (anhydro-11-(4-ethoxycarbonyl-1-piperazinyl)-10,12-ethylene-3,3,3',3'-tetramethyl-1,1'-di-(3-sulfopropyl)-4,5,4',5'-dibenzoindotricarbocyanine hydroxide) and DTTCI (3,3'-diethylthiatricarbocyanine iodide) are carbocyanine dyes which make useful models, as the structures are similar to that of the retinal chromophore in rhodopsin. In addition, these carbocyanine dyes have small Stokes shifts, making separation of the ground- and excited-state signals difficult.

These carbocyanine dyes have been extensively used as probes in solvation dynamics studies.[40,44,96-99] In much of this work, it is assumed that the structure is invariant during the early solvent reorganization dynamics. IR144 has a central five-membered ring, which might be expected to inhibit *trans-cis* isomerization of the conjugated polyene. DTTCI is a reactive system in which the *trans-cis* isomerization of the conjugated polyene can occur after excitation.[100,101]

1.2.1 Review of Vibrational Coherence Observed from Carbocyanine Dyes

Fleming and coworkers studied IR144 and DTTCI in solution[97,102] and in polymer glasses[40,98] using transient grating (TG), 3-pulse photon echo peak shift (3PEPS), and transient absorption (TA) spectroscopies. In the solution studies, vibrational frequencies were given for IR144 in ethanol.[97] Frequencies for both DTTCI and IR144 were given from the polymer glasses studies.[40] The goal of the experiments was to study solvation dynamics, so no attempt was made to assign the observed frequencies to vibrational modes of the dye.

Wiersma and coworkers performed TG and 3PEPS experiments on DTTCI in various solvents to elucidate the role of the solvent in vibrational dephasing. Vibrational frequencies in the 100–500-cm^{-1} range were observed from DTTCI in acetonitrile, ethylene glycol and methanol.[44] The observed vibrational modes were assigned to ground-state vibrations of the chromophore. The experiments showed no evidence of solvent effects.[44]

Vöhringer and coworkers used pump–probe experiments to study the solvent and frequency dependence of vibrational dephasing on a similar dye, HITCI (1,1',3,3,3',3'-

hexamethylindotricarbocyanine iodide) in various solvents.[53] Vibrational frequencies up to 800 cm^{-1} were observed, but no evidence of solvent dependence. Vöhringer and coworkers assigned the low frequency components (<200 cm^{-1}) to vibrations from the first excited state, while the higher frequency modes were assigned to ground-state vibrations.

1.3 References

(1) Boxer, S. G.; Goldstein, R. A.; Lockhart, D. J.; Middendorf, T. R.; Takiff, L. *J. Phys. Chem.* **1989**, *93*, 8280–8294.

(2) Parson, W. W. In *Photosynthesis*; Amesz, J., Ed.; Elsevier, 1987, p 43–61.

(3) Friesner, R. A.; Won, Y. *Biochim. Biophys. Acta* **1989**, *977*, 99–122.

(4) Deisenhofer, J.; Epp, O.; Miki, K.; Huber, R.; Michel, H. *Nature* **1985**, *318*, 618–624.

(5) Peteanu, L. A.; Schoenlein, R. W.; Wang, Q.; Mathies, R. A.; Shank, C. V. *Proc. Natl. Acad. Sci. USA* **1993**, *90*, 11762–11766.

(6) Schoenlein, R. W.; Peteanu, L. A.; Mathies, R. A.; Shank, C. V. *Science* **1991**, *254*, 412–415.

(7) Wang, Q.; Schoenlein, R. W.; Peteanu, L. A.; Mathies, R. A.; Shank, C. V. *Science* **1994**, *266*, 422–424.

(8) Brandon, C.; Tooze, J. *Introduction to Protein Structure*; 2nd ed.; Garland Publishing, Inc.: New York, 1999.

(9) Vos, M. H.; Rappaport, F.; Lambry, J.-C.; Breton, J.; Martin, J.-L. *Nature* **1993**, *363*, 320–325.

(10) Jonas, D. M.; Bradforth, S. E.; Passino, S. A.; Fleming, G. R. *J. Phys. Chem.* **1995**, *99*, 2594–2608.

(11) Zewail, A. H. *J. Phys. Chem.* **1993**, *97*, 12427-12446.

(12) Heller, E. J. *Acc. Chem. Res.* **1981**, *14*, 368-375.

(13) Heller, E. J.; Sundberg, R. L.; Tannor, D. *J. Phys. Chem.* **1982**, *86*, 1822–1833.

(14) Lee, S.-Y.; Heller, E. J. *J. Chem. Phys.* **1979**, *71*, 4777–4788.

(15) Johnson, A. E.; Myers, A. B. *J. Chem. Phys.* **1996**, *104*, 2497–2507.

(16) Fragnito, H. L.; Bigot, J.-Y.; Becker, P. C.; Shank, C. V. *Chem. Phys. Lett.* **1989**, *160*, 101–104.

(17) Zhu, L.; Wang, W.; Sage, J. T.; Champion, P. M. *J. Raman Spect.* **1995**, *26*, 527–534.

(18) Myers, A. B.; Mathies, R. A. In *Biological Applications of Raman Spectroscopy*; Spiro, T. G., Ed.; Wiley-Interscience: New York, 1987; Vol. 2, *Resonance Raman Spectra of Polyenes and Aromatics*, p 1–58.

(19) Spiro, T. G.; Stein, P. *Annu. Rev. Phys. Chem.* **1977**, *28*, 501–521.

(20) Myers, A. B. *Chem. Rev.* **1996**, *96*, 911–926.

(21) Brito Cruz, C. H.; Fork, R. L.; Knox, W. H.; Shank, C. V. *Chem. Phys. Lett.* **1986**, *132*, 341–345.

(22) Brito Cruz, C. H.; Gordon, J. P.; Becker, P. C.; Fork, R. L.; Shank, C. V. *IEEE J. Quant. Elect.* **1988**, *24*, 261–266.

(23) Mathies, R. A.; Brito Cruz, C. H.; Pollard, W. T.; Shank, C. V. *Science* **1988**, *240*, 777–779.

(24) Pollard, W. T.; Cruz, C. H. B.; Shank, C. V.; Mathies, R. A. *J. Chem. Phys.* **1989**, *90*, 199–208.

(25) Dexheimer, S. L.; Wang, Q.; Peteanu, L. A.; Pollard, W. T.; Mathies, R. A.; Shank, C. V. *Chem. Phys. Lett.* **1992**, *188*, 61–66.

(26) Pollard, W. T.; Fragnito, H. L.; Bigot, J.-Y.; Shank, C. V.; Mathies, R. A. *Chem. Phys. Letters* **1990**, *168*, 239–245.

(27) Pollard, W. T.; Lee, S.-Y.; Mathies, R. A. *J. Chem. Phys.* **1990**, *92*, 4012–4029.

(28) Pollard, W. T.; Mathies, R. A. *Annu. Rev. Phys. Chem.* **1992**, *43*, 497–523.

(29) Pollard, W. T.; Dexheimer, S. L.; Wang, Q.; Peteanu, L. A.; Shank, C. V.; Mathies, R. A. *J. Phys. Chem.* **1992**, *96*, 6147–6158.

(30) Bowman, R. M.; Dantus, M.; Zewail, A. H. *Chem. Phys. Lett.* **1990**, *174*, 546–552.

(31) Zhu, L.; Sage, J. T.; Champion, P. M. *Science* **1994**, *266*, 629–632.

(32) Chachisvilis, M.; Fidder, H.; Pullerits, T.; Sundström, V. *J. Raman Spect.* **1995**, *26*, 513–522.

(33) Bardeen, C. J.; Wang, Q.; Shank, C. V. *J. Phys. Chem. A* **1998**, *102*, 2759–2766.

(34) Rosca, F.; Kumar, A. T. N.; Ye, X.; Sjodin, T.; Demidov, A.; Champion, P. M. *J. Phys. Chem. A* **2000**, *104*, 4280–4290.

(35) Diffey, W. M. In *Department of Chemistry*; Vanderbilt University: Nashville, Tennessee, 2002.

(36) Savikhin, S.; Buck, D. R.; Struve, W. S. *Chem. Phys.* **1997**, *223*, 303–312.

(37) Arnett, D. C.; Vöhringer, P.; Scherer, N. F. *J. Am. Chem. Soc.* **1995**, *117*, 12262–12272.

(38) Ashworth, S. H.; Joschko, M.; Woerner, M.; Riedle, E.; Elsaesser, T. *Optics Letters* **1996**, *20*, 2120–2122.

(39) Lenderink, E.; Duppen, K.; Wiersma, D. A. *J. Phys. Chem.* **1995**, *99*, 8972–8977.

(40) Nagasawa, Y.; Passino, S. A.; Joo, T.; Fleming, G. R. *J. Chem. Phys.* **1997**, *106*, 4840–4852.

(41) Streltsov, A. M.; Vulto, S. I. E.; Shkuropatov, A. Y.; Hoff, A. J.; Aartsma, T. J.; Shuvalov, V. A. *J. Phys. Chem. B* **1998**, *102*, 7293–7298.

(42) Tian, W. D.; Sage, J. T.; Champion, P. M.; Chien, E.; Sligar, S. G. *Biochemistry* **1996**, *35*, 3487–3502.

(43) Zhu, L.; Li, P.; Huang, M.; Sage, J. T.; Champion, P. M. *Phys. Rev. Lett.* **1994**, *72*, 301–304.

(44) de Boeij, W. P.; Pshenichnikov, M. S.; Wiersma, D. A. *J. Phys. Chem.* **1996**, *100*, 11806–11823.

(45) Arnett, D. C.; Yang, T.-S.; Moser, C.; Scherer, N. F. In *Femtochemistry: Ultrafast chemical and physical processes in molecular systems*; Chergui, M., Ed.; World Scientific: Singapore, 1996, p 407–413.

(46) Arnett, D. C.; Moser, C. C.; Dutton, P. L.; Scherer, N. F. *Laser Chemistry* **1999**, *19*, 161–164.

(47) Book, L. D.; Arnett, D. C.; Hu, H.; Scherer, N. F. *J. Phys. Chem. A* **1998**, *102*, 4350–4359.

(48) Arnett, D. C.; Moser, C. C.; Dutton, P. L.; Scherer, N. F. *J. Phys. Chem. B* **1999**, *103*, 2014–2032.

(49) Hayashi, M.; Yang, T.-S.; Mebel, A.; Chang, C. H.; Lin, S. H.; Scherer, N. F. *Chem. Phys.* **1997**, *217*, 259–273.

(50) Scherer, N. F.; Ziegler, L. D.; Fleming, G. R. *J. Chem. Phys.* **1992**, *96*, 5544–5547.

(51) Scherer, N. F.; Jonas, D. M.; Fleming, G. R. *J. Chem. Phys.* **1993**, *99*, 153–168.

(52) Scherer, N. F.; Book, L. D.; Ungar, L. W.; Arnett, D. C.; Hu, H.; Voth, G. A. In *Ultrafast Phenomena X*; Barbara, P. F., Fujimoto, J. G., Knox, W. H., Zinth, W., Eds.; Springer-Verlag: Berlin, 1996, p 361–362.

(53) Vohringer, P.; Westervelt, R. A.; Yang, T.-S.; Arnett, D. C.; Feldstein, M. J.; Scherer, N. F. *J. Raman Spect.* **1995**, *26*, 535–551.

(54) Pollard, W. T.; Brito Cruz, C. H.; Shank, C. V.; Mathies, R. A. *J. Chem. Phys.* **1988**, *90*, 199–208.

(55) Schoenlein, R. W.; Peteanu, L. A.; Wang, Q.; Mathies, R. A.; Shank, C. V. *J. Phys. Chem.* **1993**, *97*, 12087–12092.

(56) Wang, Q.; Kochendoerfer, G. G.; Schoenlein, R. W.; Verdegem, P. J. E.; Lugtenburg, J.; Mathies, R. A.; Shank, C. V. *J. Phys. Chem.* **1996**, *100*, 17388–17394.

(57) Bardeen, C. J.; Che, J.; Wilson, K. R.; Yakovlev, V. V.; Cong, P.; Kohler, B.; Krause, J. L.; Messina, M. *J. Phys. Chem. A* **1997**, *101*, 3815–3822.

(58) Bernstein, R. B.; Zewail, A. H. *J. Chem. Phys.* **1989**, *90*, 829–842.

(59) Bernstein, R. B.; Zewail, A. H. *Chem. Phys. Lett.* **1990**, *170*, 321–328.

(60) Bowman, R. M.; Dantus, M.; Zewail, A. H. *Chem. Phys. Lett.* **1989**, *161*, 297–302.

(61) Dantus, M.; Bowman, R. M.; Baskin, J. S.; Zewail, A. H. *Chem. Phys. Lett.* **1989**, *159*, 406–412.

(62) Dantus, M.; Bowman, R. M.; Zewail, A. H. *Nature* **1990**, *343*, 737–739.

(63) Dantus, M.; Janssen, M. H. M.; Zewail, A. H. *Chem. Phys. Lett.* **1991**, *181*, 281–287.

(64) Dantus, M.; Rosker, M. J.; Zewail, A. H. *J. Chem. Phys.* **1987**, *87*, 2395–2397.

(65) Dantus, M.; Rosker, M. J.; Zewail, A. H. *J. Chem. Phys.* **1987**, *89*, 6128–6140.

(66) Gruebele, M.; Zewail, A. H. *Phys. Today* **1990**, *43*, 24–33.

(67) Gruebele, M.; Roberts, M.; Dantus, M.; Bowman, R. M.; Zewail, A. H. *Chem. Phys. Lett.* **1990**, *166*, 459–469.

(68) Gruebele, M.; Sims, I. R.; Potter, E. D.; Zewail, A. H. *J. Chem. Phys.* **1991**, *95*, 7763–7766.

(69) Khundkar, L. R.; Zewail, A. H. *Annu. Rev. Phys. Chem.* **1990**, *41*, 15–60.

(70) Liu, Q.; Wang, J.-K.; Zewail, A. H. *Nature* **1993**, *364*, 427–430.

(71) Nelson, K. A. In *Ultrafast Phenomena IX*; Barbara, P. F., Knox, W. H., Mourou, G. A., Zewail, A. H., Eds.; Springer-Verlag: Berlin, 1994, p 47.

(72) Pedersen, S.; Herek, J. L.; Zewail, A. H. *Science* **1994**, *266*, 1359–1364.

(73) Polanyi, J. C.; Zewail, A. C. *Acc. Chem. Res.* **1995**, *28*, 119–132.

(74) Porter, G. In *The Chemical Bond: Structure and Dynamics*; Zewail, A., Ed.; Academic Press, Inc.: Boston, 1992, p 113–148.

(75) Reid, P. J.; Silva, C.; Dong, Y.; Hupp, J. T.; Barbara, P. F. In *Ultrafast Phenomena IX*; Barbara, P. F., Knox, W. H., Mourou, G. A., Zewail, A. H., Eds.; Springer-Verlag: Berlin, 1994, p 505–506.

(76) Rosker, M. J.; Dantus, M.; Zewail, A. H. *Science* **1988**, *241*, 1200–1202.

(77) Rosker, M. J.; Dantus, M.; Zewail, A. H. *J. Chem. Phys.* **1988**, *89*, 6113–6127.

(78) Rosker, M. J.; Wise, F. W.; Tang, C. L. *Phys. Rev. Lett.* **1986**, *57*, 321-324.

(79) Wise, F. W.; Rosker, M. J.; Tang, C. L. *J. Chem. Phys.* **1987**, *86*, 2827-2832.

(80) Scherer, N. F.; Knee, J. L.; Smith, D. D.; Zewail, A. H. *J. Phys. Chem.* **1985**, *89*, 5140–5143.

(81) Zewail, A. H. *Nature* **1988**, *328*, 760–761.

(82) Zewail, A. H. *Scientific American* **1990**, *263*, 76–82.

(83) Zewail, A. H. *Faraday Discuss. Chem. Soc.* **1991**, *91*, 207–237.

(84) Zewail, A.; Bernstein, R. In *The Chemical Bond: Structure and Dynamics*; Zewail, A., Ed.; Academic Press: San Diego, 1992, p 223–279.

(85) Zewail, A. H. In *Femtosecond Chemistry*; Manz, J., W\"oste, L., Eds.; VCH Publishers: New York, 1995, p 15–128.

(86) Vos, M. H.; Lambry, J. C.; Robles, S. J.; Youvan, D. C.; Breton, J.; Martin, J. L. *Proceedings of the National Academy of Sciences of the United States of America* **1991**, *88*, 8885-8889.

(87) Vos, M. H.; Lambry, J. C.; Robles, S. J.; Youvan, D. C.; Breton, J.; Martin, J. L. *Proceedings of the National Academy of Sciences of the United States of America* **1992**, *89*, 613-617.

(88) Kumble, R.; Palese, S.; Visschers, R. W.; Dutton, P. L.; Hochstrasser, R. M. *Chem. Phys. Lett.* **1996**, *261*, 396–404.

(89) Stanley, R. J.; Boxer, S. G. *J. Phys. Chem.* **1995**, *99*, 859–863.

(90) Cherepy, N. J.; Shreve, A. P.; Moore, L. J.; Boxer, S. G.; Mathies, R. A. *J. Phys. Chem. B* **1997**, *101*, 3250–3260.

(91) Cherepy, N. J.; Shreve, A. P.; Moore, L. J.; Franzen, S.; Boxer, S. G.; Mathies, R. A. *J. Phys. Chem.* **1994**, *98*, 6023–6029.

(92) Vos, M. H.; Jones, M. R.; Breton, J.; Lambry, J.-C.; Martin, J.-L. *Biochemistry* **1996**, *35*, 2687–2692.

(93) Vos, M. H.; Jones, M. R.; Hunter, C. N.; Breton, J.; Lambry, J.-C.; Martin, J.-L. *Biochemistry* **1994**, *33*, 6750–6757.

(94) Vos, M. H.; Jones, M. R.; Hunter, C. N.; Breton, J.; Martin, J.-L. *Proc. Natl. Acad. Sci. USA* **1994**, *91*, 12701–12705.

(95) Vos, M. H.; Jones, M. R.; McGlynn, P.; Hunter, C. N.; Breton, J.; Martin, J.-L. *Biochim. Biophys. Acta* **1994**, *1186*, 117–122.

(96) Pshenichnikov, M. S.; Duppen, K.; Wiersma, D. A. *Phys. Rev. Lett.* **1995**, *74*, 674–677.

(97) Joo, T.; Jia, Y.; Yu, J.-Y.; Lang, M. J.; Fleming, G. R. *J. Chem. Phys.* **1996**, *104*, 6089–6108.

(98) Passino, S. A.; Nagasawa, Y.; Joo, T.; Fleming, G. R. *J. Phys. Chem. A* **1997**, *101*, 725–731.

(99) Shang, X.; Benderskii, A. V.; Eisenthal, K. B. *J. Phys. Chem. B* **2001**, *105*, 11578–11585.

(100) Sahyun, M. R. V.; Serpone, N. *J. Phys. Chem. A* **1997**, *101*, 9877–9883.

(101) Sanchez-Galvez, A.; Hunt, P.; Robb, M. A.; Olivucci, M.; Vreven, T.; Schlegel, H. B. *J. Am. Chem. Soc.* **2000**, *122*, 2911–2924.

(102) Cho, M.; Yu, J.-Y.; Joo, T.; Nagasawa, Y.; Passino, S. A.; Fleming, G. R. *J. Phys. Chem.* **1996**, *100*, 11944–11953.

CHAPTER 2

EXPERIMENTAL APPARATUS

2.0 Introduction

Broad gain bandwidth, large energy storage density and favorable thermal properties are attained from titanium–sapphire ($Ti:Al_2O_3$). Self-mode-locking (Kerr Lens mode-locking) lasers made titanium-sapphire laser systems ideal for ultrafast spectroscopy, as sub 20-fs pulse durations can be obtained.[1-3] As discussed in chapter one, many groups have employed ultrafast oscillators to study a variety of systems including rhodopsin[4-7], myoglobin[8-12] and the photosynthetic reaction center.[13-18] The following sections will discuss the construction of the titanium-sapphire oscillator and the design of the interferometer.

2.1 Titanium–Sapphire Oscillator

The titanium–sapphire oscillator shown in figure 2.1 is based on the Murnane-Kapteyn design[2,3] using components from a Clark Instrument NJA-4 kit. This oscillator had been built previously by other group members,[19,20] but was reconstructed here at Michigan State University.

The main components of the oscillator are the gain medium, high reflector (HR) mirror, and an output coupler (OC). The oscillator is pumped by a Verdi (Coherent) 5-W laser. The gain medium is a 4 mm, brewster cut, 0.15% doped titanium–sapphire crystal purchased from Union Carbide. Dichroic curved mirrors with 10 cm radii that are transparent for the 532-nm pump light, but reflect the 800-nm laser light are arranged on

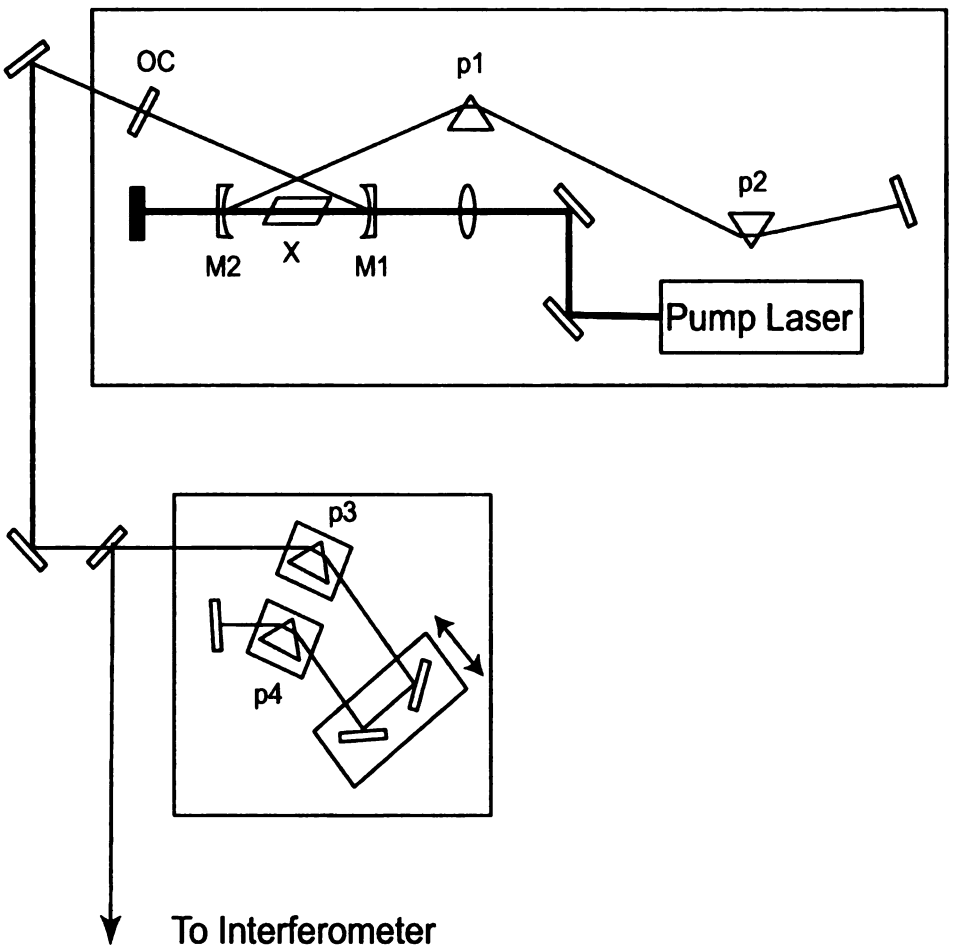

Figure 2.1. Self-mode-locked titanium–sapphire laser oscillator and pulse compressor employed in the dynamic-absorption spectroscopy experiments. *Symbols*: p1-p2, fused-silica prisms; M1-M2, dichroic curved mirrors; x, 4-mm titanium: sapphire crystal; OC, output coupler (10% transmitting); HR, high reflecting mirror; p3-p4, LaKL21 prisms.

either side of the gain medium. A HR and 10% OC complete the continuous-wave (cw) cavity. Two fused-silica prisms, brewster cut for 800 nm, complete the oscillator.

2.1.1 Alignment of Oscillator

A lens (f = 12.5 cm) focuses the pump laser into the gain medium. The gain medium is set slightly off-center from two curved mirrors, angled 16° from the crystal. The second curved mirror (M2) is placed on a translation stage (Newport) to allow for alignment adjustments. The HR and OC are arranged close to the gain medium and aligned to overlap the fluorescence spots from titanium–sapphire crystal. A photodiode (Newport) behind the OC monitors cw power. The OC, HR, crystal, M2 and pump focus are adjusted to improve overlap and increase power. Lasing occurs when a strong overlap is obtained. The OC and HR are moved further from the crystal to obtain the desired 2.27-m cavity length. Optimized cw power obtained is 900 mW with 4.5 mW pump power.

A pair of prisms are added to the HR arm of the laser cavity. Both of the prisms are placed on translation stages (Newport) to allow for alignment adjustments. The prisms are separated at distance of 0.62 m and HR is placed to give the 2.27-m cavity length. Oscillator power is maximized by passing the beam through the prism apex. Average power obtained is 450 mW with pump power of 4.5 mW.

The oscillator is monitored by a fast photodiode (ThorLabs) and an optical multichannel array (OMA)/spectrograph (Princeton Instruments). The OMA is a photodiode array that allows real-time observation of the output of the oscillator. As M2 is translated towards the crystal, the shape of the beam is monitored by dispersing the beam with a short-focus lens to obtain an oval beam shape. When the oval shape is obtained, P1

is moved monitoring the OMA spectrum for spectral broadening. Once mode locked, the output spectral bandwidth is controlled by adjusting the amount of prism glass the beam passes through. The oscillator operates at a natural pulse-repetition rate of 76 MHz.

Figure 2.2 shows the output spectrum obtained from the mode-locked oscillator. This spectral bandwidth results in 12-fs ($sech^2$) pulses shown in figure 2.3. The pulse train is sent through a pair of LaKL21 prisms prior to the interferometer. This arrangement allows for precompensation of group-delay dispersion from optics in the interferometer.

2.2 Rapid-Scanning Modified Mach–Zehnder Interferometer

Experiments employing multiple pulses require one arm of the interferometer to be scanned slowly. This motion can be obtained with delay-stage steps, which usually require seconds to obtain a single data point. A single scan can take minutes to obtain, resulting in larger errors due to laser instability. The use of rapid scanning techniques increases signal-to-noise ratios without broadening the instrument response function.[21-23] In order to use this technique, a fused-silica photo-elastic modulator is employed as a 100-kHz amplitude modulator. The design of the interferometer has been described by previous group members[19,24], but modifications have been made to increase signal quality. Figure 2.4 shows the design of the rapid-scanning modified Mach-Zehnder interferometer.

2.2.1 Layout of Interferometer

The horizontal polarization of the incident pulse train is rotated to vertical using a periscope arrangement with mirrors of s and p polarization orientated for 45° reflections. The beam is split by a 50% beamsplitter (CVI FABS-800.0-45S-PW-1012-W). The probe

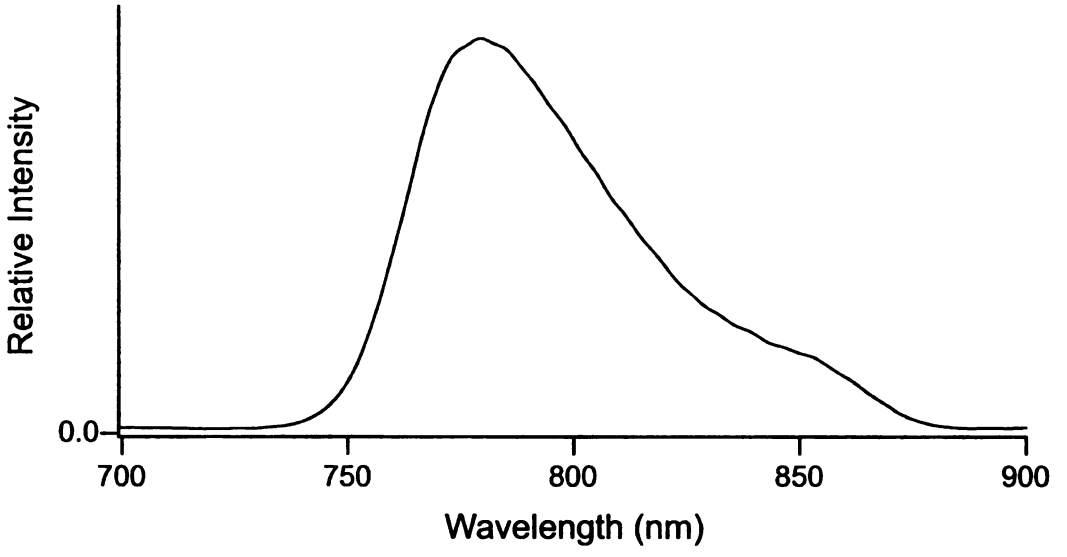

Figure 2.2. Output intensity spectrum of 12-fs ($sech^2$; 53-nm (fwhm) spectral width) pulses from the Murnane-Kapteyn oscillator.

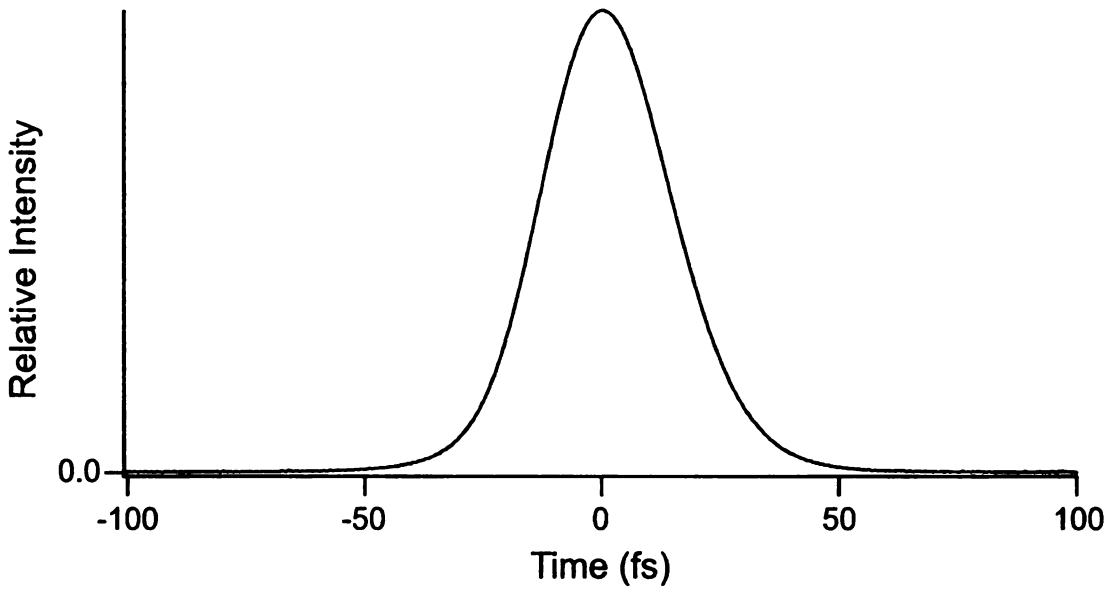

Figure 2.3. Zero-background autocorrelation trace of a 12-fs ($sech^2$) pulse obtained from the Murnane-Kapteyn oscillator.

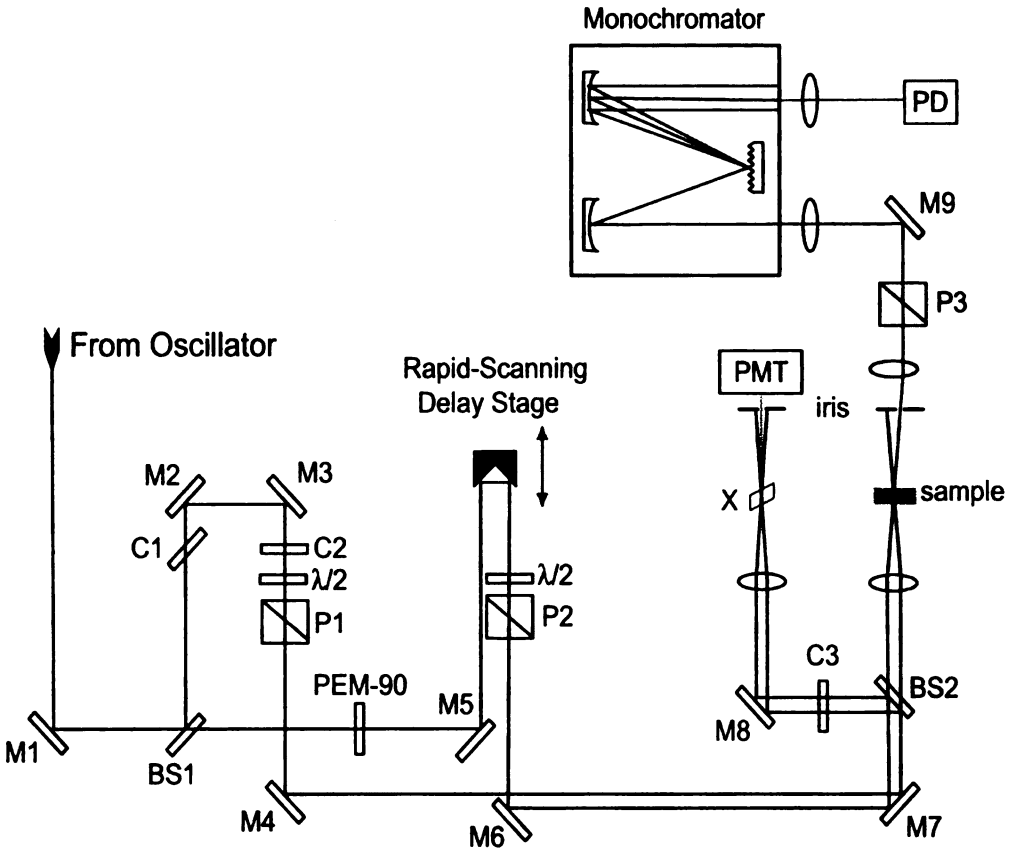

Figure 2.4. Modified Mach-Zehnder rapid-scanning interferometer employed in the dynamic-absorption spectroscopy experiments. *Symbols*: M1-M9, silver mirrors; BS1-BS2, beam splitters; C1-C3, compensation optics; $\lambda/2$, half-wave plates; P1-P3, Glan-laser calcite polarizers; PEM-90, photoelastic modulator; x, β-barium borate crystal; PMT, photomultiplier tube; PD, photodiode.

arm employs a manually adjusted translation stage (Newport) and two silver mirrors (New Focus 5103) to adjust the path length to that of the pump arm of the interferometer.

The pump arm employs a Clark Instrumentation ODL-150 rapid-scanning delay. The ODL-150 uses a galvanometer-type drive system (General Scanning G325DT galvanometer) and miniature translation stage to scan a retroreflector linearly. Prior to the rapid-scanning retroreflector, the pulse train encounters a 50-kHz fused-silica photoelastic modulator (Hinds Instruments, PEM90). The modulator is set up as a $\lambda/2$ retarder for the center wavelength of the titanium–sapphire laser spectrum, typically 780 nm. Alignment of the fused-silica plate is normal to the pulse train and 45° with respect to the optical table. The modulator is followed by a Glan-laser calcite polarizer (Karl Lambrecht) allowing only vertical polarization to pass. A mica zero-order $\lambda/2$ plate (Karl Lambrecht) is used to adjust the pulse train for 100% depth modulation.

The probe arm has a fused-silica plate as a compensator and a Glan-laser calcite polarizer, identical to that in the pump arm. Polarization of the probe beam is set 45° relative to polarization of the pump beam. A mica zero-order $\lambda/2$ plate (Karl Lambrecht) is used to adjust power for a 4:1 pump-probe ratio. Both the pump and probe beams have identical optics, so one pair of prisms can be used to compensate both beams for group-delay dispersion.

A 10-cm focal length BK7 lens is used to focus the pump and probe beams onto the sample position. In order to ensure spatial overlap of the pump and probe beams, both beams are aligned through a 25-μm pinhole. Initially, a 100-μm thick β-barium borate crystal (Inrad), cut for type I sum-frequency generation with 800-nm input, is placed in the sample position to obtain autocorrelation signals. The crystal is replaced with 1-mm flow

cell which holds recirculating sample solution. After transmitting the sample and recolumnation, the probe beam is analyzed by another Glan-laser calcite polarizer. The angle used for analysis is 63.44° for all experiments except for the polarization studies where analysis polarization is set parallel and perpendicular to polarization of the pump beam. The probe beam is passed through a Spex 270m monochromator with a spectral bandpass of 4 nm and detected by an amplified silicon photodiode (Thorlabs, PDA520). The photodiode signal is demodulated by a digital lock-in amplifier (Stanford Research Systems, SRS830) which is referenced to the 100-kHz pump-amplitude-modulation frequency.

Both the pump and probe beams are sampled prior to the focusing lens to provide pulses for autocorrelation analysis during data acquisition. The beams are focused onto the crystal position with a 10-cm focal-length BK7 lens. Zero-background autocorrelation measurements employ a 100-μm thick β-barium borate crystal (Inrad), cut for type I sum-frequency generation with 800-nm input. The second-harmonic beam is detected by a photomultiplier tube and lock-in amplifier (LIA-MV-200-H, Femto Messtechnik). Identical optics are used in the autocorrelation and sample arms, so group-delay dispersion is the same for both.

2.3 Data Collection

A sample/hold amplifier and digitizer (National Instruments, SC-2040S/H and PCI-6024E) record the analog outputs of the two lock-in amplifiers (for the pump–probe signal and autocorrelation signal), the transmitted-probe photodiode signal, and the position of the galvanometer (delay reference) signal. Figure 2.5 shows the multiple traces

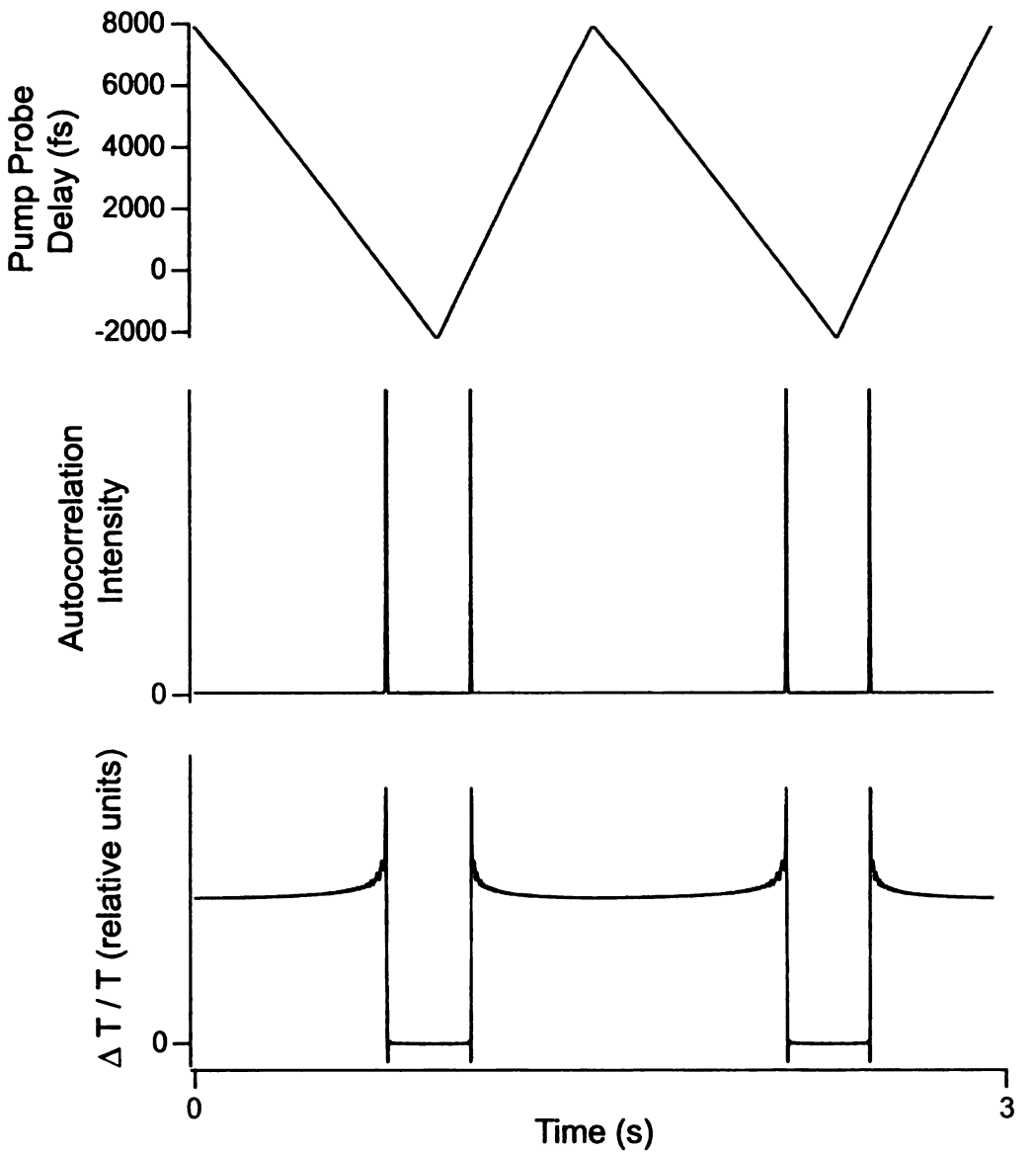

Figure 2.5. Multiple traces obtained simultaneously during dynamic-absorption experiments of DTTCI in methanol obtained at 790 nm. Two complete scans of rapid-scanning delay stage are shown as a fuction of lab time. *Top*: Pump-probe delay determined from the position of the rapid-scanning delay stage. *Middle*: Zero-background autocorrelation. *Bottom*: Single-wavelength dynamic-absorption transient.

that are obtained during dynamic-absorption experiments. Two complete scans of the rapid-scanning delay stage are shown as a function of lab time.

The pump-probe delay is calculated from the position of the rapid-scanning delay stage. The position of the stage is calibrated by adjusting the distance the probe pulse must travel and measuring the movement of the zero-background autocorrelation signal relative to the position of the delay stage. The change in distance travelled by the probe pulse is converted to time and delay-stage position is measured in volts. A conversion factor of fs/V can be calculated and used to convert the position of the delay stage to pump-probe delay.

For each scan of the delay stage, the pump and probe pulses interact twice. As observed in figure 2.5, two scans of the delay stage give four zero-background autocorrelation and dynamic-absorption signals. Only data from one half of a complete scan is required for experiments.

The scan range is adjusted to visualize only one pump-probe interaction, as shown in figure 2.6. The delay axis is scanned at 1.3 Hz over a 10-ps delay range and 6000 data points are acquired with a dwell time of 1.8 fs. The digitization frequency is 17 kHz. LabVIEW (National Instruments) routines control the signal-averaging system and the monochromator. Multiple scans are averaged for a single-wavelength measurement. The autocorrelation signal is used as a zero-delay-time reference to eliminate scan-to-scan delay drift.

Standard display of dyanmic-absorption transients is to show the signal as a function of increasing probe delay. Figure 2.7 shows a scan-averaged single-wavelength dynamic-

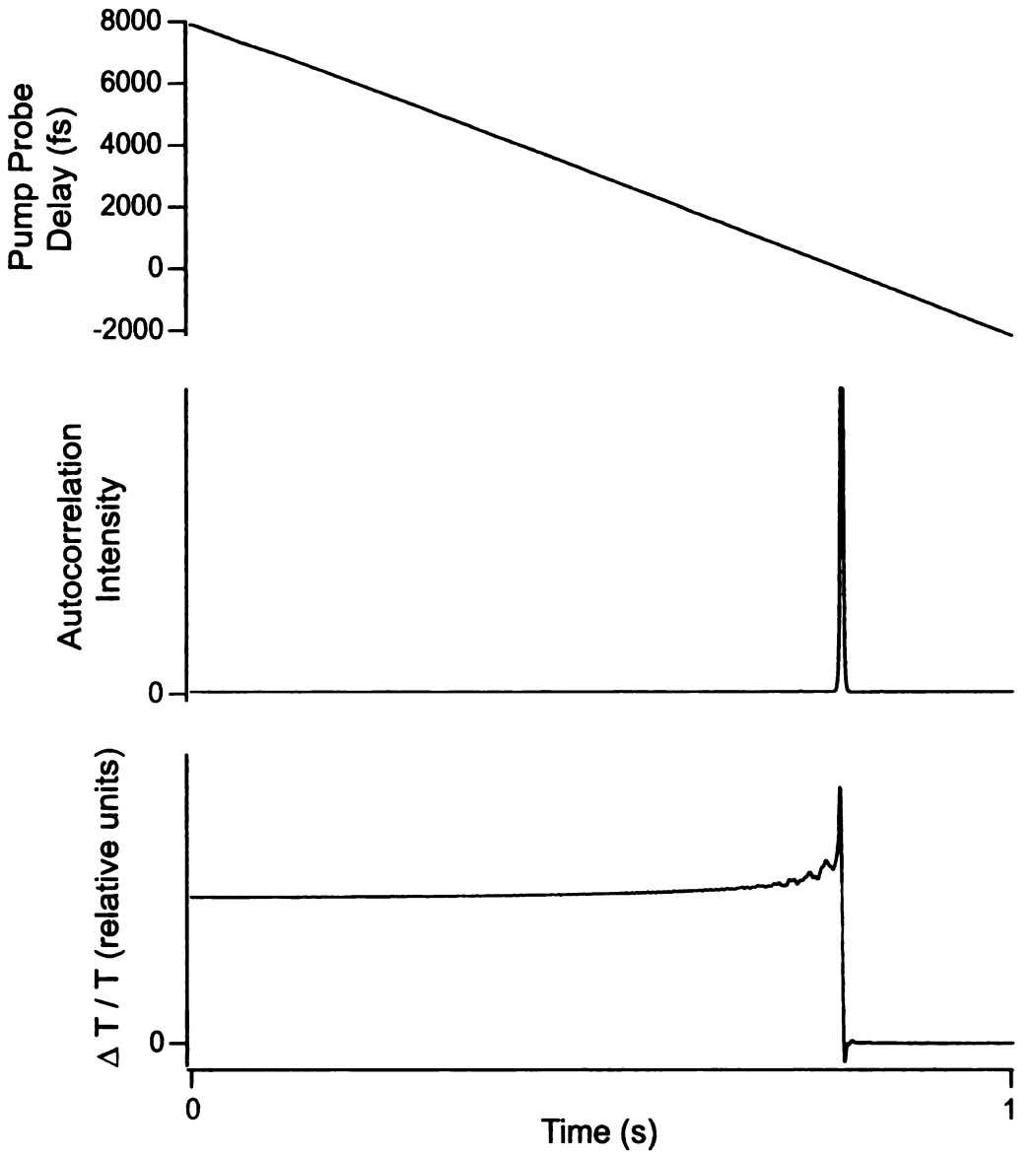

Figure 2.6. Multiple traces obtained simultaneously during dynamic-absorption experiments of DTTCI in methanol obtained at 790 nm. One half of a complete scan of rapid-scanning delay stage is shown as a fuction of lab time. *Top*: Probe delay as determined from the position of the rapid-scanning delay stage. *Middle*: Zero-background autocorrelation. *Bottom*: Single-wavelength dynamic-absorption transient.

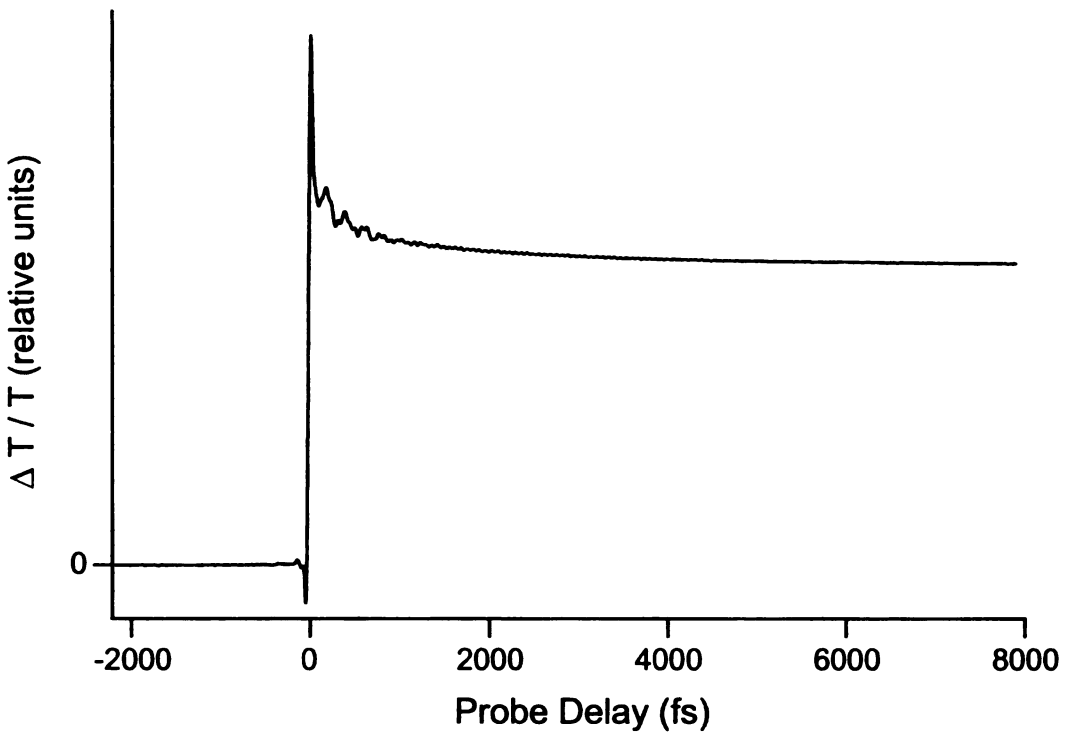

Figure 2.7. Single-wavelength dynamic-absorption transient of DTTCI in methanol obtained at 790 nm displayed as a function of probe delay.

absorption transient as a function of increasing probe delay. Transients will be shown in this form throughout the following chapters.

2.4 Sample Preparation

The carbocyanine dyes, IR144 and DTTCI were obtained from Exciton and used as received. Samples were dissolved methanol (Spectrum, spectrophotmetric grade), DMSO (Spectrum, reactant grade) or acetonitrile (EM Science, HPLC grade) to obtain an absorbance of 0.4–0.6 at λ_{max}. for a 1-mm path length. The samples were passed through a 0.22-μm filter prior to use. Samples for femtosecond spectroscopy were held at room temperature in a fused-silica flow cuvette with 1-mm path length. Samples were circulated through the cuvette at a rate of 6 mL/min using a peristaltic pump. The absorption spectrum of the sample was monitored for changes arising from photchemistry or permanent photobleaching.

This experimental design is used in chapters three through five of this dissertation to examine the vibrational coherence of the carbocyanine dyes IR144 and DTTCI.

2.5 References

(1) Christov, I. P.; Stoev, V. D.; Murnane, M. M.; Kapteyn, H. C. *Optics Letters* **1996**, *21*, 1493-1495.

(2) Huang, C.-P.; Asaki, M. T.; Backus, S.; Murnane, M. M.; Kapteyn, H. C.; Nathel, H. *Optics Letters* **1992**, *17*, 1289–1291.

(3) Asaki, M. T.; Huang, C.-P.; Garvey, D.; Zhou, J.; Kapteyn, H. C.; Murnane, M. M. *Optics Letters* **1993**, *18*, 977–979.

(4) Mathies, R. A.; Brito Cruz, C. H.; Pollard, W. T.; Shank, C. V. *Science* **1988**, *240*, 777–779.

(5) Pollard, W. T.; Fragnito, H. L.; Bigot, J.-Y.; Shank, C. V.; Mathies, R. A. *Chem. Phys. Letters* **1990**, *168*, 239–245.

(6) Schoenlein, R. W.; Peteanu, L. A.; Mathies, R. A.; Shank, C. V. *Science* **1991**, *254*, 412–415.

(7) Wang, Q.; Schoenlein, R. W.; Peteanu, L. A.; Mathies, R. A.; Shank, C. V. *Science* **1994**, *266*, 422–424.

(8) Zhu, L.; Li, P.; Huang, M.; Sage, J. T.; Champion, P. M. *Phys. Rev. Lett.* **1994**, *72*, 301–304.

(9) Zhu, L.; Sage, J. T.; Champion, P. M. *Science* **1994**, *266*, 629–632.

(10) Zhu, L.; Wang, W.; Sage, J. T.; Champion, P. M. *J. Raman Spect.* **1995**, *26*, 527–534.

(11) Tian, W. D.; Sage, J. T.; Champion, P. M.; Chien, E.; Sligar, S. G. *Biochemistry* **1996**, *35*, 3487–3502.

(12) Wang, W.; Demidov, A.; Ye, X.; Christian, J. F.; Sjodin, T.; Champion, P. M. *J. Raman Spect.* **2000**, *31*, 99–105.

(13) Vos, M. H.; Rappaport, F.; Lambry, J.-C.; Breton, J.; Martin, J.-L. *Nature* **1993**, *363*, 320–325.

(14) Vos, M. H.; Jones, M. R.; Hunter, C. N.; Breton, J.; Lambry, J.-C.; Martin, J.-L. *Biochemistry* **1994**, *33*, 6750–6757.

(15) Vos, M. H.; Jones, M. R.; Hunter, C. N.; Breton, J.; Martin, J.-L. *Proc. Natl. Acad. Sci. USA* **1994**, *91*, 12701–12705.

(16) Vos, M. H.; Jones, M. R.; McGlynn, P.; Hunter, C. N.; Breton, J.; Martin, J.-L. *Biochim. Biophys. Acta* **1994**, *1186*, 117–122.

(17) Arnett, D. C.; Moser, C. C.; Dutton, P. L.; Scherer, N. F. *Laser Chemistry* **1999**, *19*, 161–164.

(18) Arnett, D. C.; Moser, C. C.; Dutton, P. L.; Scherer, N. F. *J. Phys. Chem. B* **1999**, *103*, 2014–2032.

(19) Diffey, W. M.; Beck, W. F. *Rev. Sci. Instrum.* **1997**, *68*, 3296–3300.

(20) Diffey, W. M. In *Department of Chemistry*; Vanderbilt University: Nashville, Tennessee, 2002.

(21) Edelstein, D. C.; Romney, R. B.; Scheuermann, M. *Rev. Sci. Instrum.* **1991**, *62*, 579–583.

(22) Wise, F. W.; Rosker, M. J.; Tang, C. L. *J. Chem. Phys.* **1987**, *86*, 2827-2832.

(23) Rosker, M. J.; Wise, F. W.; Tang, C. L. *Phys. Rev. Lett.* **1986**, *57*, 321-324.

(24) Diffey, W. M.; Homoelle, B. J.; Edington, M. D.; Beck, W. F. *J. Phys. Chem. B* **1998**, *102*, 2776–2786.

CHAPTER 3

DYNAMIC-ABSORPTION SPECTRAL CONTOURS: VIBRATIONAL PHASE-DEPENDENT RESOLUTION OF LOW-FREQUENCY COHERENT WAVE-PACKET MOTION OF IR144 ON THE GROUND-STATE AND EXCITED-STATE $\pi \rightarrow \pi^*$ SURFACES

3.0 Introduction

In this chapter, we develop a new procedure for phase-dependent visualization of vibrational coherence using dynamic-absorption contours. Using this method, we are able to characterize the ground-state and excited-state vibrational coherence in IR144. As discussed in chapter one, it is assumed that IR144's structure is invariant during the early solvent reorganization dynamics. This assumption is encouraged by a distinctive feature of IR144's structure, the central five-membered ring, which might be expected to inhibit *trans-cis* isomerization of the conjugated polyene. The results discussed in this chapter, however, suggest that IR144's structure evolves significantly during the first few vibrations following excitation. Based on ground-state electronic-structure and normal-mode calculations, we assign a strong 10-15-cm^{-1} feature to global modes involving torsion and deformation of the conjugated polyene. Excited-state wave-packet motion along these coordinates carry IR144 from its planar ground-state structure to one that is bent or twisted along the polyene backbone.

3.1 Experimental

3.1.1 Sample Preparation

IR144 (anhydro-11-(4-ethoxycarbonyl-1-piperazinyl)-10,12-ethylene-3,3,3',3'-tetramethyl-1,1'-di-(3-sulfopropyl)-4,5,4',5'-dibenzoindotricarbocyanine hydroxide, see figure 3.1) was obtained from Exciton and used as received. Samples for femtosecond spectroscopy were dissolved in methanol (Spectrum, spectrophotometric grade) to obtain an absorbance of 0.4–0.6 at 800 nm for a 1-mm path length; the IR144 solution was passed through a 0.22-μm filter prior to use.

3.1.2 Continuous-Wave Spectroscopy

Fluorescence spectra were obtained at room temperature, 23° C, with a home-built visible/near-IR spectrofluorimeter built around a liquid-nitrogen cooled CCD detector. Excitation light from a Jobin-Yvon AH10 quartz-halogen lamp was selected by a Spex 1681 monochromator, which was operated with a 4-nm spectral band pass. On its path to the sample's position, the excitation beam passed through a fused-silica optical fiber bundle, a Glan-Thompson calcite polarizer, and a 5-cm focal-length fused-silica focusing lens. The horizontal line of fluorescence emitted by the sample was collected at 90° from the direction of the excitation beam by a 5-cm focal-length fused-silica lens. In order to obtain dichroism-free spectra, a Glan-Thompson calcite polarizer analyzed the fluorescence beam at the magic angle, 54.7°, with respect to the plane of the excitation-beam polarizer. The transmitted fluorescence image was rotated to the vertical by a pair of silver mirrors and then focused onto the entrance slit of a Spex 270m spectrograph by a 5-cm focal-length fused-silica lens. The spectrograph was equipped with a

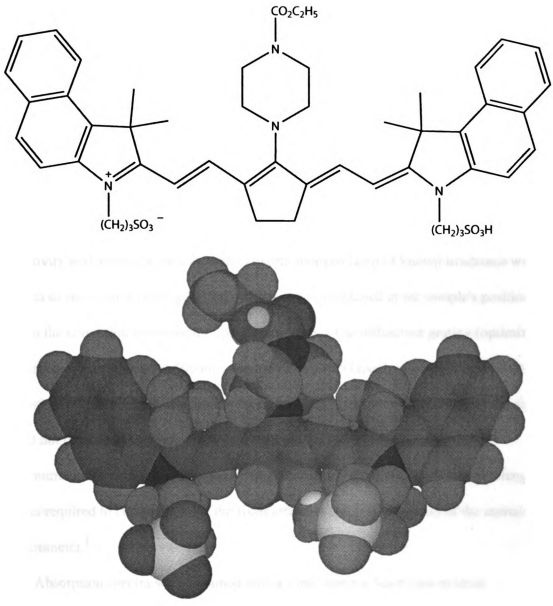

Figure 3.1. Structure of the all-*trans* configuration of IR144. The space-filling (CPK) representation is that of the energy-minimized structure obtained with the MM2 force field.

600-groove/mm ruled diffraction grating, which exposed the CCD detector to a 370-nm region of the emission spectrum. The 0.5-mm entrance slit set the spectrograph's effective band pass to 3.33 nm. The CCD system, a Spex SpectrumOne CCD detector and CCD2000 controller, employed an EEV 800 x 2048-pixel, back-illuminated spectroscopic CCD chip; Spex SpectraMax software was used for data acquisition.

Scattered light was removed from the fluorescence spectra through subtraction of a blank solvent-only spectrum that was recorded under the same measurement conditions with the same cuvette. The spectra were then corrected for the spectrofluorimeter's sensitivity with respect to wavelength; a quartz-halogen lamp of known irradiance with respect to emission wavelength (Ocean Optics) was employed at the sample's position to obtain the correction curve for the spectral response. The diffraction grating (optimized for first-order diffraction at 500 nm) and the silicon CCD (peak sensitivity in the 800-nm region) results in a rapidly decreasing signal/noise ratio in the 1000-nm region; the signal could not be used at wavelengths above 1050 nm. When plotted as a function of wavenumber, the fluorescence intensity was multiplied by the square of the wavelength, λ^2, as required to compensate for the fixed effective spectral band pass of the emission spectrometer.[1]

Absorption spectra were obtained with a 2-nm spectral band pass at room temperature, 22° C, with a Hitachi U-2000 spectrometer and LabVIEW (National Instruments) routines.

3.1.3 Femtosecond Spectroscopy

Dynamic-absorption spectroscopy was performed with two femtosecond pump–probe spectrometers built around self-mode-locked titanium–sapphire oscillators. The short-pulse apparatus was discussed previously in chapter two. The long-pulse, narrow-spectrum experiments employed a Mira 9000 oscillator (Coherent) that was equipped with X-wave broad-tuning-range cavity optics. The Mira 9000 oscillator was pumped by a Verdi (Coherent) 5-W laser and used at the natural pulse-repetition rate (76 MHz) without pulse selection. Extracavity pulse compression employed SF10 prisms. The long-pulse spectrometer also employed the rapid-scanning[2] modified Mach-Zehnder interferometer[3] of an improved design as discussed in chapter two. For the experiments presented in this chapter, the Murnane-Kapteyn oscillator was adjusted to produce 12-fs pulses ($sech^2$) with a band width of 820-cm^{-1} (fwhm) centered at 800 nm; the Mira 9000 oscillator was adjusted to produce 52-fs pulses ($sech^2$) with a band width of 250-cm^{-1} (fwhm) centered at 765 nm.

The IR144 sample was held at room temperature (22° C) in a fused-silica flow cuvette; the path length was 1 mm. The sample flow rate was 6 mL/min. The absorption spectrum of the sample was monitored for changes arising from photochemistry or permanent photobleaching.

3.2 Results

3.2.1 Continuous-Wave Spectroscopy

Figure 3.2 shows the absorption and fluorescence spectra exhibited by IR144 in methanol solvent at room temperature. The spectra are plotted as $A(\nu)/\nu$ and $F(\nu)/\nu^3$, respectively, with normalization to unit area. The integrals of these quantities report the dipole strength,[1,4] the square of the transition-dipole moment, which is proportional to the Einstein coefficients for absorption and stimulated emission, B_{ab} and B_{ba}, respectively. As plotted, the sum of the spectra can be compared to the time-integrated dynamic-absorption spectrum in the weak-field limit.[5] The fluorescence spectrum exhibits some partially resolved vibronic structure; no structure is observed in the absorption spectrum. The 0–0 vibronic transition occurs in the vicinity of 12400 cm^{-1} (806 nm), where the two normalized spectra cross.

In the short-pulse (12-fs $sech^2$) dynamic-absorption experiments, the titanium-sapphire laser's spectrum (11300–13333 cm^{-1}, with peak intensity at 12500 cm^{-1}) excites IR144 over a spectral range that starts to the red of the absorption maximum, passes the 0–0 transition, and proceeds on to cover the red onset. The laser spectrum then spans a great deal of the fluorescence spectrum. Accordingly, as used in the dynamic-absorption experiments as the probe beam, the laser spectrum covers much of the stimulated-emission spectrum and only the red onset of the ground-state depletion spectrum.

3.2.2 Short-Pulse Dynamic-Absorption Experiments

Figure 3.3 shows a three-dimensional mesh-surface view of a portion of the dynamic-absorption intensity-delay-wavelength surface from IR144 in methanol. A set of

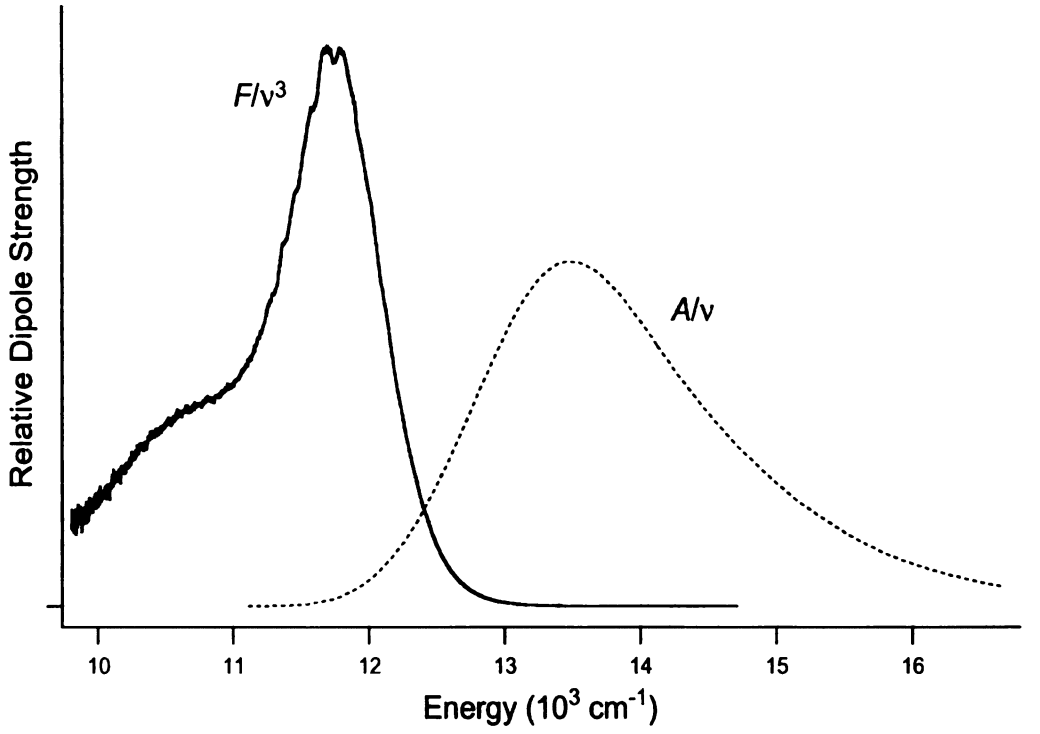

Figure 3.2. Continuous-wave absorption and fluorescence spectra from IR144 in methanol plotted as relative dipole strengths, A/ν and F/ν^3, respectively. The spectra are normalized to unit area. The fluorescence spectrum was excited at 790 nm (12600 cm^{-1}).

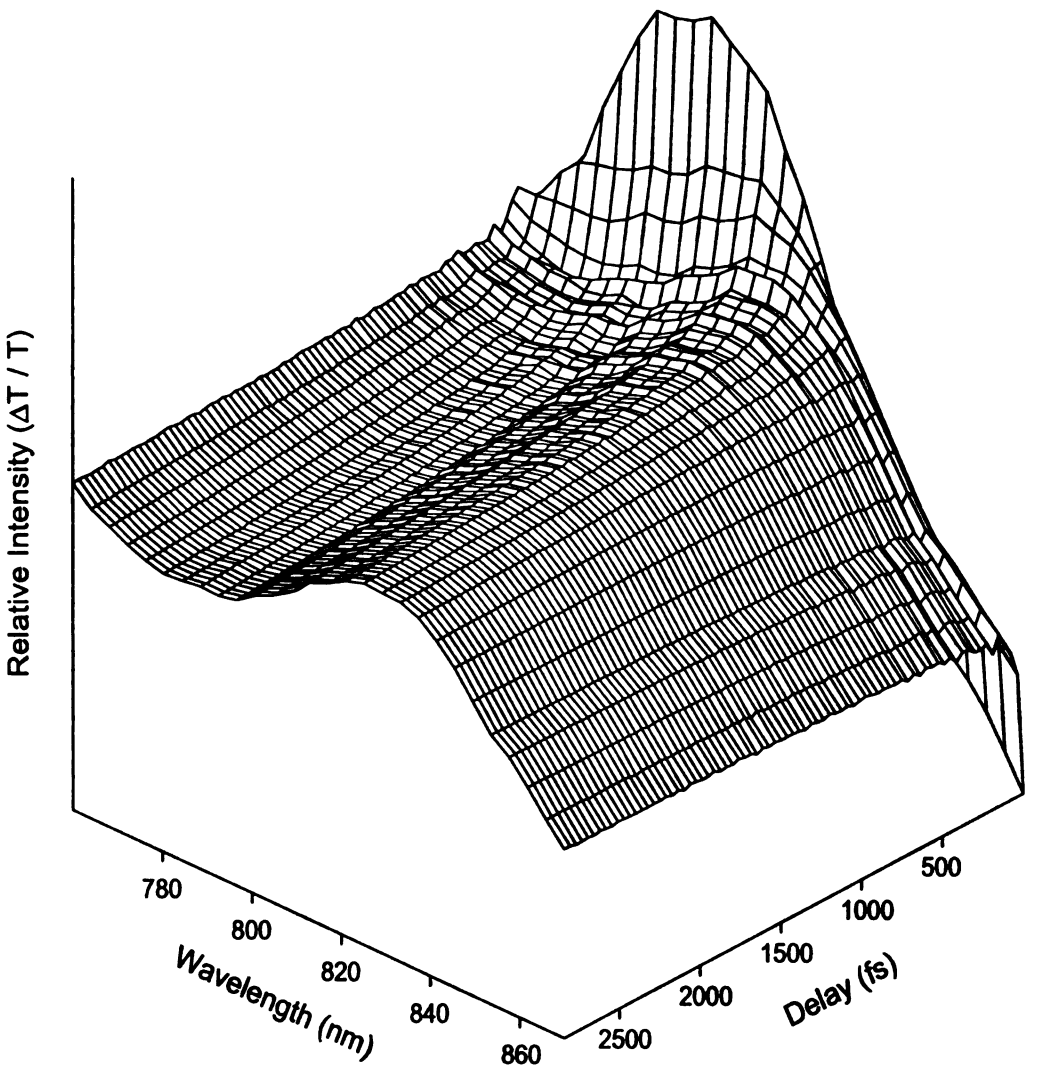

Figure 3.3. Dynamic-absorption spectrum obtained with 12-fs pulses centered at 790 nm from IR144 in methanol.

single-wavelength pump-induced transmission ($\Delta T/T$) transients was recorded over a 110-nm range of probe wavelengths; the spacing of the probe wavelengths matched the monochromator's spectral band pass (4 nm). Initially the dynamic-absorption spectrum exhibits a hole-burned character, with the overall width far less than anticipated from the sum of the absorption and fluorescence dipole-strength line shapes (see figure 3.4, right panel). Within 100 fs the spectrum splits into two partially resolved peaks, from ground-state depletion and from stimulated emission, and broadens to close to the anticipated width. The stimulated-emission spectrum is well red-shifted compared to the initial position of the hole spectrum; it exhibits a peak near the position of the fluorescence maximum by the 2-ps delay point.

The main panel of figure 3.4 shows a contour representation of IR144's dynamic-absorption surface. The contour plot was obtained from the 4-nm x 1.8-fs data grid using default settings in the program Igor Pro (Wavemetrics). The program employed bilinear interpolation to obtain a square high-resolution grid; interpolation along the longer of the two grid axes, the delay axis, was not required. From this grid, contour lines were constructed at 40 discrete intensity levels; the intensity levels were evenly spaced over the full range of intensities in the data set. Similar contour lines were obtained, though with lower signal/noise ratio, with data sets recorded with 2-nm resolution and spacing.

The contour lines exhibit wavelength oscillations with respect to the delay axis. These oscillations are not as prominent in the mesh-surface representation owing to their relatively low amplitude. The wavelength oscillations are clearly grouped into sets of contour lines with the same phase. Near flat portions of the surface (see figure 3.3), the

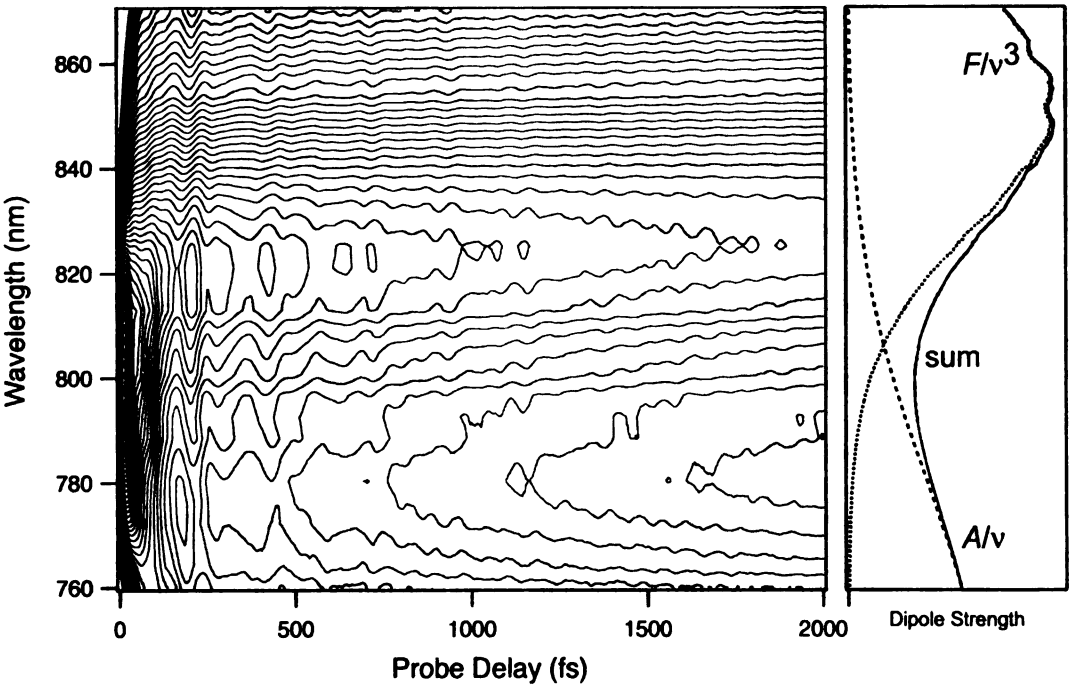

Figure 3.4. Contour representation of the dynamic-absorption spectrum obtained from IR144 in methanol. The right-hand panel shows the continuous-wave fluorescence-emission spectrum (dotted line), the absorption spectrum (dashed line), and their sum (solid line) plotted as relative dipole strengths on the same wavelength scale.

contour lines break off; on slanted portions of the surface it is possible to observe continuous runs of oscillations spanning at least the 0–5000-fs delay range.

Four sets of contour lines with alternating phase are observed in figure 3.4 as one scans from one wavelength limit to the other. One set runs from the 870-nm red limit of the surface to the stimulated-emission peak-maximum region, 830 nm. A second, oppositely phased set ranges from 810 nm to the 780-nm region. The phase inverts again for the set of contour lines that begins at 775 nm and runs to 765 nm. A fourth set is only partially observed at the 760-nm blue limit of the probe spectrum.

Two transients from the data set used to build the dynamic-absorption surface are shown in figure 3.5. Intensity oscillations are observed over the 200–5000-fs delay range. The 864-nm transient is chosen from the spectral region covered by the set of contour lines at the red limit of the probe spectrum. The 808-nm transient is chosen from the spectral range covered by the oppositely phased set of contour lines that lies below the first set. The biexponential falling and rising trends that follow the zero-time pump–probe interaction region in the 808-nm and 864-nm transients, respectively, show the effects of dynamic solvation on the stimulated-emission spectrum (see figure 3.3); excited-state population decay occurs on a much longer time scale. In the following, we examine in more detail the information content carried in the wave-packet oscillations detected in these two spectral regions.

Figure 3.6 shows an expanded view of the oscillatory part of two contour lines selected from the set shown in figure 3.4. The contour lines were those centered approximately at 808 nm and at 864 nm, the wavelength regions probed by the two transients in figure 3.5. The oscillatory part of each contour line was obtained by

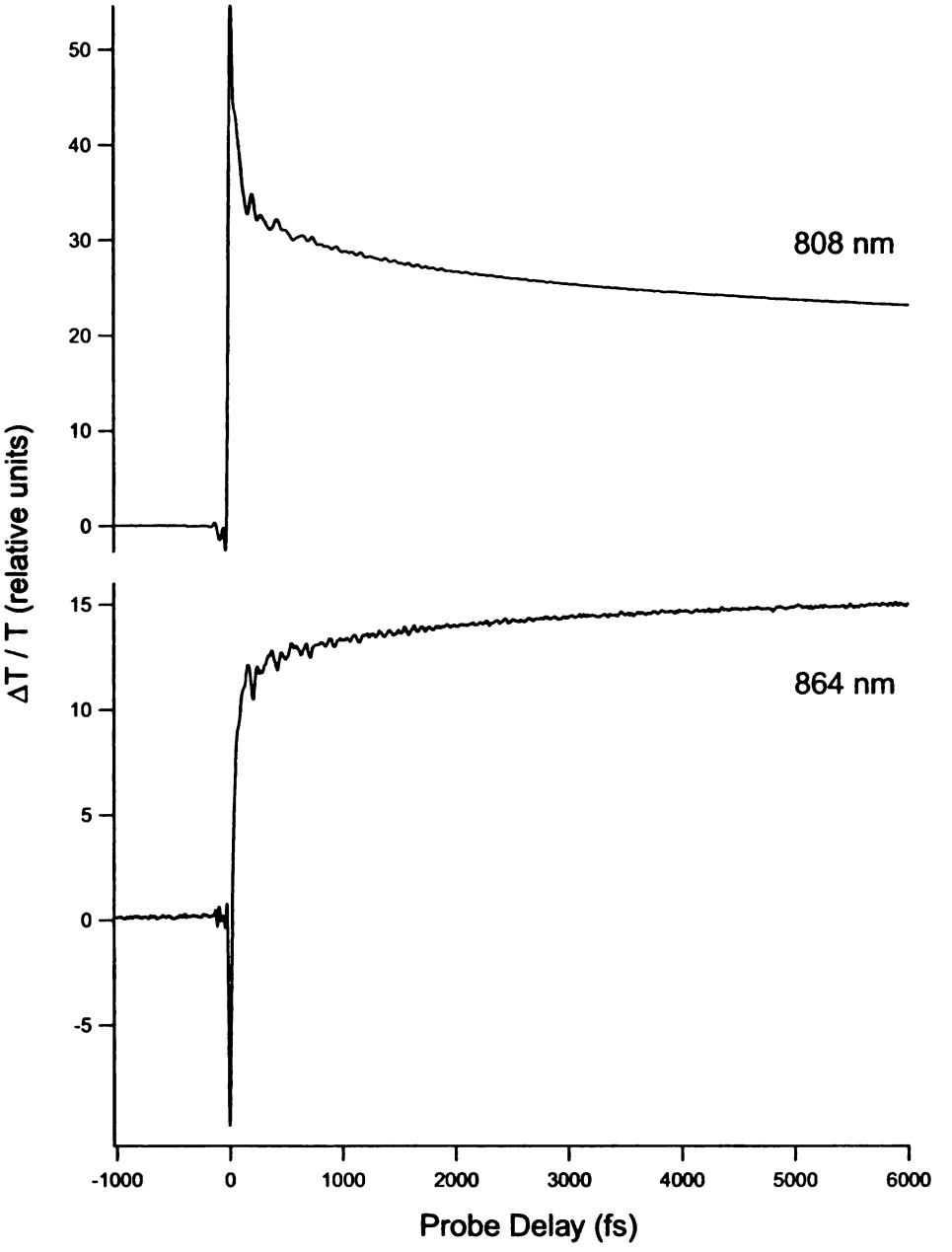

Figure 3.5. Dynamic-absorption transients obtained from IR144 in methanol, with the transmitted probe light detected at 808 nm and 864 nm. The maximum signal for the 808-nm transient corresponds to $\Delta T/T = 10^{-4}$.

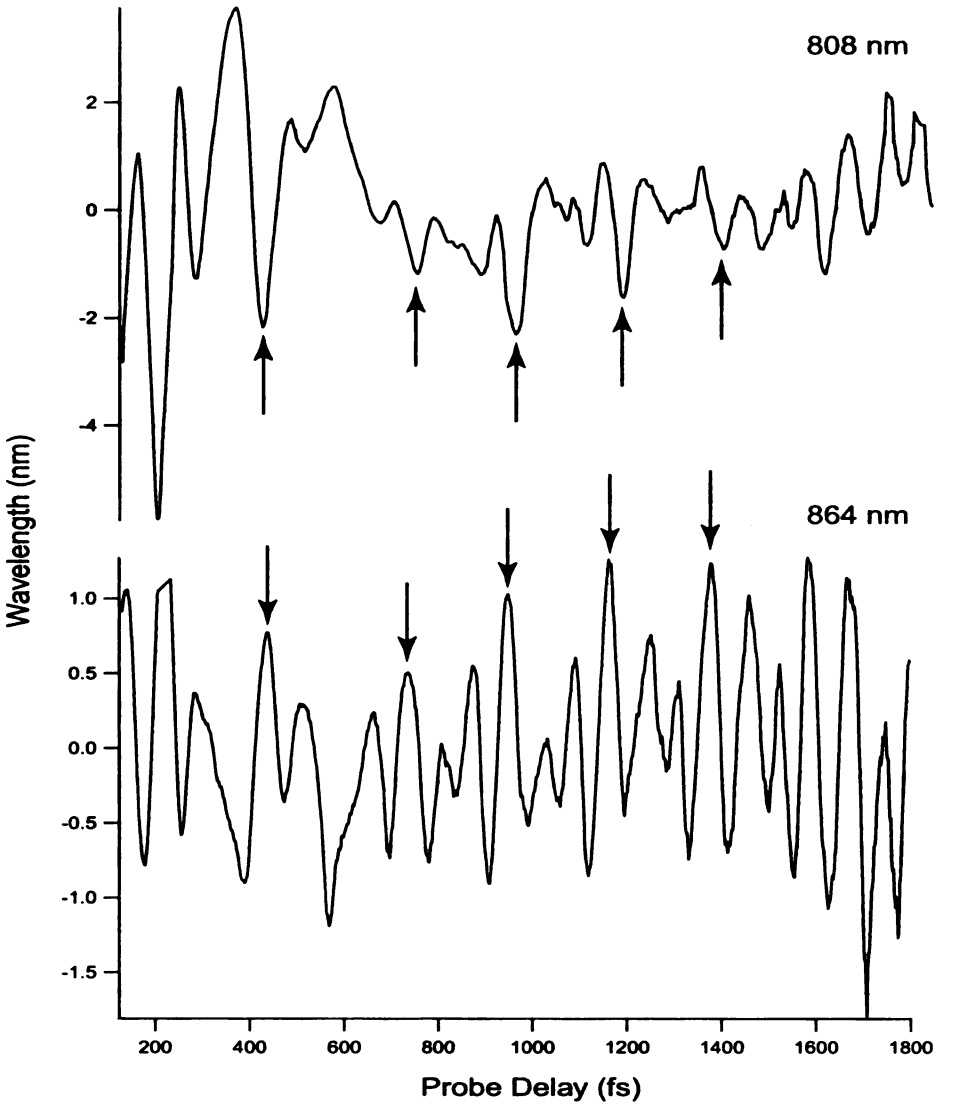

Figure 3.6. A delay-expanded view of a section of the oscillatory signals obtained from the contour lines centered at 808 nm and at 864 nm in the dynamic-absorption spectrum from IR144 in methanol. These contour lines were selected from the set shown in figure 3.4. In order to illustrate the antiphase character of the two contour lines, arrows mark several extrema at approximately the same delay times.

subtracting a fitted double-exponential baseline function. The fit started at a delay past the initial fast decay or rise transient (~150 fs, see figure 3.5) and extended to the end of the signal.

Figure 3.6 shows that the 808-nm and 864-nm contour lines exhibit the same oscillatory features but with almost perfectly opposite phases. The arrows in figure 3.6 mark extrema in the two traces that occur nearly at the same delay point; notice that the antiphased features gradually separate in time, with the 808-nm trace trailing the 864-nm trace. The 808-nm trace also includes an obvious low-frequency oscillation, with a maximum swing at 400 fs and a minimum swing at 1000 fs, which is not as apparent in the 864-nm trace.

3.2.3 Fourier-Magnitude Spectrum Estimation

The next four figures present a Fourier analysis of the oscillatory components observed in transmission-intensity transients and contour lines at the 808-nm and at 864-nm probe wavelengths. The oscillatory part of each signal was obtained by subtracting a fitted double-exponential baseline function. The oscillatory segment over the 150–4000-fs delay range was multiplied by a Hanning (or raised cosine) window function,[6]

$$\omega(k) = 0.5\left[1 - \cos\frac{2\pi k}{n+1}\right] \tag{3.1}$$

defined for the point index k in the data segment in terms of the number of data points n. The window function gradually forces the intensity at the beginning and end of the signal segment to zero amplitude. This procedure is required to suppress satellite ripples in the

Fourier-magnitude spectra, which arise from leakage of signal frequencies into adjacent channels owing to truncation of the time-domain signal at the beginning and end. Lastly, the windowed signals were zero-padded by a factor of 32 in order to enhance the point density along the frequency axis in the Fourier-magnitude spectra.

Figure 3.7 shows that the oscillatory signals observed in the 808-nm region of the dynamic-absorption spectrum arise from rapidly damped low-frequency components and from high-frequency components that persist well past the 4000-fs delay mark. The contour line exhibits a strong low-frequency component that is not as strongly displayed in the transient. The Fourier-magnitude spectra obtained from the contour and transient are shown in figure 3.8. The main difference between the two spectra is the strength of the 15-cm^{-1} peak, which is much more intense in the spectrum derived from the contour line. At least eleven components with reproducible position, width, and intensity are observed over the 10-800-cm^{-1} frequency range.

Similar modulation frequencies contribute to the 864-nm region of the dynamic-absorption spectrum. The oscillatory signals obtained from the transient and contour line (see figure 3.9) are almost identical, but again the Fourier-magnitude spectra shown in figure 3.10 evidence a stronger component at 15 cm^{-1} in the contour line. Compared to the strength of the 450-cm^{-1} components, however, the 15-cm^{-1} components detected at 864 nm are substantially weaker than observed at 808 nm (see figure 3.8).

In order to obtain reliable estimates for intensities and damping times, we modeled the experimental Fourier-magnitude spectra obtained from the contour lines at 808 nm and 864 nm using a sum of damped cosines,

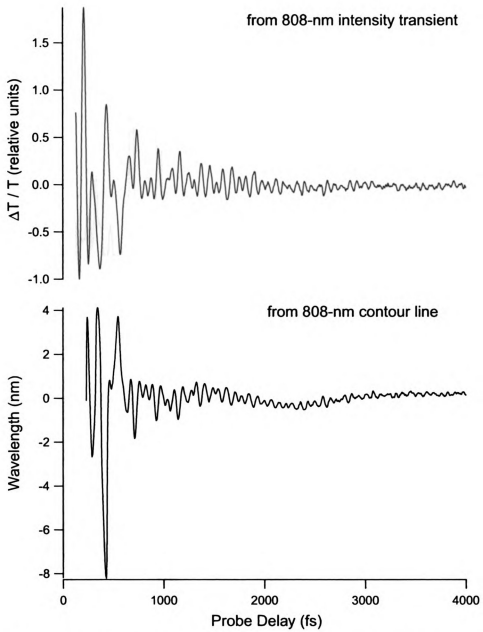

Figure 3.7. Comparison of the oscillatory components observed at 808 nm from the intensity transient (upper graph) and from the 808-nm contour line (lower graph) obtained from the dynamic-absorption spectrum from IR144 in methanol (see figure 3.4).

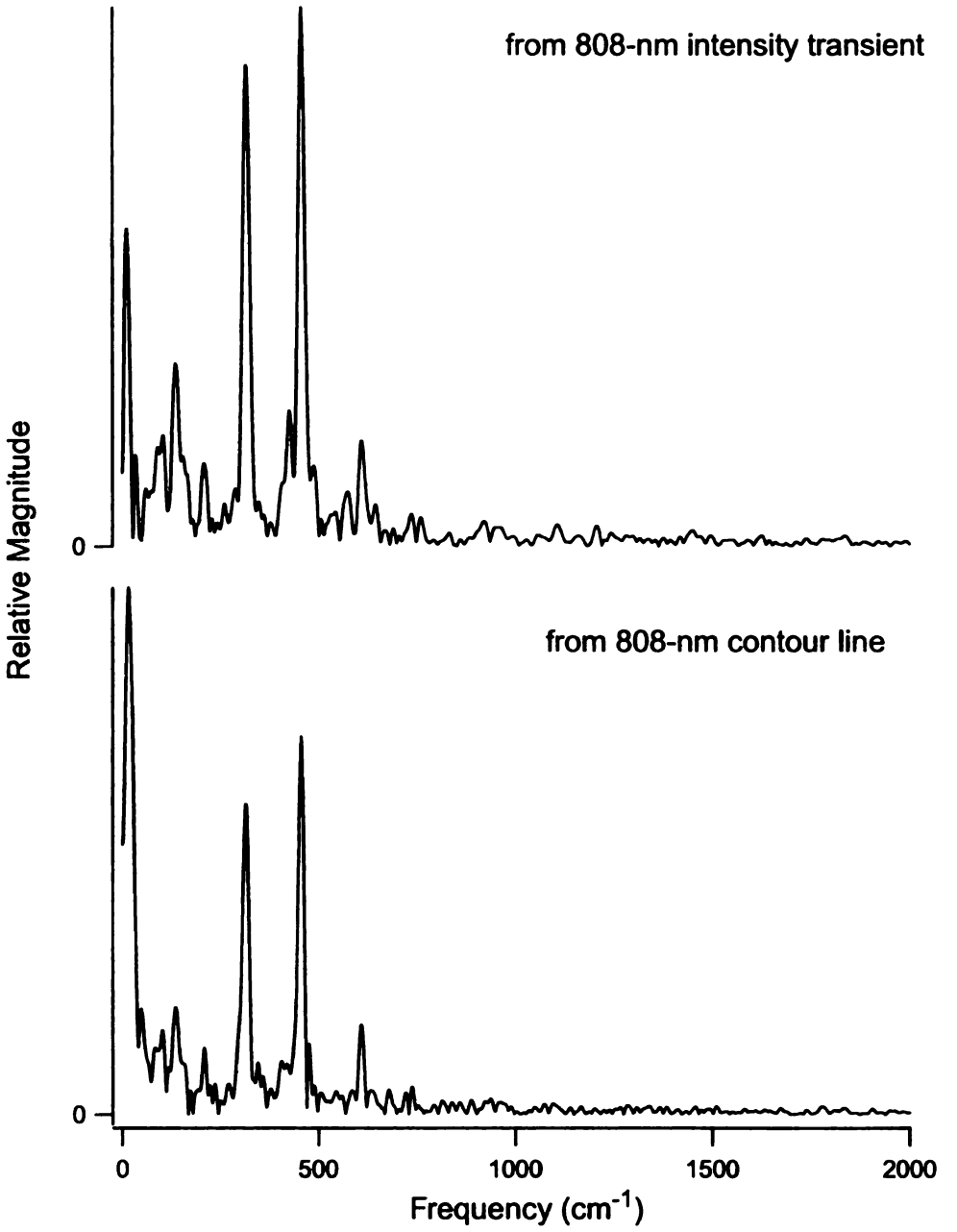

Figure 3.8. Comparison of the Fourier-transform magnitude spectra obtained from the oscillatory components observed at 808 nm, as shown in figure 3.7, from the intensity transient (upper graph) and from a contour line (lower graph) obtained from the dynamic-absorption spectrum from IR144 in methanol.

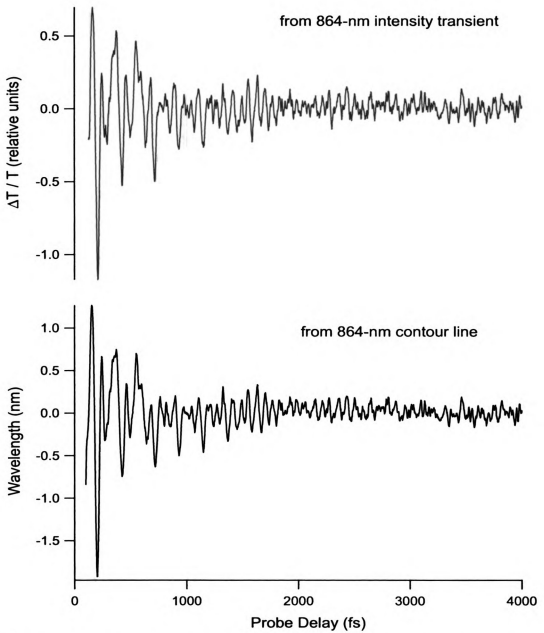

Figure 3.9. Comparison of the oscillatory components observed at 864 nm from the intensity transient (upper graph) and from the contour line (lower graph) obtained from the dynamic-absorption spectrum from IR144 in methanol.

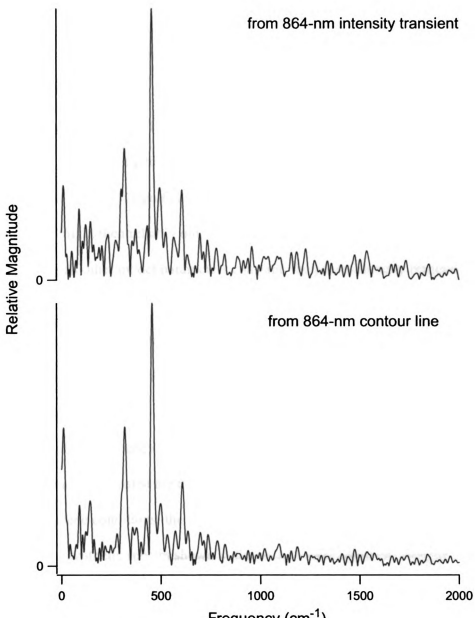

Figure 3.10. Comparison of the Fourier-transform magnitude spectra obtained from the oscillatory components observed at 864 nm, as shown in figure 3.9, from the intensity transient (upper graph) and from a contour line (lower graph) obtained from the dynamic-absorption spectrum from IR144 in methanol.

$$I(t) = \sum_i A_i \exp\left(-\frac{t}{\gamma_i}\right) \cos(\omega_i t + \phi_i) \tag{3.2}$$

The model signal was sampled using the delay times t and segment lengths obtained from the experimental contour signals; it was processed by the same sequence of windowing, zero-padding, and Fourier-magnitude spectrum calculation. The intensities A_i, frequencies ω_i, and damping times γ_i were adjusted iteratively to reproduce the intensity, position, and width of each significant feature in the experimental Fourier-magnitude spectrum. (One might then reliably obtain the phases ϕ_i by optimization in the time domain, leaving all other model parameters constant; the phases directly retrieved from a Fourier analysis of the contour lines or transients are strongly affected by signal noise.) The optimized parameters are listed in table 3.1. The intensities listed in the table were compensated for the finite width of the instrument-response function by deconvolution in the frequency domain: the raw optimized amplitudes were scaled by the reciprocal of the Fourier magnitude at frequency ω_i obtained from the pump–probe autocorrelation signal.[7] The components listed are the ones that were reproduced in several experimental trials under the same conditions; the uncertainties reflect the range of observed frequencies. The synthetic spectra shown in figure 3.11 were obtained from the tabulated model parameters using a sum of Lorentzian line shapes.[8]

$$I(\omega) = \sum_i \frac{A_i}{4\gamma_i^2(\omega - \omega_i)^2 + 1} \tag{3.3}$$

Note that an assumption of Lorentzian line shapes results in a model that damps somewhat more rapidly (especially for the higher-frequency components, such as the one at 456 cm^{-1}) than is actually observed.

Table 3.1. Frequencies, normalized intensities, and damping constants for modulation components observed in contour lines at 808 nm and 864 nm from the dynamic-absorption spectrum of IR144 in methanol.

	808-nm contour		864-nm contour	
frequency (cm^{-1})	intensity[a]	γ (fs)	intensity[a]	γ (fs)
15 ± 6	2.30	600	0.15	800
96 ± 6	0.05	1300	0.03	1300
138 ± 6	0.23	500	0.29	500
273 ± 6	0.26	700	0.10	700
317 ± 2	0.80	750	1.98	500
353 ± 6	0.14	1000	0.07	1000
456 ± 2	1.00	1000	1.00	1000
483 ± 7	0.28	1300		
500 ± 8	0.15	1300		
501 ± 3			0.21	500
525 ± 6			0.12	1300
609 ± 2	0.37	1100	0.68	900
634 ± 2	0.46	500	0.36	1000

[a] Relative to the intensity of the 456-cm^{-1} mode after deconvolution in the frequency domain.

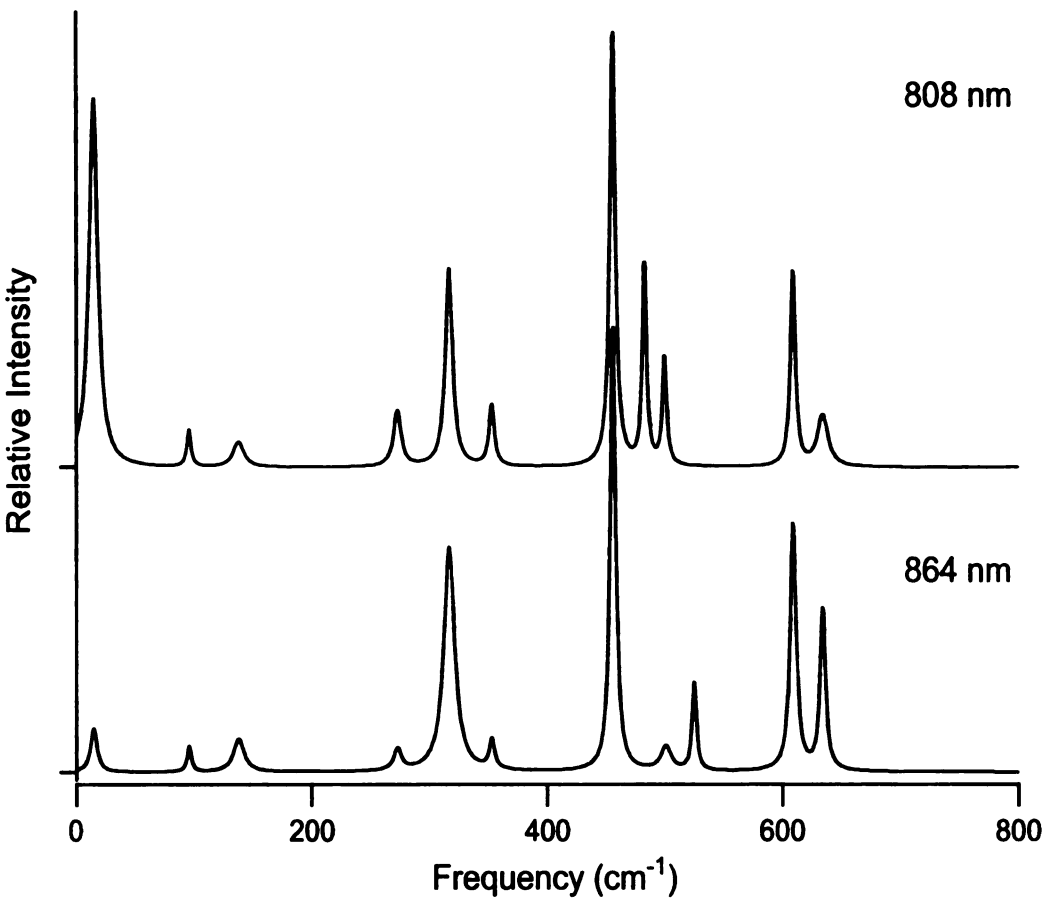

Figure 3.11. Synthetic spectra describing relative magnitudes, frequencies, and damping times for modulation components observed in the contour lines centered at 808 nm (top graph) and 864 nm (bottom graph) in the dynamic-absorption spectrum of IR144. Lorentzian line shapes were employed for each modulation component. The parameters for these spectra are listed in table 3.1.

The synthetic spectra shown in figure 3.11 represent the best estimates for the modulation frequencies, intensities, and damping times for the coherent wave-packet motions of IR144 that would be retrieved by Fourier analysis if it were possible to determine the spectrum from an infinitely long segment of data obtained from an experiment with delta-function pump pulses. The windowing function causes a significant quenching of signal components below 50 cm^{-1} for the 4000-fs signal length used here: compared to the frequency and peak height obtained directly from the Fourier-magnitude spectrum by inspection, the retrieved frequency is shifted a few wavenumbers higher and the retrieved intensity is significantly larger (compare figure 3.11 with figure 3.8, as an example). Further, the window function causes an inverse scaling of the width of the peaks in the Fourier-magnitude spectrum with respect to the analyzed segment length; longer segments retrieve narrower peaks, but the signal/noise ratio degrades as the delay time increases owing to the damping of the oscillations. The frequency-domain spectral-estimation method used here is robust; in the absence of signal/noise limitations, the returned parameters are independent of the choice of analyzed signal length.

3.2.4 Long-Pulse Dynamic-Absorption Experiments

In order to probe the ground-state depletion portion of the dynamic-absorption spectrum somewhat farther to the blue than was possible in the short-pulse experiments, we performed a set of experiments with pulses of 52-fs ($sech^2$) duration and 11.5-nm spectral width from the Mira 9000 oscillator, which can be tuned well to the blue of the maximum of the fixed spectrum of our Murnane-Kapteyn oscillator. These experiments also provide a clearer view of the low-frequency wave-packet oscillations because the

high-frequency components that dominate the signals obtained with short pulses are not impulsively excited.

Figure 3.12 shows the dynamic-absorption transient, its oscillatory components, and Fourier-magnitude spectrum obtained from a pump spectrum centered at 765 nm and transmitted probe light monitored at 758 nm. Three strong components, at 15 cm^{-1}, 90 cm^{-1}, and 130 cm^{-1}, are observed in the Fourier-magnitude spectrum; high-frequency modulation components, above 220 cm^{-1}, are not observed reproducibly. The frequencies, intensities, and damping times for the oscillatory components were retrieved using the procedure described in the previous section of the paper. The results are similar to those obtained for the 808-nm contour or transient in the short-pulse experiment. It is notable that the intensity for the 15-cm^{-1} component is more intense than that for the 130-cm^{-1} component, which mirrors the result obtained with 12-fs pulses from the 808-nm contour (see figure 3.8 and table 3.1) but not that from the 864-nm contour (see figure 3.10).

An additional experiment was conducted with the pump spectrum centered at 750 nm and the transmitted probe light monitored at 743 nm. These settings probe the ground-state wave-packet motion even farther to the blue but the vibrational level that is prepared on the excited-state surface is higher up in energy. The results we obtained (not shown) are very similar to those in figure 3.12, but the signal/noise ratio is not as high.

3.2.5 Simulations

The amplitude-modulated part of the dynamic-absorption spectrum observed from IR144 arises from an interference pattern produced by the partial spectral overlap of the stimulated-emission and ground-state depletion spectra. In the following, we show how

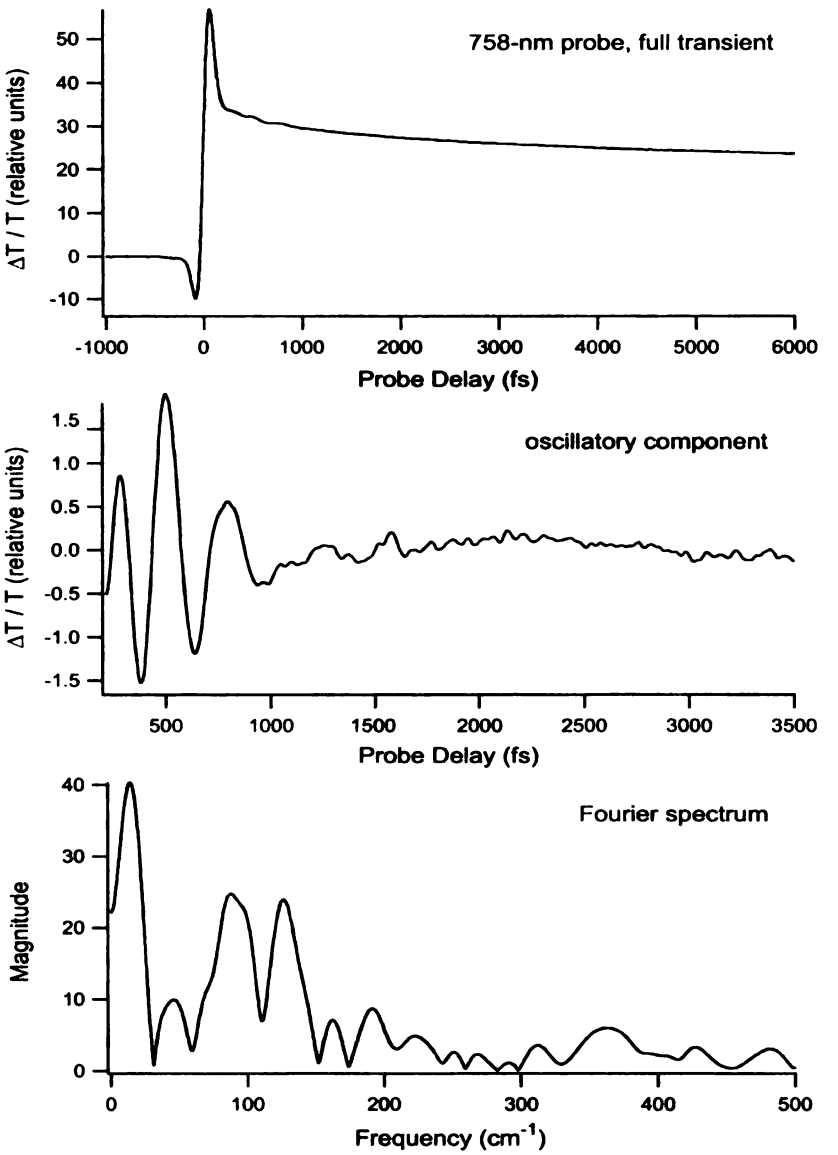

Figure 3.12. Narrow-spectrum, long-pulse (52-fs) pump–probe transient (top), oscillatory component (middle), and Fourier-magnitude spectrum (bottom) obtained from IR144 in methanol. The pump spectrum and transmitted-probe band pass were centered at 765 nm and 758 nm, respectively. The delay window used for the Fourier transform was 3500-fs wide.

the phases of the excited-state and ground-state wave packets that give rise to the modulated spectra can be discerned by inspection of a contour representation of the dynamic-absorption spectrum. The reader is referred to work by Pollard and Mathies,[5] Chachisvilis *et al.*,[9-11] and Nagarajan[12] for a discussion of the nonlinear optics and solvent-bath coupling aspects of the problem. We discuss in the following using a simple theory the spectral interference that would be produced by a cosinusoidal motion of two line shapes with respect to the ground-to-excited-state energy gap at one or more vibrational frequencies. The results mimic several aspects of the experimental dynamic-absorption spectra from IR144 that are discussed in this paper.

The stimulated-emission signal I arising at a certain time t and observation frequency ω from a single wave packet on the excited-state surface can be described parametrically by a line-shape function, an oscillating equation of motion, and a phase distribution. We use here a Gaussian shape of constant intrinsic intensity A and half-width σ:

$$I(\omega, t) = A\sum_i N(\phi_i)\exp\left(-\frac{\omega - -\omega_{0i}(t)}{2\sigma^2}\right) \tag{3.4}$$

The intensity A scales with the energy of the pump pulse; the width σ can be taken as arising from homogeneous line broadening and the temperature-dependent breadth of the initial vibrational-state distribution. In order to obtain a damped modulation of the spectrum, the sum is taken over an ensemble of molecules described by a normalized phase distribution $N(\phi_i)$, defined here as a Gaussian that expands in width exponentially with time; the time constant used arbitrarily in the simulations produces an effective intensity-damping time of 1.2 ps. The center frequency ω_{0i} for the molecules in the ensemble with phase ϕ_i oscillates cosinusoidally with respect to ω as

$$\omega_{0i}(t) = \Delta\cos(\omega_v t + \phi_i) \tag{3.5}$$

For a certain vibrational level v, the energy gap for the most probable transition to the other state's potential-energy surface is effectively cosinusoidally modulated as a function of the vibrational coordinate owing to the variation in Franck-Condon factors. The amplitude parameter Δ corresponds to the resonance Raman cross section, which is proportional to the square of the dimensionless displacement of the excited-state vibrational coordinate for Albrecht *A*-term active modes. Without some displacement, the spectrum is not modulated with respect to the vibrational coordinate.[8]

In the first simulation, the mode frequency ω_v was set arbitrarily to 200 cm^{-1}; the amplitude Δ was set to be one-third of the half-width $\sigma = 1$. This choice produces a broad spectrum with a relatively small modulation depth due to wave-packet motion, which resembles the situation at room temperature in IR144. The intensity surface $I(\omega, t)$ was built as a 400×400 grid of intensities that was calculated as a series of time-resolved spectra with 5 fs spacing over the 0–2000-fs range.

The contour-plot representation of the stimulated-emission intensity surface, figure 3.13, can be described as a set of cosinusoidally modulated contour lines that exhibit the same phase. The Fourier-magnitude spectrum of one of the contour lines, as calculated using the methods described above, consists of a peak at the fundamental frequency and a series of progressively much weaker peaks at the harmonics (see figure 3.14, where only the first harmonic at 400 cm^{-1} is barely visible with the fundamental plotted at full scale).

Figure 3.15 shows that similar Fourier-magnitude spectra with strong fundamentals and much weaker harmonics are obtained from intensity transients obtained as slices

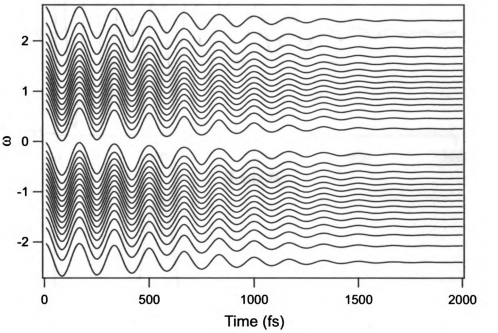

Figure 3.13. Contour-plot representation of the modulated stimulated-emission spectrum arising from the 200-cm^{-1} vibrational motion of a single damped wave packet. The parameters for the calculation are described in the text.

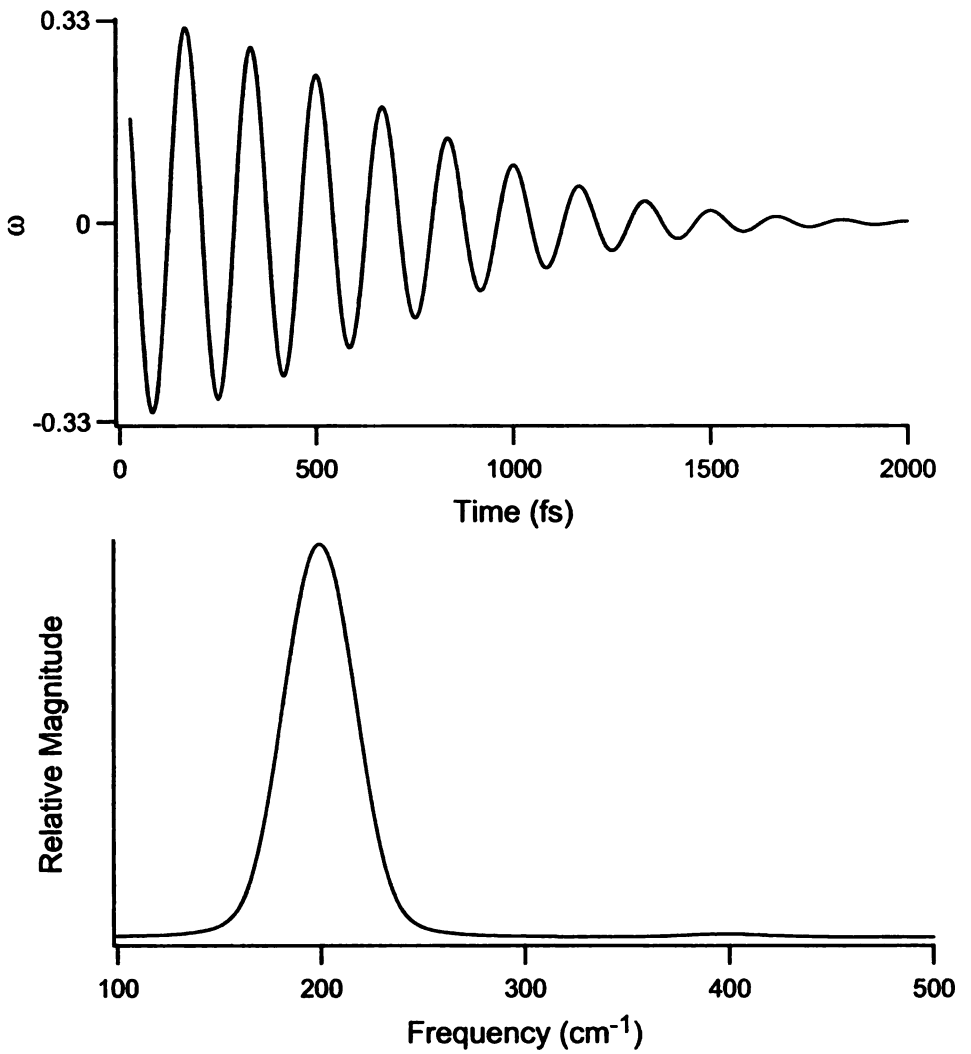

Figure 3.14. A single contour line selected from the set shown in figure 3.13 at $\omega = -1$ and its Fourier-magnitude spectrum (bottom panel).

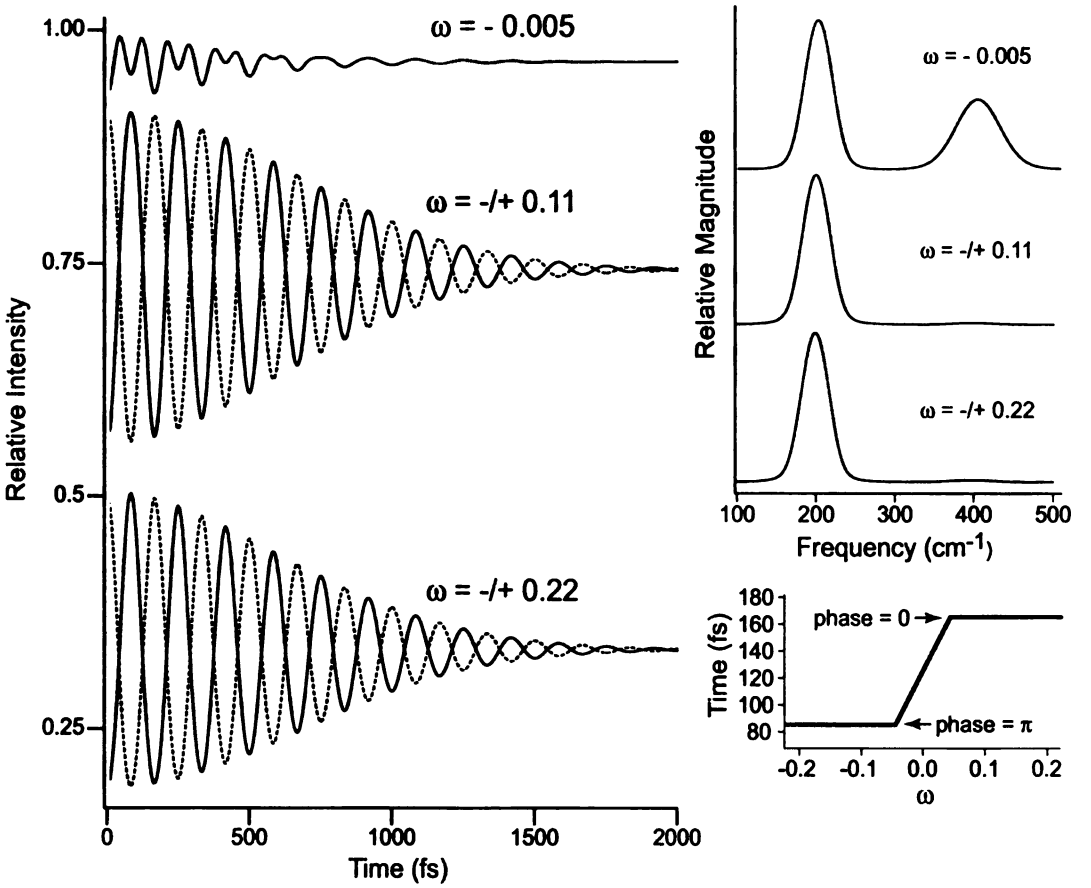

Figure 3.15. Transients obtained from the spectrum shown in figure 3.13 at a set of discrete observation frequencies ω. Where pairs of transients are superimposed, solid curves correspond to $\omega < 0$ and dashed curves correspond to $\omega > 0$. The Fourier-magnitude spectra corresponding to the transients are shown to the right. The lower right-hand figure plots the first positive-going recurrence time as a function of ω.

across the $I(\omega, t)$ surface at selected observation frequencies ω. Near the center of the spectrum, however, the transients exhibit a much more intense second-harmonic component. Indeed, the wave packet crosses the observation frequency twice per mode period, but the modulation depth at the second-harmonic frequency is not very large except at the center of the spectrum. This behavior has been previously discussed.[10,13,14]

Also shown in figure 3.15 is the intensity-phase behavior of the transients. Recurrences occur at fixed times, independent of ω; near the center of the spectrum, however, the recurrence times scan rapidly from one phase limit to the other and produce a π phase shift. This aspect of the dynamic-absorption spectrum has been discussed in much of the previous work.[13,15-18] If the narrow spectral region where the phase shift occurs lies outside the probed region or is obscured by a spectral overlap, a plot of the phase as a function of ω might be difficult to interpret.[19] In contrast, the constant contour-phase signature arising from a single wave packet's motion can be observed over most of the probe region spanned by the spectral motion.

Figure 3.16 shows the results obtained when a second modulation component is introduced. The calculation was performed as the sum of in-phase components with modulation frequencies at 200 and 120 cm^{-1} and relative intensities of 1 and 0.75, respectively; the other parameters were the same as in the first simulation. The resulting $I(\omega, t)$ surface exhibits contour lines with two modulation components, as one might expect. It can be shown that the magnitudes obtained from a Fourier analysis of the contour lines return the product of the amplitude Δ (equation 3.5) and the intensity-scaling factor A (equation 3.4). The Fourier-magnitude spectra obtained from single-frequency intensity transients are similar to those obtained from the contour lines.

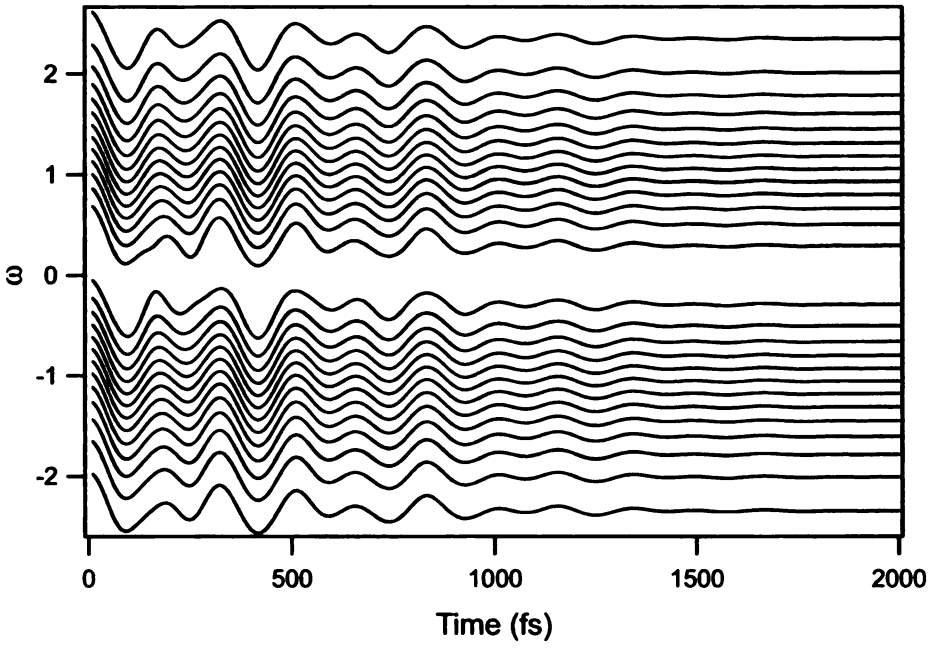

Figure 3.16. Contour-plot representation of the modulated stimulated-emission spectrum arising from the motion of a damped wave packet with two modulation components, at 200 cm^{-1} and 120 cm^{-1} and relative intensities of 1 and 0.75, respectively. The parameters for the calculation are otherwise as used for the simulation shown in figure 3.13.

Lastly, figure 3.17 shows the spectral interference arising from the in-phase motion of two wave packets with the same frequency (200-cm^{-1}) and intensity, one on the excited state and one on the ground state. In this simulation, we used equation 3.5 as defined above to control the motion for the stimulated-emission spectrum. The equation of motion for the ground-state depletion spectrum is essentially the negative of that used for the stimulated-emission spectrum,

$$\omega_{0i} = \omega_G - \Delta\cos(\omega_v t + \phi_i) \tag{3.6}$$

The ground-state wave packet absorbs probe photons, so the cosinusoidal motion of its signal with respect to ω is opposite in sense to that contributed by the excited-state wave packet's gain.[20,21] For this simulation, the ground-state and excited-state signals are offset along the ω axis by the parameter $\omega_G = 1$.

The resulting intensity surface exhibits a set of contour lines with four alternating phase regions. As one scans in figure 3.17 from the lower ω limit, one encounters a continuous set of contour lines with the same phase that arises from the excited-state wave packet. A similar set of lines arising from the ground-state wave packet is observed starting from the upper ω limit, but the phase is inverted with respect to the phase of the opposite set of contour lines. The observed phase reports which of the two wave-packet signals is the larger one at a particular ω. But in the center of the spectrum, the contour phase inverts twice, producing two narrow regions of opposite phase. These regions arise from the narrowing of the wave packet's spectral breadth as it changes its direction of motion; the resulting relatively sharp intensity modulation causes the turning wave packet's signal to surpass that of the other. Note that these turning-point regions were observed in the spectroscopic simulations by Pollard and Mathies[5,22] even in the limit of

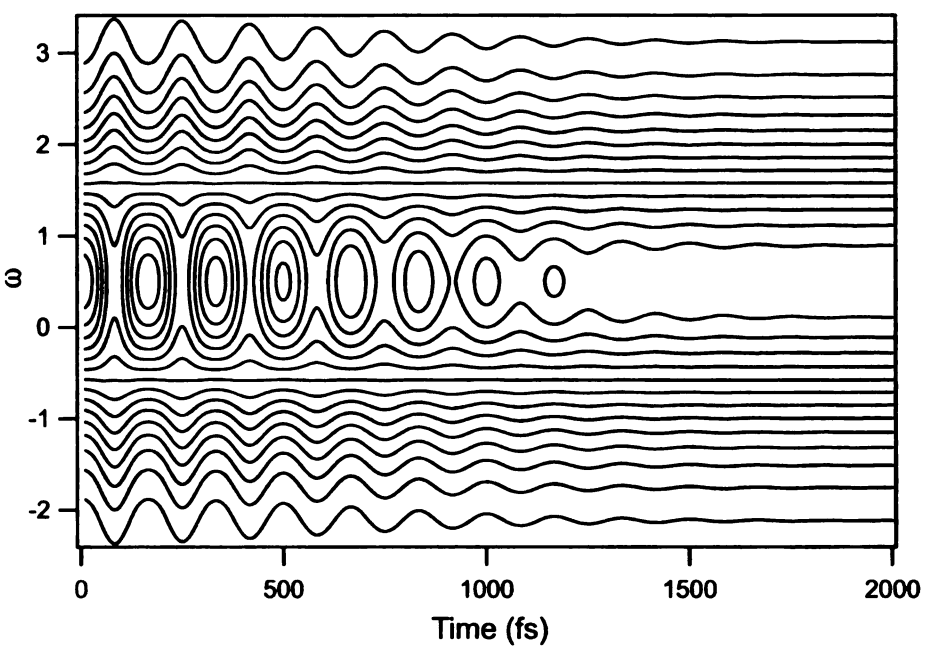

Figure 3.17. Contour-plot representation of the sum of the modulated stimulated-emission and ground-state depletion spectra arising from two damped wave packets, one moving on the excited-state surface and one moving on the ground-state surface. Both spectra are modulated by the same 200-cm^{-1} component but they move with opposite sense with respect to the observation-frequency axis, ω. The parameters for the stimulated-emission spectrum are as used for the spectrum shown in figure 3.13; the antisense (ground-state) spectrum is offset along the ω axis from the first wave packet by +1 unit.

purely harmonic motion; they arise in our simulations analogously from the phase distribution $N(\phi_i)$. The turning-point spectral regions that contribute to the phase alternation in the center of the dynamic-absorption spectrum arise from the short-displacement and long-displacement turning points of the excited-state and ground-state wave-packet motion, respectively. The other two turning-point spectral regions would be found in the clear (not overlapped with the signal from the other wave-packet) high-frequency and low-frequency limits of the spectrum. Figure 3.18 illustrates the positions on the vibrational-displacement axis where the turning points can be found.

The pattern of phase alternation shown in figure 3.17 is very similar to that observed in the spectrum from IR144 (see figure 3.4); the main differences involve a rapid relaxation of the energy of the excited state owing to dynamic solvation, which is not included in the simulation. The reader should refer to the work by Nagarajan[12] for a treatment of this issue.

3.3 Discussion

The results of this chapter show that a contour representation of the dynamic-absorption spectrum provides a powerful and easily used tool that permits a distinction on the basis of the vibrational phase between coherent wave-packet motions on a molecule's ground-state and excited-state potential energy surfaces even in the limit of small Stokes shifts. The experimental results from IR144 and the simulations show that a Fourier analysis of contour lines returns essentially the same modulation frequencies and relative magnitudes that a Fourier analysis of intensity transients provides. There may be a technical advantage in the analysis of contour lines because of their direct sensitivity to

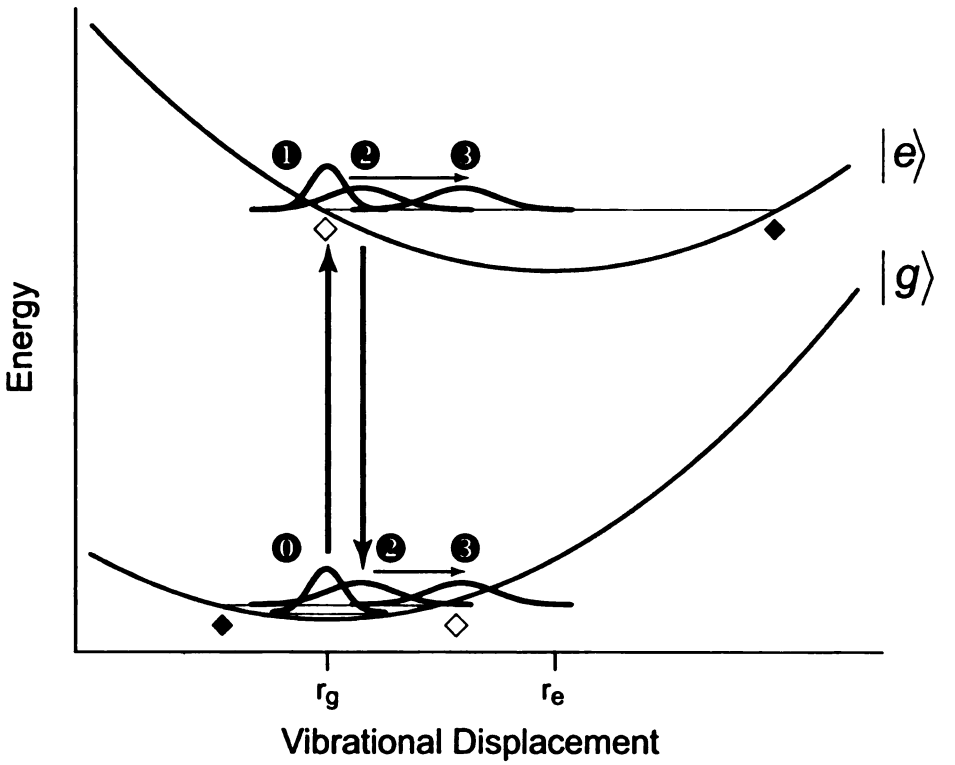

Figure 3.18. Excited-state and ground-state coherent wave-packet motion in the dynamic-absorption experiment. The excited-state ($|e\rangle$) and ground-state ($|g\rangle$) potential-energy surfaces are drawn as parabolas that are displaced with respect to a generalized multimode coordinate; r_g and r_e mark the equilibrium ground-state and excited-state geometries, respectively. Thick arrows represent the resonant pump-laser field; thin arrows show the direction that the wave packets evolve during the first passage on the two surfaces. The numbers indicate event times, starting with the ground-state probability density ($t = 0$), creation of the excited-state wave packet by the pump field ($t = 1$), creation of the ground-state wave packet by the pump field ($t = 2$), and evolution during the first vibration ($t = 3$). The turning-point regions, where a wave packet narrows and reverses its direction of motion, are marked on both surfaces with diamonds; white (unfilled) diamonds mark the turning points that contribute to the interference pattern in the dynamic-absorption spectrum.

modulation with respect to the probe wavelength, the main signature of coherent wave-packet motion. Further, the experimental results suggest that the contour lines are more sensitive to very low frequency modulations, which are inherently difficult to sense against a background of noise. The main value of the contour representation, however, lies in its direct projection of the phase relationships between pump–probe signals observed at different observation frequencies.

The antiphase character of the contour waveforms produced by the excited-state and ground-state wave packets in dynamic-absorption spectra arises naturally from stimulated emission and absorption, respectively, when the wave packets are resonant with probe photons.[5,22-24] As depicted in figure 3.18, the pump field prepares an excited-state wave packet at the Franck-Condon geometry. The excited-state wave packet is, in general, prepared on a sloping, displaced region of the excited-state surface owing to the change in electronic configuration that accompanies absorption of the pump photon. The ground-state wave packet is created by an interaction of the now moving excited-state wave packet with the pump field. The momentum of the parent excited-state wave packet is conserved in this process, so the excited-state and ground-state wave packets move in phase away from the Franck-Condon geometry. Because the excited-state surface is displaced, however, the recurrence time for the excited-state wave packet is somewhat delayed (for positive excited-state displacements) with respect to that of the ground-state wave packet.[5] In the limit of zero displacement and bound surfaces, the contour waveforms exhibited by the excited-state and ground-state wave packets would be exactly antiphase in character if the same modes are active on both surfaces. Both wave packets would describe the same equation of motion (structure as a function of time), but they act

oppositely on the transmitted probe intensity. Any phase shift between the resulting antiphase waveforms reports the displacement directly, and mode-specific displacements might be obtained from an analysis of the phases for individual modes, as preferably obtained by optimization of a model in the time domain.

3.3.1 Ground-State and Excited-State Wave-Packet Motion in IR144

The four regions of alternating phase that are observed in the contour representation of IR144's dynamic-absorption spectrum (see figure 3.4) define the spectral regions in which excited-state and ground-state wave-packet modulations can be observed. We chose to characterize in detail (see figures 3.5–3.10) the 808-nm and 864-nm regions because they lie in regions where the ground-state and excited-state wave packets, respectively, make a dominant contribution. The 808-nm region lies in the lower-energy of the two turning-point regions of the spectrum, so we can use contour lines and intensity transients in this part of the spectrum to obtain information on ground-state wave-packet motions. The 864-nm region lies in the long-wavelength-limit continuous run of contour lines that arise from motions of the excited-state wave packet.

The contour waveforms observed at 808-nm in the ground-state turning-point region and at 864-nm in the excited-state region (see figure 3.6) are almost exactly antiphase at early delays. This finding indicates that the IR144's low-frequency normal coordinates have only small displacements. The increasing phase difference between the two waveforms that is observed with increasing delay reports small differences in the excited-state and ground-state vibrational frequencies, but table 3.1 indicates that only two weak components out of eleven modes exhibit significant frequency shifts (and, surprisingly, the

excited state exhibits higher frequencies in these two modes). Given the lack of large frequency shifts and displacements along the low-frequency coordinates, it is likely that these modes gain some of their activity through anharmonic coupling to high-frequency modes that are not impulsively excited in these experiments. These high-frequency modes are likely to be those of totally symmetric character that obtain resonance Raman intensity[25] from the Albrecht *A*-term mechanism; the low-frequency modes also may obtain their intensities via the *B*-term mechanism owing to mixing of the Franck-Condon state with other electronic states in the energy neighborhood.

The 15-cm^{-1} feature observed much more prominently in the ground-state wave-packet motion is the most interesting in this regard. The relatively strong ground-state intensity shows that the excited-state wave packet is moving near the Franck-Condon region with some significant amplitude along the normal coordinate(s) associated with this feature.[26] The much weaker excited-state intensity suggests that the wave packet moves rather quickly, well within the period of the vibration of this coordinate, to a region of the excited-state potential-energy surface that is relatively flat with respect to the low-frequency coordinate(s). This motion is associated with several vibrations along the higher-frequency coordinates.

3.3.2 Nature of IR144's Lowest-Frequency Vibrations

Lacking a systematic isotopic-substitution study, it is not possible at this point to provide definitive assignments for the low-frequency modes that are active in the vibrational coherence on the ground and excited states of IR144. Nevertheless, through the use of ground-state electronic structure calculations and normal-mode calculations

from the optimized geometries, we can suggest probable assignments in terms of classes of motion with respect to IR144's conjugated-polyene backbone.

We employed Gaussian 98[27] to perform a series of calculations at various levels of theory. The structures that were electronically and structurally peripheral in IR144 to the conjugated polyene, the piperazinyl ring and the propylsulfonyl tails, were truncated to dimethylamine and methyl groups, respectively. These simplifications are reasonable because the resonant electronic transition in the dynamic-absorption experiments is a $\pi \rightarrow \pi^*$ transition. The UFF molecular-mechanics force field was employed to obtain an approximate structure; the optimized structure was then used, in series, to obtain optimized structures in the ground state with the AM1 semi-empirical theory and then the B3LYP hybrid density-functional theory with the 6-31G(d) basis set. Good minima were located on the ground-state surface in each case. From each optimized structure, the normal modes and frequencies were obtained with the same theory used to optimize the geometry.

The most significant result of the AM1 and B3LYP calculations is that IR144 should exhibit three global normal modes with estimated frequencies in the 10–15-cm^{-1} regime. These modes should exhibit resonance Raman intensity because they involve distortions of the conjugated polyene. The mode with the lowest frequency in this range can be described as a hindered torsion; the central five-membered ring (see figure 3.1) resists large displacements along this coordinate, which would contribute in the ring's absence to isomerization of the central carbon-carbon double bond. The other two modes, arising from in-plane and out-of-plane deformations, are nearly degenerate. We suggest that the prominent 15-cm^{-1} feature, observed especially in the ground-state vibrational coherence,

can be assigned to the superimposed line shapes arising from the three global modes. The intensity difference noted for ground-state and excited-state vibrational coherence in the 15-cm^{-1} mode might be interpreted, then, as an indication that a significant distortion of the conjugated polyene along at least one of the global coordinates occurs within one vibrational period. This geometry change will contribute to the intramolecular (non-solvation) portion of the decay of the ground--excited-state energy-gap time-correlation function $M(t)$, which is detected in stimulated photon-echo and dynamic fluorescence Stokes shift experiments.[28-30]

3.4 References

(1) Lakowicz, J. R. *Principles of Fluorescence Spectroscopy*; Second ed.; Kluwer Academic/Plenum Publishers: New York, 1999.

(2) Edelstein, D. C.; Romney, R. B.; Scheuermann, M. *Rev. Sci. Instrum.* **1991**, *62*, 579–583.

(3) Diffey, W. M.; Beck, W. F. *Rev. Sci. Instrum.* **1997**, *68*, 3296–3300.

(4) Cantor, C. R.; Schimmel, P. R. *Biophysical Chemistry. Part II: Techniques for the Study of Biological Structure and Function*; W. H. Freeman and Company: San Francisco, 1980.

(5) Pollard, W. T.; Mathies, R. A. *Annu. Rev. Phys. Chem.* **1992**, *43*, 497–523.

(6) Press, W. H.; Flannery, B. P.; Teukolsky, S. A.; Vetterline, W. T. *Numerical Recipes: the Art of Scientific Computing*; Cambridge University Press: Cambridge, 1986.

(7) McMorrow, D.; Lotshaw, W. T. *Chem. Phys. Lett.* **1990**, *174*, 85–94.

(8) McHale, J. L. *Molecular Spectroscopy*; Prentice Hall: Upper Saddle River, New Jersey, 1999.

(9) Chachisvilis, M.; Fidder, H.; Pullerits, T.; Sundstrom, V. *J. Raman Spect.* **1995**, *26*, 513–522.

(10) Chachisvilis, M.; Pullerits, T.; Jones, M. R.; Hunter, C. N.; Sundstrom, V. *Chem. Phys. Lett.* **1994**, *224*, 345–351.

(11) Chachisvilis, M.; Sundstrom, V. *Chem. Phys. Lett.* **1996**, *261*, 165–174.

(12) Nagarajan, V. *Chem. Phys. Lett.* **2000**, *317*, 203–210.

(13) Vos, M. H.; Rappaport, F.; Lambry, J.-C.; Breton, J.; Martin, J.-L. *Nature* **1993**, *363*, 320–325.

(14) Jonas, D. M.; Bradforth, S. E.; Passino, S. A.; Fleming, G. R. *J. Phys. Chem.* **1995**, *99*, 2594–2608.

(15) Wang, Q.; Schoenlein, R. W.; Peteanu, L. A.; Mathies, R. A.; Shank, C. V. *Science* **1994**, *266*, 422–424.

(16) Zhu, L.; Sage, J. T.; Champion, P. M. *Science* **1994**, *266*, 629–632.

(17) Bardeen, C. J.; Wang, Q.; Shank, C. V. *J. Phys. Chem. A* **1998**, *102*, 2759–2766.

(18) Rosca, F.; Kumar, A. T. N.; Ye, X.; Sjodin, T.; Demidov, A.; Champion, P. M. *J. Phys. Chem. A* **2000**, *104*, 4280–4290.

(19) Diffey, W. M. In *Department of Chemistry*; Vanderbilt University: Nashville, Tennessee, 2002.

(20) Scherer, N. F.; Ziegler, L. D.; Fleming, G. R. *J. Chem. Phys.* **1992**, *96*, 5544–5547.

(21) Scherer, N. F.; Jonas, D. M.; Fleming, G. R. *J. Chem. Phys.* **1993**, *99*, 153–168.

(22) Pollard, W. T.; Dexheimer, S. L.; Wang, Q.; Peteanu, L. A.; Shank, C. V.; Mathies, R. A. *J. Phys. Chem.* **1992**, *96*, 6147–6158.

(23) Pollard, W. T.; Fragnito, H. L.; Bigot, J.-Y.; Shank, C. V.; Mathies, R. A. *Chem. Phys. Lett.* **1990**, *168*, 239–245.

(24) Pollard, W. T.; Lee, S.-Y.; Mathies, R. A. *J. Chem. Phys.* **1990**, *92*, 4012–4029.

(25) Tang, J.; Albrecht, A. C. In *Raman Spectroscopy: Theory and Practice*; Szymanski, H. A., Ed.; Plenum: New York, 1970; Vol. 2, p 33–68.

(26) Myers, A. B.; Mathies, R. A. In *Biological Applications of Raman Spectroscopy*; Spiro, T. G., Ed.; Wiley-Interscience: New York, 1987; Vol. 2, *Resonance Raman Spectra of Polyenes and Aromatics*, p 1–58.

(27) Frisch, M. J.; Trucks, G. W.; Schlegel, H. B.; Scuseria, G. E.; Robb, M. A.; Cheeseman, J. R.; Zakrzewski, V. G; J. A. Montgomery, J.; Stratmann, R. E.; Burant, J. C.; Dapprich, S.; Millam, J. M.; Daniels, A. D.; Kudin, K. N.; Strain, M. C.; Farkas, O.; Tomasi, J.; Barone, V.; Cossi, M.; Cammi, R.; Mennucci, B.; Pomelli, C.; Adamo, C.; Clifford, S.; Ochterski, J.; Petersson, G. A.; Ayala, P. Y.; Cui, Q.; Morokuma, K.; Salvador, P.; Dannenberg, J. J.; Malick, D. K.; Rabuck, A. D.; Raghavachari, K.; Foresman, J. B.; Cioslowski, J.; Ortiz, J. V.; Baboul, A. G; Stefanov, B. B.; Liu, G; Liashenko, A.; Piskorz, P.; Komaromi, I.; Gomperts, R.; Martin, R. L.; Fox, D. J.; Keith, T.; Al-Laham, M. A.; Peng, C. Y.; Nanayakkara, A.; Challacombe, M.; Gill, P. M. W.; Johnson, B.; Chen, W.; Wong, M. W.; Andres, J. L.; Gonzalez, C.; Head-Gordon, M.; Replogle, E. S.; Pople, J. A. *Gaussian 98, Revision A.11.1*; Gaussian, Inc.: Pittsburgh, Pennsylvania, 2001.

(28) Joo, T.; Jia, Y.; Yu, J.-Y.; Lang, M. J.; Fleming, G. R. *J. Chem. Phys.* **1996**, *104*, 6089–6108.

(29) Passino, S. A.; Nagasawa, Y.; Joo, T.; Fleming, G. R. *J. Phys. Chem. A* **1997**, *101*, 725–731.

(30) Nagasawa, Y.; Passino, S. A.; Joo, T.; Fleming, G. R. *J. Chem. Phys.* **1997**, *106*, 4840–4852.

CHAPTER 4

DYNAMIC-ABSORPTION CONTOURS FROM DTTCI: RAMAN ACTIVITY FROM ISOMERIZATION, GROUND–EXCITED STATE FREQUENCY SHIFTS AND DEPOLARIZATION

4.0 Introduction

As shown in chapter three, a clear distinction between the ground-state and excited-state vibrational coherence cannot be made solely on the basis of probe wavelength due to the overlap of the ground-state depletion and stimulated-emission regions near the 0–0 vibronic transition. In the last chapter, we developed an approach that uses the phase of the vibrations to distinguish between the two signals and demonstrated that a contour representation of the dynamic-absorption surface permits one to obtain phase information by inspection.[1]

In this chapter, we study the carbocyanine dye, DTTCI, which lacks the central ring structure of IR144 (as shown in figure 4.1) and is able to isomerize. As discussed in chapter one, the *trans–cis* isomerization of DTTCI occurs on the nanosecond time scale from a torsionally relaxed excited state which relaxes to either the *trans* or *cis* form.[2,3] Given the ability to isomerize, we would expect to see evidence in the dynamic-absorption spectrum from DTTCI. In this chapter, we show that DTTCI exhibits a four-phase dynamic-absorption spectrum similar to IR144. Additional vibrational modes are observed in the excited-state vibrational coherence which are not observed in the ground-state vibrational coherence. The novel use of polarization shows that none of the components in the ground-state and excited-state vibrational coherence obtain their activity from vibrational displacement, so activity is obtained from either the Albrecht

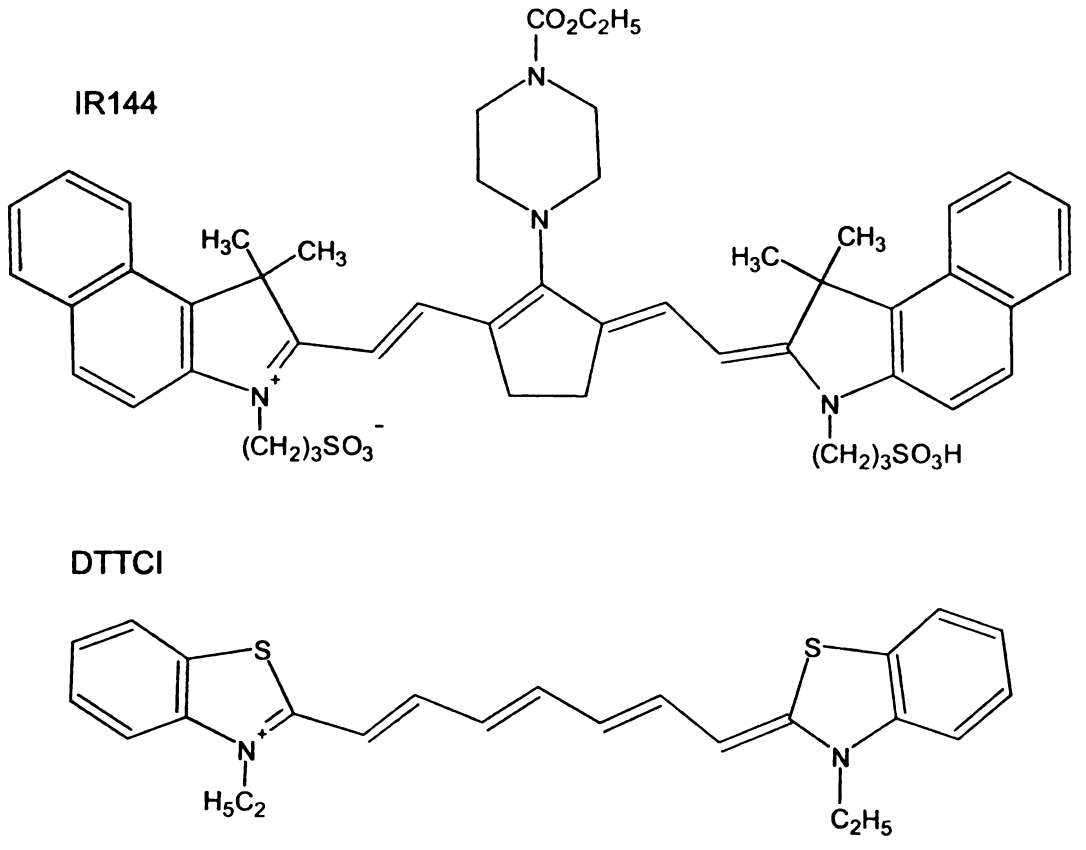

Figure 4.1. All-*trans* configurations of IR144 (anhydro-11-(4-ethoxycarbonyl-1-piperazinyl)-10,12-ethylene-3,3,3′,3′-tetramethyl-1,1′-di-(3-sulfopropyl)-4,5,4′,5′-dibenzoindotricarbocyanine hydroxide) and DTTCI (3,3′-diethylthiatricarbocyanine iodide).

B-term mechanism or from anharmonic coupling to the *A*-term active modes that are displaced in the Franck-Condon region. Lastly, we observe two time regions of vibrational dephasing that strongly suggest involvement of intermolecular modes with solvent.

4.1 Experimental

4.1.1 Sample Preparation

DTTCI was obtained from Exciton and used as received. Samples were dissolved in methanol (Spectrum, spectrophotometric grade) to obtain an absorbance of 0.4–0.6 at 760 nm for a 1-mm path length; the DTTCI solution was passed through a 0.22-μm filter prior to use.

4.1.2 Continuous-Wave Absorption and Fluorescence Spectroscopy

Fluorescence spectra were obtained at 23° C with a home-built visible/near-IR spectrofluorimeter and a liquid-nitrogen cooled CCD detector, which have been described previously in chapter three.[1] The excitation and emission band passes were 4 nm and 3.33 nm, respectively. The fluorescence intensities were corrected using a calibration curve obtained from a standard lamp and were multiplied by the square of the wavelength in order to compensate for the fixed spectral band pass of the spectrometer.[4,5] Absorption spectra were obtained with 2-nm spectral band pass at 22° C with a Hitachi U-2000 spectrometer.[1]

4.1.3 Femtosecond Spectroscopy

Dynamic-absorption spectroscopy was performed with two femtosecond pump–probe spectrometers built around self-mode-locked titanium–sapphire oscillators. The short-pulse apparatus was discussed previously in chapter two. The long-pulse, narrow-spectrum apparatus was discussed previously in chapter three. For the experiments presented in this chapter, the Murnane-Kapteyn oscillator was adjusted to produce 12-fs pulses ($sech^2$) with a band width of 820-cm^{-1} (fwhm) centered at 800 nm; the Mira 9000 oscillator was adjusted to produce 52-fs pulses ($sech^2$) with a band width of 250-cm^{-1} (fwhm) centered at 750 nm.

Samples were held at room temperature (22 ° C) in a fused-silica flow cuvette with 1-mm path length. The flow rate was 6 mL/min. The absorption spectrum of the sample was monitored for changes arising from photochemistry or permanent photobleaching.

4.2 Results

4.2.1 Continuous-Wave Spectroscopy

Figure 4.2 shows the absorption and fluorescence spectra of DTTCI in methanol at room temperature. The spectra are plotted with respect to wavenumber as $A(\nu)/\nu$ and $F(\nu)/\nu^3$, respectively, with normalization to unit area. The integrals of these quantities report the dipole strength, the square of the transition-dipole moment.[4,6] The fluorescence and absorption spectra exhibit a partially resolved vibronic progression. The spectra can be described by the sum of two lognormal lineshapes[5,7] corresponding to the 0–0 and 0–1 vibronic transitions spaced by 890 cm^{-1} and 1495 cm^{-1}, respectively. This ground-to-excited state change in mode frequency suggests a significant change in structure.[3]

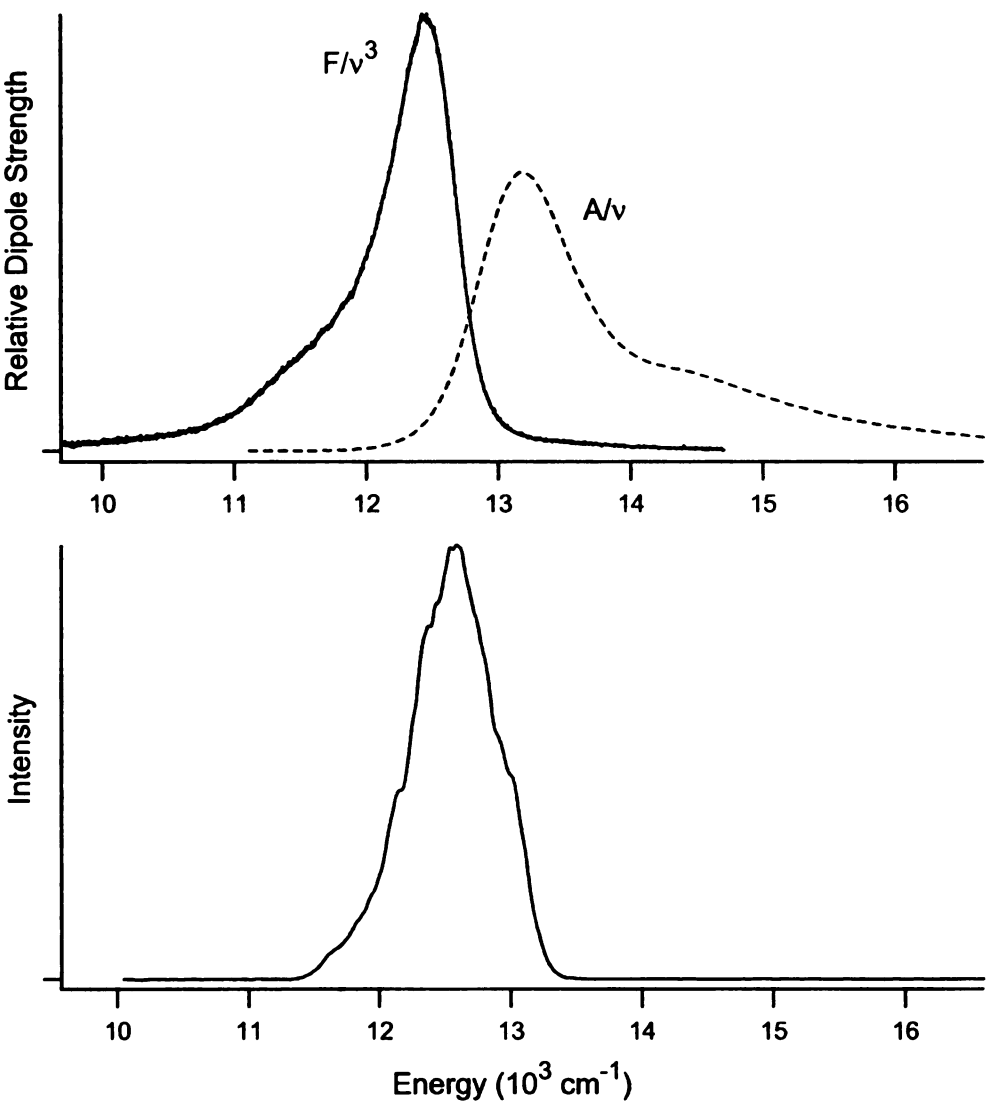

Figure 4.2. *Top panel:* Continuous-wave absorption (dashed curve) and fluorescence (solid curve) spectra from DTTCI in methanol. The spectra are plotted as relative dipole strengths, A/ν and F/ν^3, respectively, and are normalized to unit area. The excitation source for the fluorescence spectrum was tuned to the 0–0 transition energy, where the absorption and fluorescence dipole-strength spectra cross. *Bottom panel*: Intensity spectrum from the Murnane-Kapteyn oscillator used in the short-pulse dynamic-absorption experiments, plotted on the same energy scale.

The spectrum from the Murnane-Kapteyn oscillator (11 480–13 343 cm^{-1}, with peak intensity at 12 580 cm^{-1}) overlaps with most of the fluorescence spectrum, but only the red tail of the absorption spectrum. As used in the short-pulse dynamic-absorption experiments, the probe spectrum overlaps with much of the stimulated-emission spectrum but only a small portion of the ground-state depletion spectrum.

4.2.2 Short-Pulse Dynamic-Absorption Experiments

The dynamic-absorption spectrum from DTTCI in methanol was acquired as a set of single-wavelength transients spanning most of the 110-nm range of transmitted probe wavelengths from the Murnane-Kapteyn oscillator. The spacing of the probe wavelengths matched the spectral band pass of the monochromator (4 nm). As discussed previously, the transients describe an intensity-time-wavelength surface that can be usefully visualized in a contour representation.

The main panel of figure 4.3 shows a contour representation of the dynamic-absorption surface of DTTCI. By using the methods discussed previously[1], the contour plot was obtained from the data set, using default settings in the program Igor Pro (Wavemetrics). The contour lines exhibit wavelength oscillations over the entire 4000-fs delay range. As observed previously in the spectrum from IR144, the wavelength oscillations are grouped into sets of contour lines with the same phase. The first set begins at 870 nm and continues to 830 nm. The next set is opposite in phase and ranges from 830 nm to 780 nm. The last set begins at 790 nm and continues to 760 nm.

As discussed previously[1] in chapter three, ground- and excited-state wave-packet motion cause anti-phase spectral oscillations. The four regions of phase observed pertain

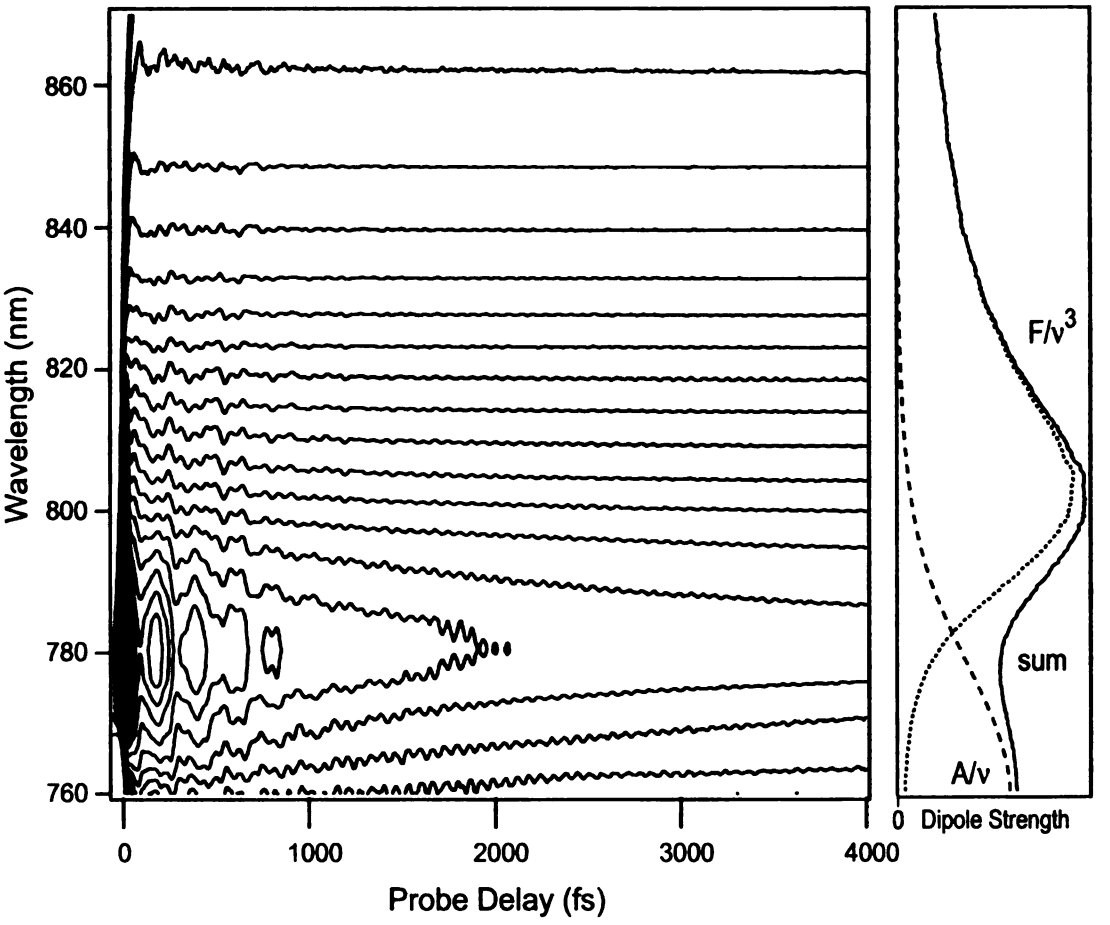

Figure 4.3. Contour representation of the dynamic-absorption spectrum from DTTCI in methanol. The right-hand panel shows the absorption (dashed curve) and the fluorescence (dotted curve) dipole-strength spectra and their sum (solid curve) plotted on the same wavelength scale.

to the pure ground and excited states and the ground-state and excited-state turning points. We only observe three regions of phase are from DTTCI. The spectrum of the laser used in these experiments overlaps with a significant portion of the fluorescence spectrum from DTTCI. We are not able to probe a region of the spectrum from DTTCI where there is not overlap with the fluorescence, so we are unable to observe the fourth phase region pertaining to pure ground-state.

Figure 4.4 shows an expanded view of the oscillatory portion of three contour lines selected from each of the phase regions shown in figure 4.3. The oscillatory portion of each contour line was obtained by subtracting a fitted double-exponential baseline function. The contour line centered at 770 nm was chosen from the region of contour lines that corresponds to the excited-state turning point region. The 790-nm contour line was chosen from the region of contour lines that corresponds to the ground-state turning point region. The contour line centered at 840 nm was chosen from the region of contour lines that corresponds to the excited-state region. Figure 4.4 shows that the three contour lines exhibit similar oscillatory features, but with alternating phase.

Two transients from the data set used to build the dynamic-absorption surface are shown in figure 4.5. A step-function increase in the transmitted-probe signal associated with the net population transfer from the ground state to the excited state is observed following the zero of time. A rapid decay in the 790-nm transient and a comparably rapid rise in the 840-nm transient follows; a red-to-blue spectral evolution owing to dynamic solvation occurs on less than 1 ps time scale. Intensity oscillations arising from coherent wave-packet motions are observed over the 100–6000 fs probe-delay range.

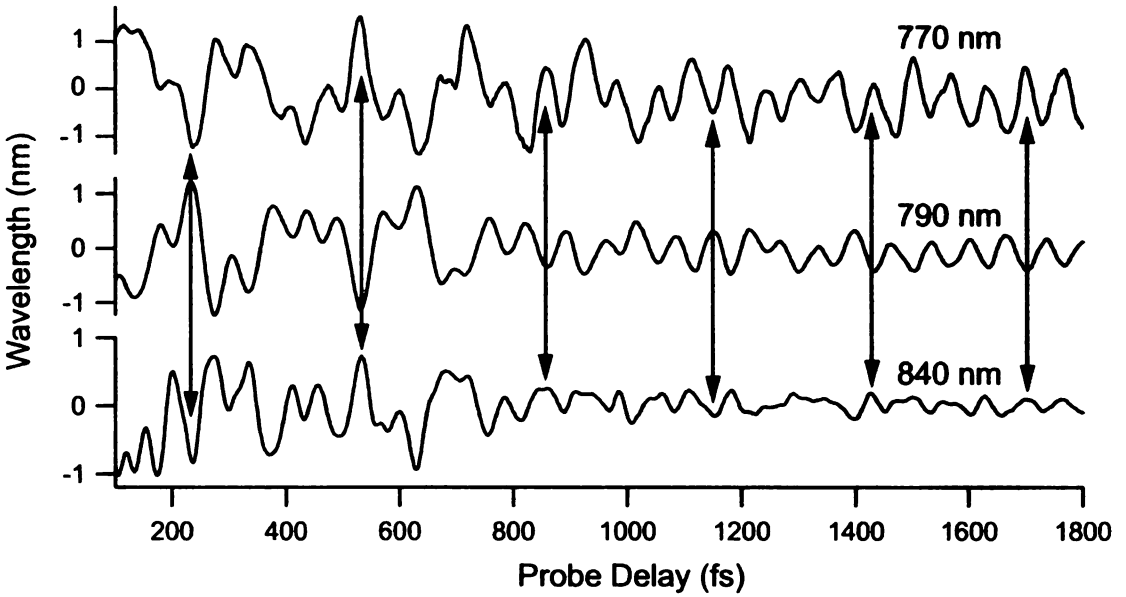

Figure 4.4. Delay-expanded view of the oscillatory signals obtained from contour lines centered at 770 nm, 790 nm, and 840 nm in the dynamic-absorption spectrum from DTTCI in methanol (see figure 4.3) showing the two inversions of phase that occur as the detected probe band width is scanned. Arrows mark alternately phased extrema at several delay points.

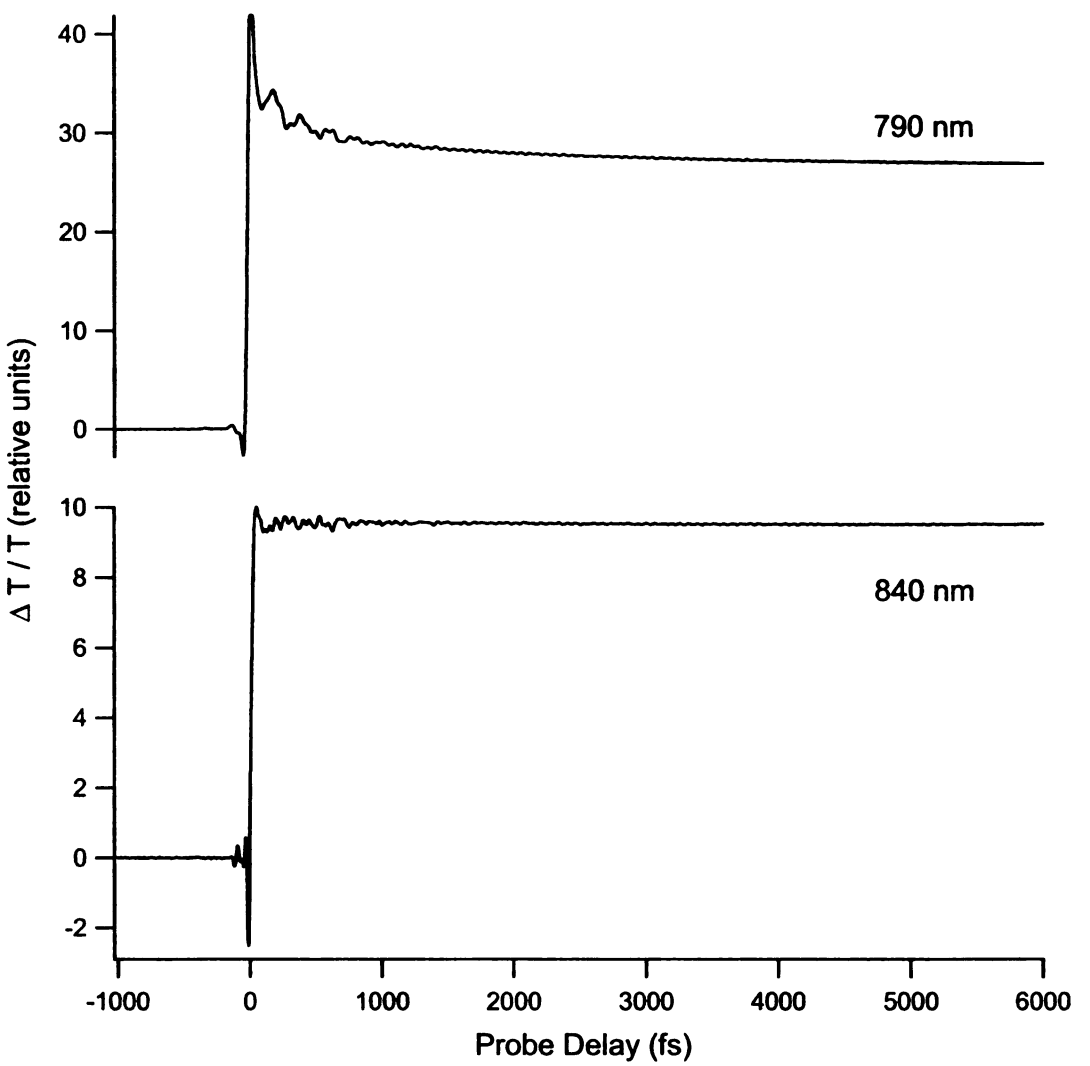

Figure 4.5. Dynamic-absorption transients from DTTCI in methanol, with the transmitted probe light detected at 790 nm and 840 nm.

4.2.3 Fourier-Magnitude Spectrum Estimation

The next four figures present a Fourier analysis of the oscillatory components observed in dynamic-absorption transients and contour lines at the 790- and 840-nm probe wavelengths, which correspond to the ground-state turning point and excited-state regions, respectively. The oscillatory portions from each signal were obtained by subtracting a fitted double-exponential baseline function. The oscillatory segment over the 150–4000 fs delay range was multiplied by a Hanning window function and zero-padded to suppress satellite ripples and enhance point density in the Fourier-magnitude spectra.[1]

Figure 4.6 shows the oscillatory signals observed from an intensity transient and a contour line at 790 nm. The Fourier-magnitude spectra obtained from the contour and the intensity transient are shown in figure 4.7. Nine frequency components are observed in both the contour and the intensity transient with strong components at 512 cm^{-1}, 163 cm^{-1} and 12 cm^{-1}. The oscillatory signals observed at 840 nm are shown in figure 4.8. Figure 4.9 shows the Fourier-magnitude spectra obtained from the excited-state oscillatory signals. Eighteen frequency components are observed in both the intensity transient and the contour line with strong components at 512 cm^{-1}, 262 cm^{-1}, 163 cm^{-1} and 12 cm^{-1}. New frequencies are observed in the 700–1000 cm^{-1} region of the excited-state spectra, which are not observed in the ground state. In addition to these new frequencies, the intensity of 262-cm^{-1} peak is notably stronger in the excited state than in the ground state.

To obtain reliable estimates for intensities and damping times, the experimental Fourier-magnitude spectra obtained from the contour lines at 790 and 840 nm were modeled in the time domain using a sum of damped cosines. This procedure has been

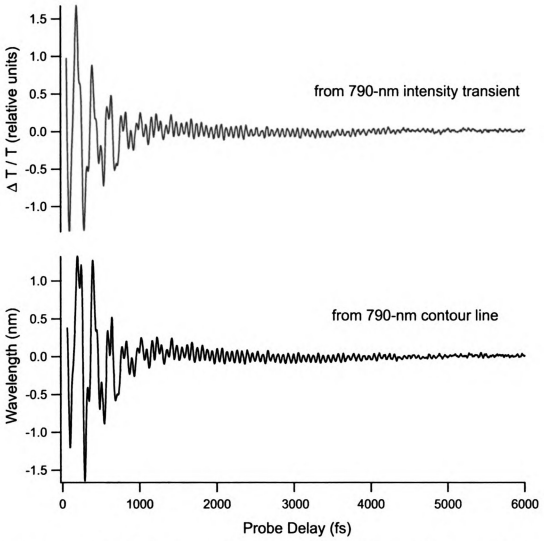

Figure 4.6. Oscillatory components observed in the dynamic-absorption spectrum from DTTCI in methanol: *Top Panel:* from the intensity transient at 790 nm (see figure 4.5); *Bottom Panel:* from the contour line centered at 790 nm (see figure 4.4).

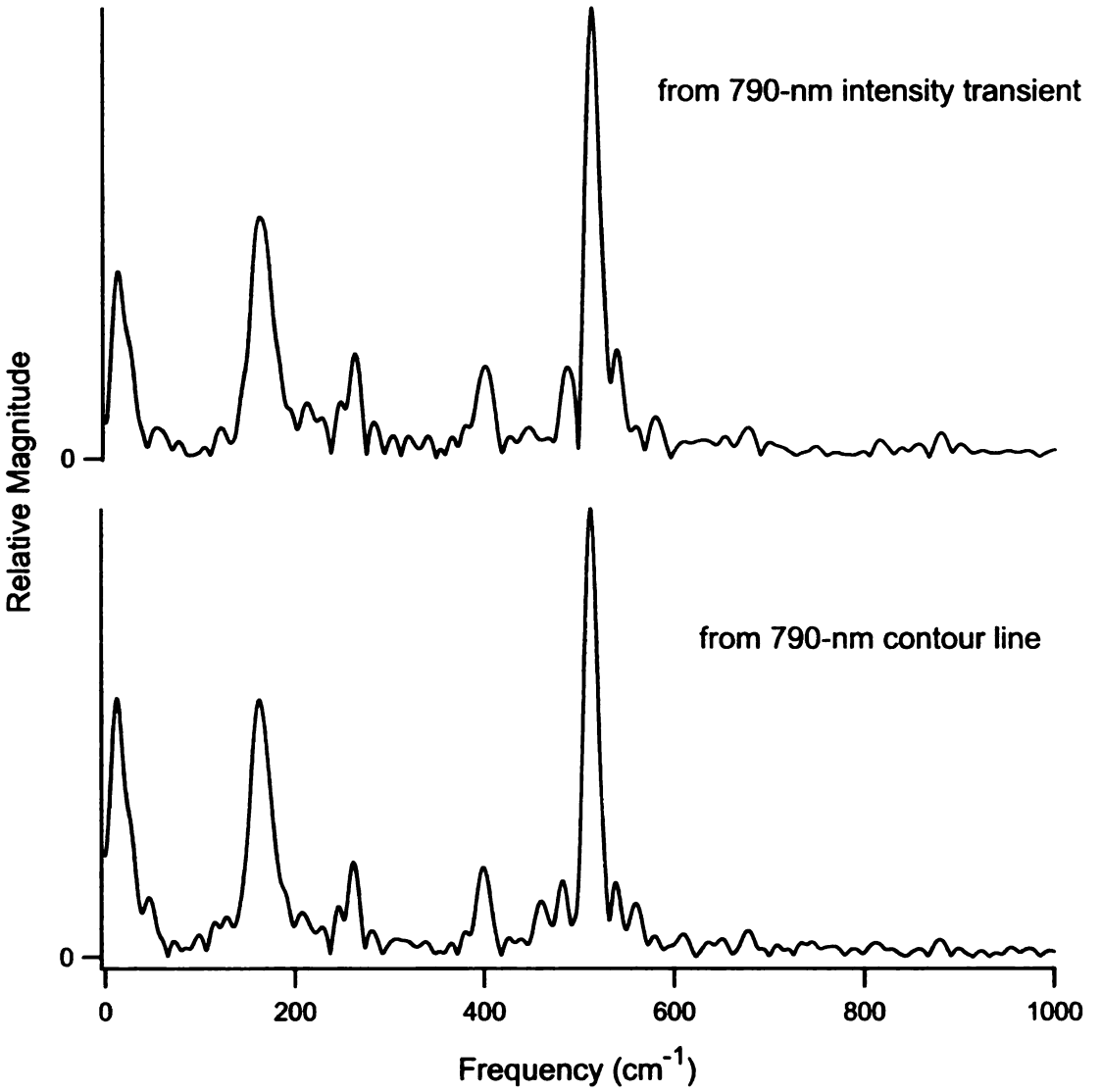

Figure 4.7. Fourier-magnitude spectra from the oscillatory components at 790 nm (see figure 4.6) from the intensity transient (top) and from the contour line (bottom).

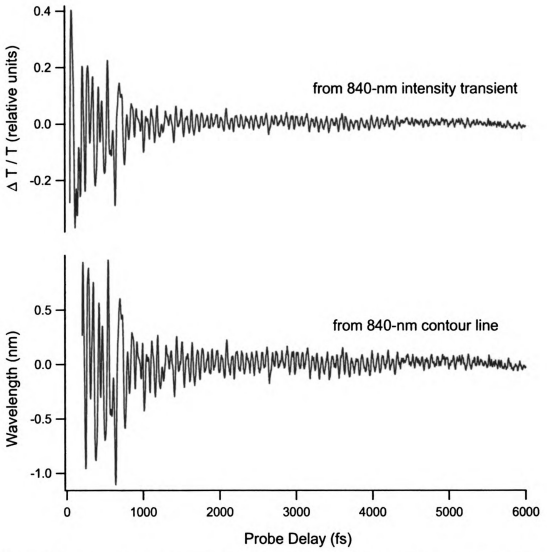

Figure 4.8. Oscillatory components observed in the dynamic-absorption spectrum from DTTCI in methanol: *Top Panel:* from the intensity transient at 840 nm (see figure 4.5); *Bottom Panel:* from the contour line centered at 840 nm (see figure 4.4).

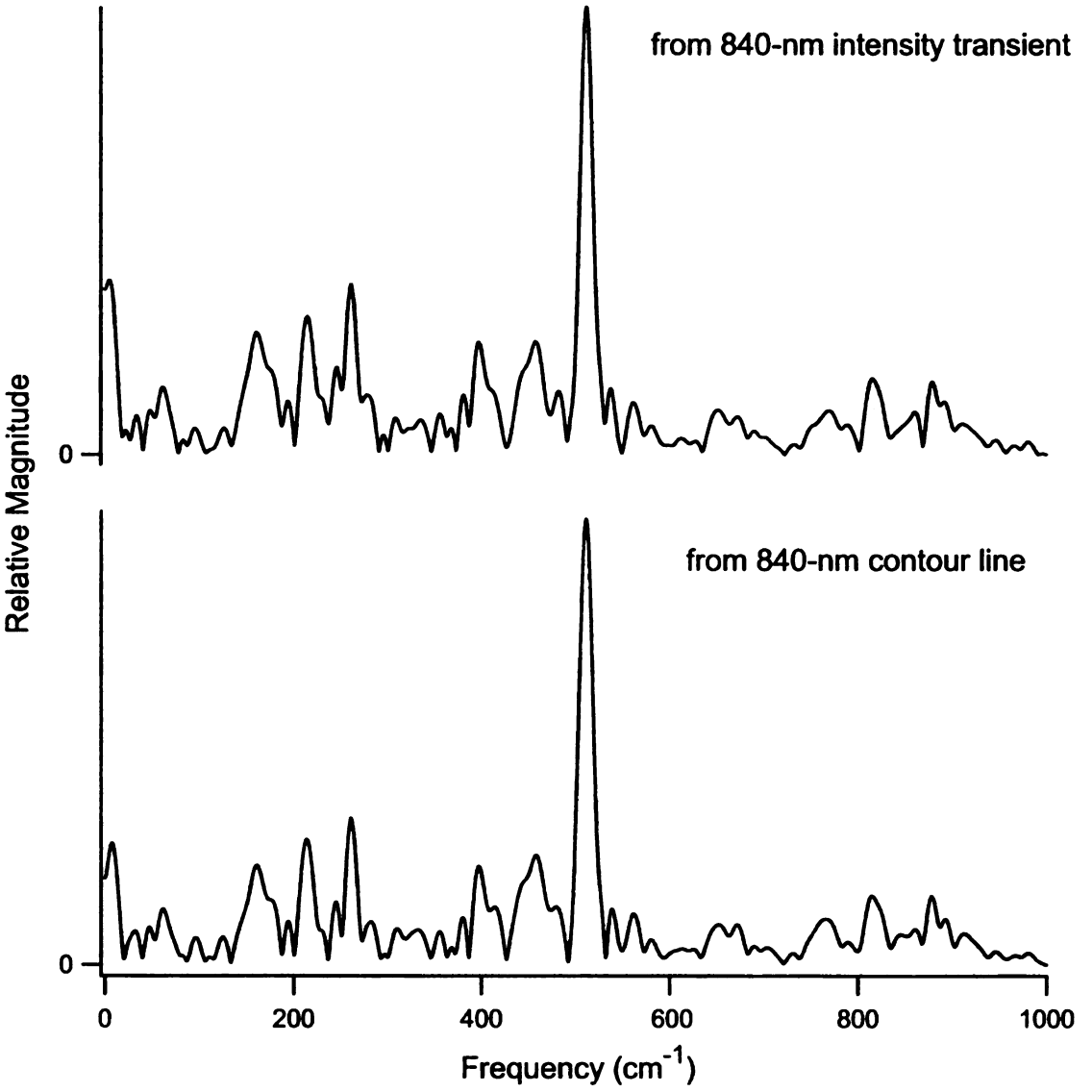

Figure 4.9. Fourier-magnitude spectra from the oscillatory components at 840 nm (see figure 4.8) from the intensity transient (top) and from the contour line (bottom).

described previously.[1] The optimized parameters are listed in table 4.1. The intensities listed in the table were compensated for the finite width of the instrument-response function by deconvolution in the frequency domain. The raw optimized amplitudes were scaled by the reciprocal of the Fourier magnitude obtained from the pump–probe autocorrelation signal.[8] The components listed are those that were reproduced in several experimental trials under the same conditions.

4.2.4 Long-Pulse Dynamic-Absorption Experiments

To probe the ground-state depletion portion of the dynamic-absorption spectrum farther to the blue than was possible in the short-pulse experiments, we performed a set of experiments with pulses of 52-fs ($sech^2$) duration and a spectral width of 11.5 nm from the Mira9000 oscillator. Figure 4.10 shows the dynamic-absorption transient, oscillatory component and Fourier-magnitude spectrum obtained with the pump spectrum centered at 750 nm and transmitted-probe detected at 743 nm. The Fourier-magnitude spectrum, obtained from a 3500-fs window of the oscillatory portion, reproduces the relative magnitudes and frequencies of the 12 cm^{-1} and 163 cm^{-1} modes from the ground-state data obtained from the short-pulse experiment. High frequency components are lost due to the longer pulse width.

4.2.5 Polarized Dynamic-Absorption Experiments

An additional set of experiments was performed to elucidate the mechanism through which the vibrational modes observed in the vibrational coherence obtain activity. Intensity transients were acquired in the ground-state and excited-state regions with

Table 4.1. Frequencies, normalized intensities, and damping constants for modulation components observed in contour lines at 790 nm and 840 nm from the dynamic-absorption spectrum of DTTCI.

Frequency	790-nm contour		840-nm contour	
(cm^{-1})	Intensity[a]	γ (fs)	Intensity[a]	γ (fs)
12	0.36	1000	0.28	1000
53	-	-	0.06	1500
163	0.96	600	0.53	600
192	-	-	0.10	1000
205	0.09	1000	-	-
213	-	-	0.19	1000
248	-	-	0.10	1300
262	0.10	1300	0.19	1300
280	-	-	0.12	1000
401	0.27	800	0.27	800
460	-	-	0.22	1000
479	0.17	1000	0.14	1000
512	1	1000	1	1000
541	0.14	1300	0.14	1300
564	0.15	1000	0.24	1000
775	-	-	0.31	1000
816	-	-	0.45	1000
861	-	-	0.24	1000
882	-	-	0.59	1000

[a] Relative to the intensity of the 512-cm^{-1} mode after deconvolution in the frequency domain.

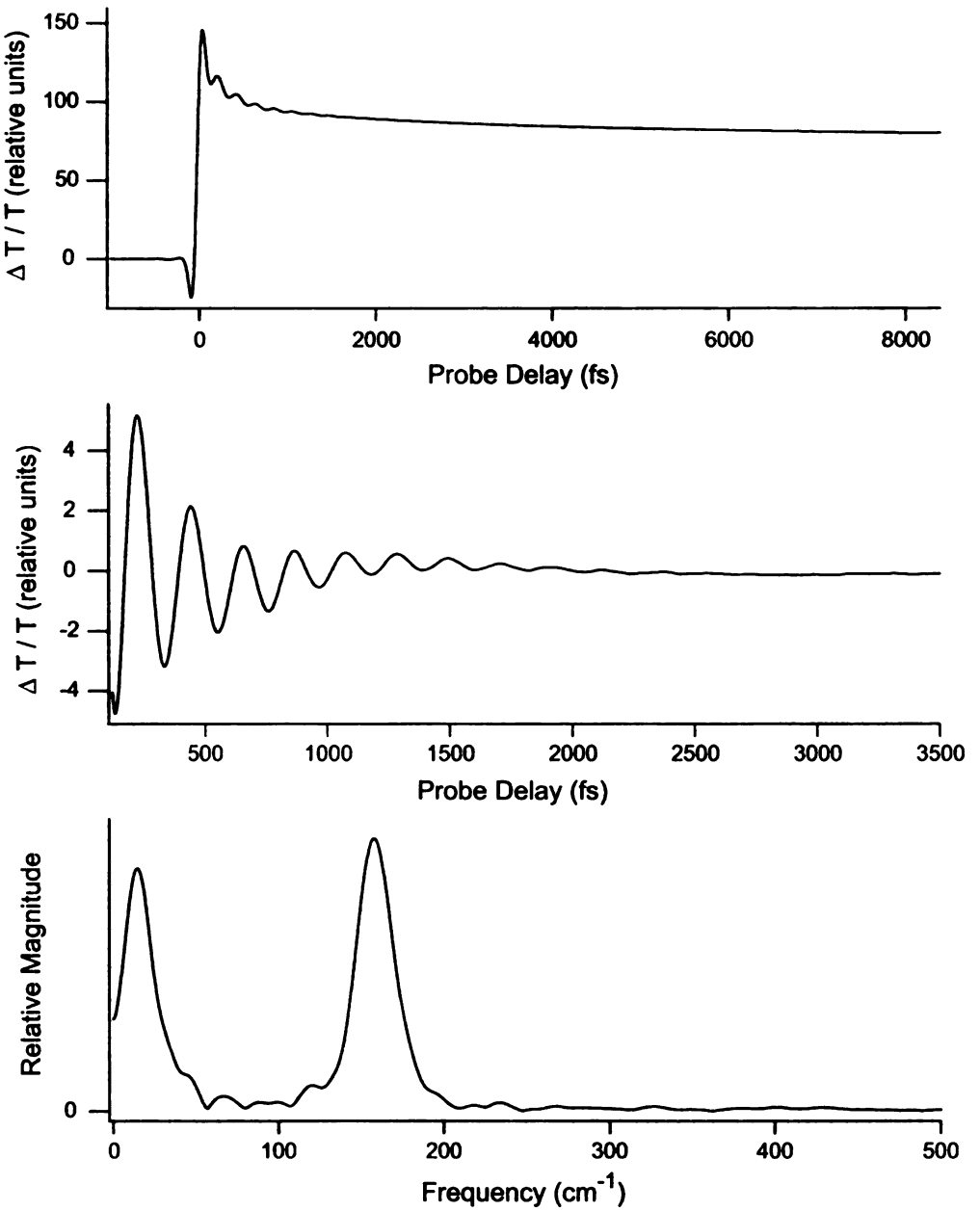

Figure 4.10. Narrow-spectrum, long-pulse (52-fs) dynamic-absorption transient (top), oscillatory component (middle), and Fourier-magnitude spectrum (bottom) obtained from DTTCI in methanol. The pump spectrum and transmitted-probe band pass were centered at 750 nm and 743 nm, respectively. The delay window used for the Fourier transform was 3500-fs wide.

polarization analysis of the transmitted-probe beam set relative to the plane of polarization of the pump beam. Figure 4.11 shows the oscillatory signals obtained at 790 nm. Figure 4.12 shows the Fourier-magnitude spectra obtained from the ground-state oscillatory signals. The intensities and damping times for most frequencies are similar for both polarizations. Figure 4.13 shows the oscillatory signals obtained at 840 nm. The Fourier-magnitude spectra obtained from the excited-state oscillatory signals are shown in figure 4.14. For most frequencies, the intensities and damping times are similar for both polarizations observed from the ground and excited states.

4.3 Discussion

4.3.1 Ground-State and Excited-State Wave-Packet Motion in DTTCI

The three regions of alternating phase that are observed in the contour representation of the dynamic-absorption spectrum of DTTCI (see figure 4.3) define the spectral regions in which excited-state and ground-state wave-packet modulations can be observed. We chose to characterize the 790- and 840-nm regions (see figures 4.6–4.9) because they lie in regions where the ground-state and excited-state wave packets, respectively, make a dominant contribution. The 790-nm region lies in the lower energy of the two turning-point regions of the spectrum, so we can use contour lines and intensity transients in this region to obtain information on ground-state wave-packet motions. The 840-nm region lies in the set of contour lines that result from the motions of the excited-state wave packet.

Comparison of the ground-state and excited-state vibrational frequencies indicates that the excited-state has new vibrational components, the most significant are those

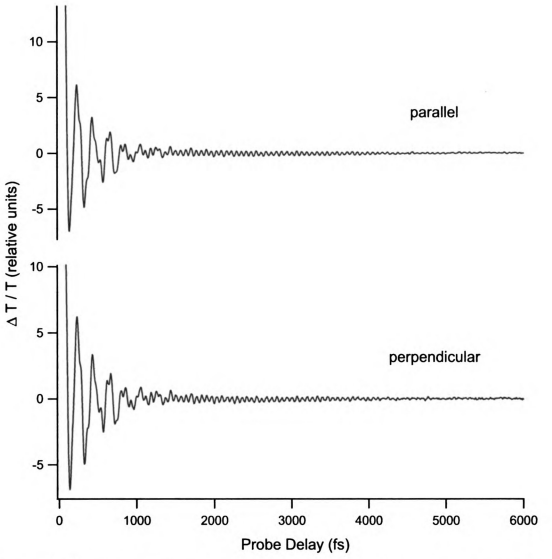

Figure 4.11. Oscillatory components observed in the dynamic-absorption spectrum from DTTCI in methanol at 790 nm; *Top panel:* with polarization analysis of the transmitted probe beam parallel respect to the pump beam's plane of polarization; *Bottom panel:* with polarization analysis of the transmitted probe beam perpendicular with respect to the pump beam's plane of polarization.

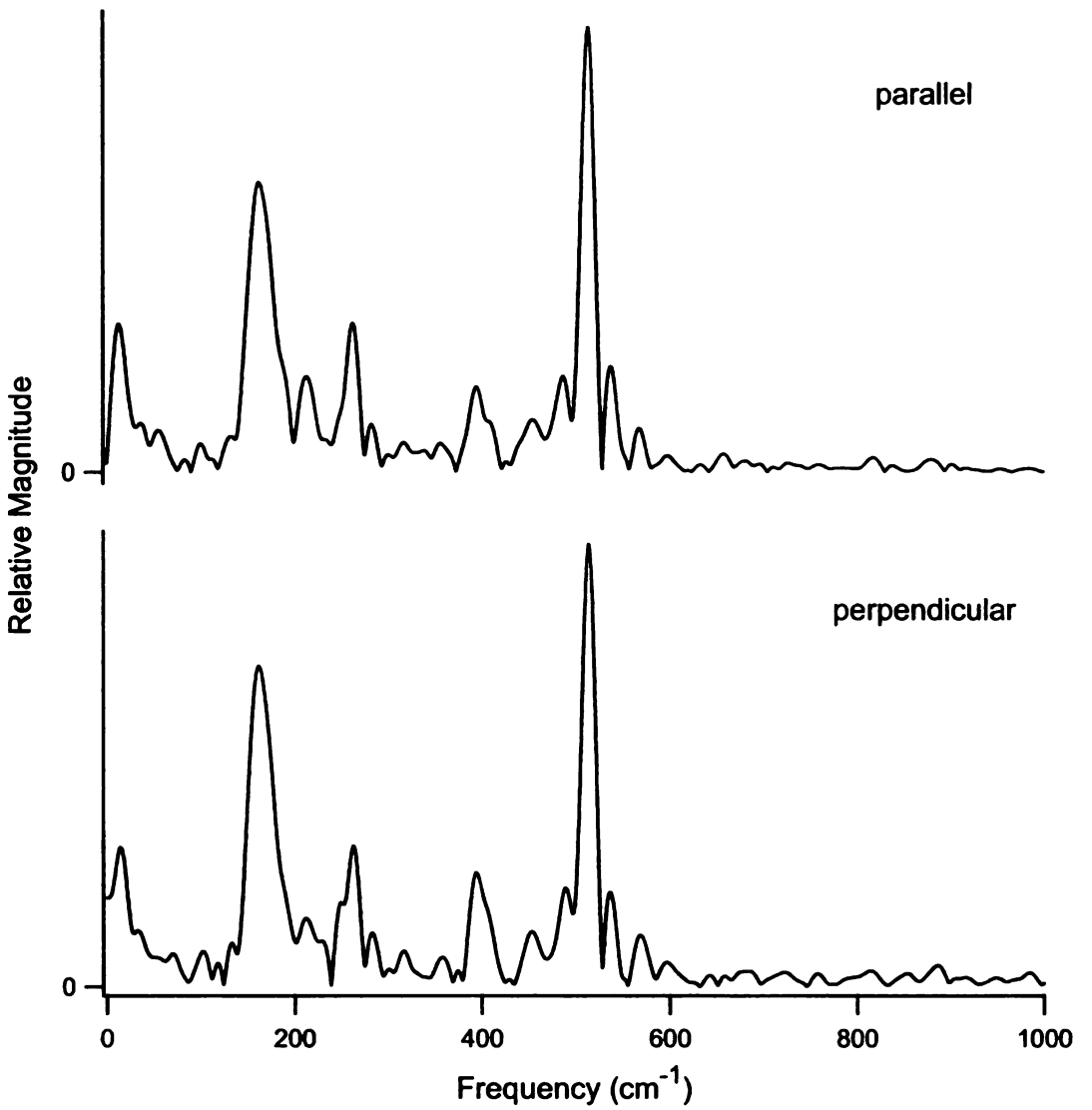

Figure 4.12. Fourier-magnitude spectra obtained from the polarized oscillatory components at 790 nm (see figure 4.11).

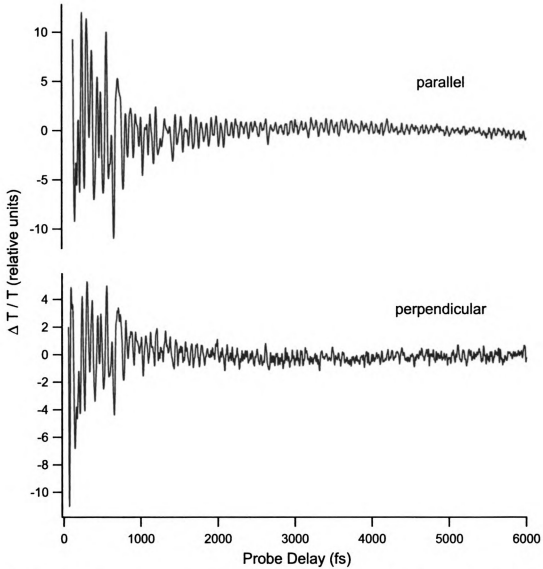

Figure 4.13. Oscillatory components observed in the dynamic-absorption spectrum from DTTCI in methanol at 840 nm; *Top panel:* with polarization analysis of the transmitted probe beam parallel respect to the pump beam's plane of polarization; *Bottom panel:* with polarization analysis of the transmitted probe beam perpendicular with respect to the pump beam's plane of polarization.

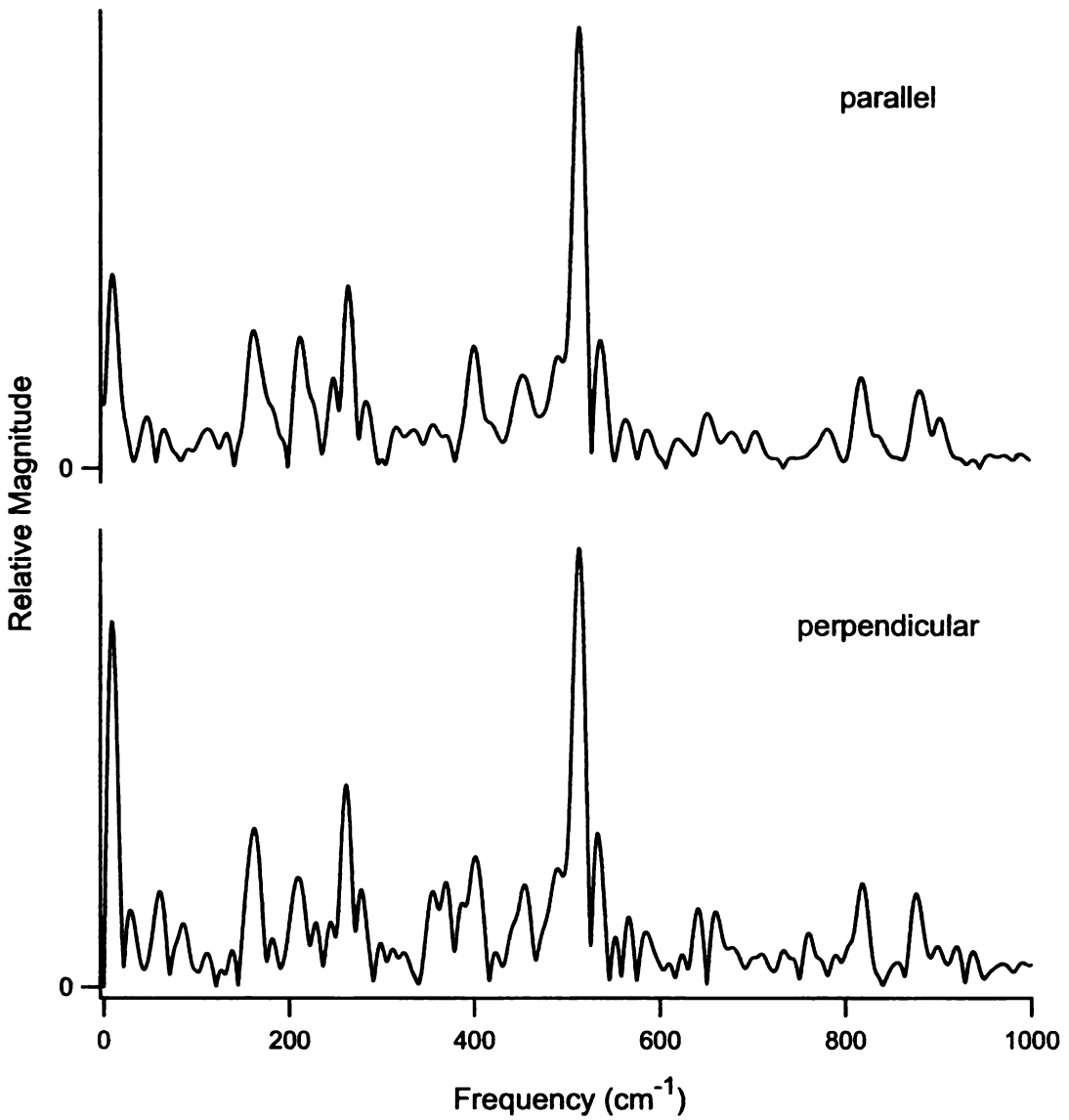

Figure 4.14. Fourier-magnitude spectra obtained from the polarized oscillatory components at 840 nm (see figure 4.13).

observed in the 750–900-cm^{-1} region. These additional frequencies in the excited-state vibrational coherence are observed because DTTCI is a reactive system and has the ability to isomerize. No additional frequencies were observed from the excited state of IR144 because it is unable to isomerize due to the central five-membered ring.

4.3.2 Origin of Vibrational Activity

For vibrational activity to be Albrecht *A*-term active, the excited-state potential-energy surface must be displaced from that of the ground-state surface. In the following, we show that displaced surfaces should be apparent from both the oscillatory signals and the observed Fourier spectra. We use a simple theory to depict the signals that would be produced by wave-packet motion on displaced and non-displaced ground- and excited-state harmonic-oscillator potential-energy surfaces.

Intensity oscillations are simulated as a sum of two damped cosinusoids:

$$I(\omega, t) = \sum_i A_i \exp\left(-\frac{t}{\gamma}\right) \cos(\omega_i t + \phi) \qquad (4.1)$$

In each simulation, the ground- and excited state oscillations have the same damping time (γ = 800 fs), but the phase, ϕ, is shifted by π. The ground-to-excited-state amplitude ratios were chosen to represent three regions of the dynamic-absorption surface. In the stimulated-emission (red) region, the ratio was set to 1:4 because the excited-state signal dominates. At the node region, the contribution from both states is equal, so each amplitude was set to be 2.5. In the ground-state turning point (blue) region, the ratio was set to 4:1 because the ground-state has the largest contribution.To simulate the wave-packet motion that would be observed from displaced potential-energy surfaces, the

vibrational frequency of the ground state was set to 210 cm^{-1} while the excited-state frequency was set to 190 cm^{-1}. In an additional simulation, both frequencies were chosen to be 200 cm^{-1} to simulate the non-displaced potential-energy surfaces.

We chose to depict the displaced potential-energy surfaces as frequency shifts because we are trying to simulate a situation where an electron is excited from a π orbital to a π^* orbital. In this situation, a longer, weaker bond occurs. In the harmonic-oscillator model, the excited-state potential-energy surface would be displaced relative to the ground-state surface. The force contant for the vibration of the bond would be weaker, resulting in a lower vibrational frequency.

The results of displaced potential-energy surfaces are depicted in figure 4.15. The oscillatory signals demonstrate the anti-phase character observed from the ground- and excited-state wave-packet motion. At the node region, a beating character is observed due to the equal amplitudes and shifted frequencies. In the Fourier-intensity spectra, the sign of the intensity indicates the phase of the signal. In the stimulated-emission region, the intensity of the excited-state frequency dominates the observed signals. The intensity of the ground-state frequency dominates the observed signals in the ground-state depletion region. At the node region, the intensity of the ground-state and excited-state frequencies are equal.

Figure 4.16 illustrates what would be observed if the ground- and excited-state potential-energy surfaces were not displaced. Again, the antiphase oscillatory character is observed in the ground-state depletion and stimulated-emission regions, but the oscillatory character disappears at the node. At the node, the oscillatory amplitudes are equal but opposite in phase, therefore one signal cancels the other. The Fourier-intensity spectra

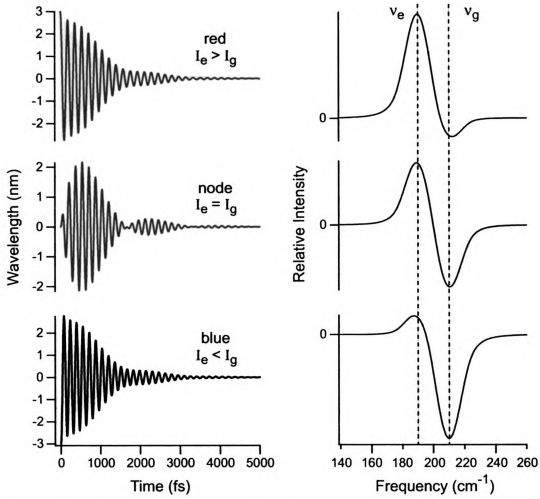

Figure 4.15. *Left*: Demonstration of dynamic-absorption contours from wave-packet motion on displaced ground- and excited-state potential-energy surfaces as the probe wavelength is tuned from red to blue across the node at which the intensity of ground-state depletion and stimulated emission are equal. *Right*: Fourier-intensity spectra corresponding to the dynamic-absorption contours. The sign of the intensity with respect to frequency reports the phase of the signals. The intensity ratios of ground–excited states is set to be 1:4 in the red region, equal at the node and 4:1 in the blue region. The ground-state frequency is 210 cm^{-1} and the excited-state frequency is 190 nm^{-1}.

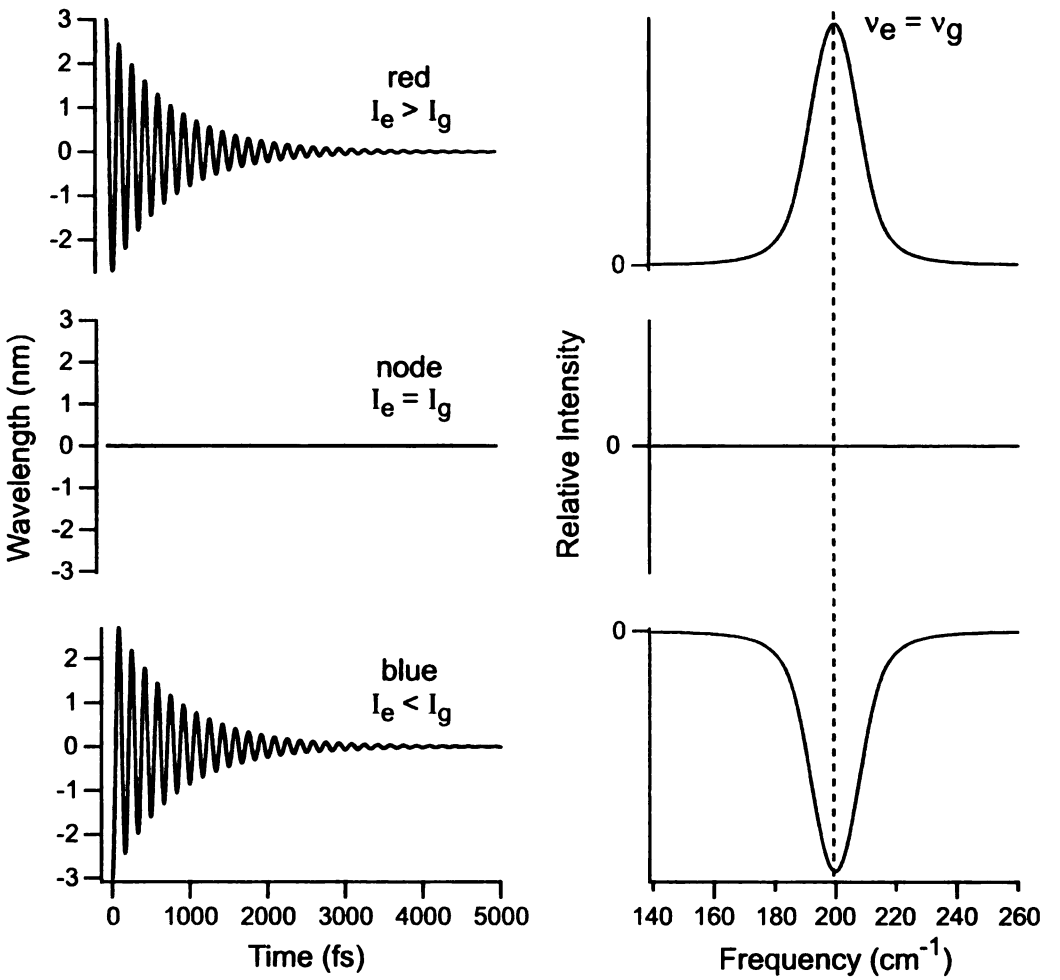

Figure 4.16. *Left*: Demonstration of dynamic-absorption contours from wave-packet motion on non-displaced ground- and excited-state potential-energy surfaces as the probe wavelength is tuned from red to blue across the node at which the intensity of ground-state depletion and stimulated emission are equal. *Right*: Fourier-intensity spectra corresponding to the dynamic-absorption contours. The sign of the intensity with respect to frequency reports the phase of the signals. The intensity ratios of ground–excited states is set to be 1:4 in the red region, equal at the node and 4:1 in the blue region. Both frequencies are 200 cm^{-1}.

show the progression of the dominant signal. In the stimulated-emission region, the intensity is positive indicating dominance by the excited-state, but in the ground-state depletion region, the ground-state signal dominates indicated by the negative intensity. At the node, no frequency peak is observed due to the cancellation of oscillatory signals.

In the contours obtained from both DTTCI and IR144, cancellation of oscillatory character is observed; there is no evidence of a shifted-frequency beating pattern. This indicates that the excited-state potential-energy surface is not displaced from the ground state. In addition, there is no evidence for a shift in mode-frequency when comparing the ground- and excited-state frequency spectra (see figures 4.7 and 4.9). Therefore, we suggest that most of the vibrational modes observed in the vibrational coherence from IR144 and DTTCI cannot be Albrecht *A*-term active.

The vibrational modes that we observed in the vibrational coherence are most likely Albrecht *B*-term active owing to mixing of nearby excited states. Figure 4.17 depicts the potential-energy surfaces for the *trans-cis* isomerization of DTTCI. This model is adapted from the schematic state correlation diagram for the *cis-trans* isomerization of stilbene as depicted by Orlandi and Siebrand.[9,10] In this model, DTTCI is excited from the S_0 state to the non-displaced S_1 state. The S_1 state is able to mix with the nearby S_2 state. As the displacement of the torsional mode increases, the mixing of the S_1 and S_2 states increases. It is from the S_2 state that isomerization occurs as DTTCI relaxes to either the *trans* or *cis* form.[2,3] Through the mixing of the S_1 and S_2 states, DTTCI is able to obtain resonance Raman activity via the Albrecht *B*-term mechanism.

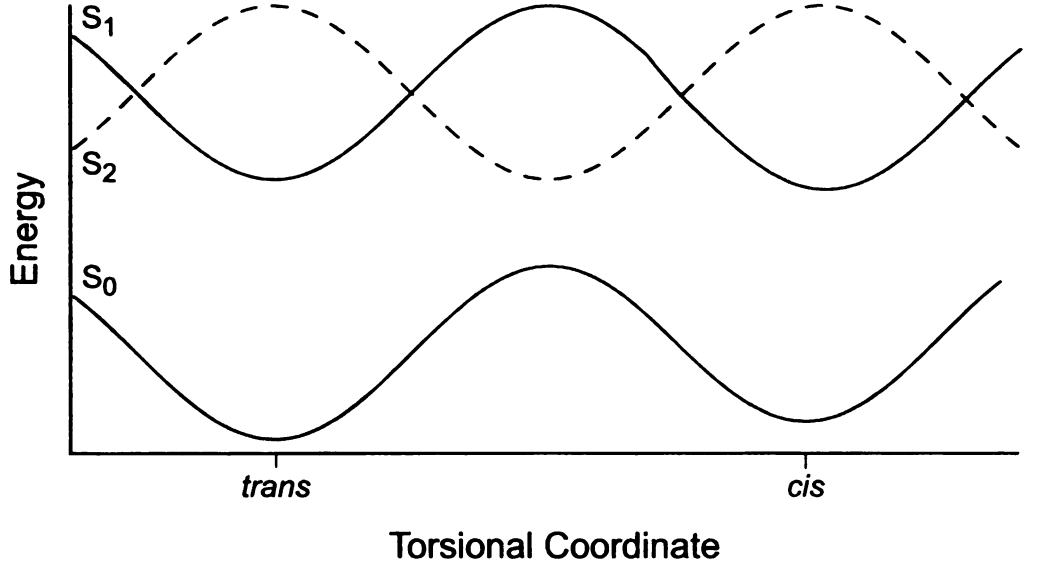

Figure 4.17. Potential-energy surfaces for the *trans-cis* isomerization of DTTCI. Adapted from the schematic state correlation diagram for the *cis-trans* isomerization of stilbene as depicted by Orlandi and Siebrand.[9,10]

4.3.3 Polarized Vibrational Coherence

In conventional Raman spectroscopy, choice of excitation energies can distinguish the method through which vibrational modes obtain Raman activity. In pre-resonance Raman spectroscopy, Albrecht *B*-term active modes are enhanced, while Albrecht *A*-term active modes are stronger in resonance Raman spectroscopy. Depolarization ratios in resonance Raman spectroscopy are used also to determine Raman activity. Depolarization ratios, ρ_s, are defined as the ratio of the intensities $I_{//}$ for exciting light linearly polarized parallel to the direction of observation and $I_{\perp}$ for exciting light polarized perpendicular to it.[11] Vibrational modes that are totally-symmetric (Albrecht *A*-term) modes are polarized, while non-totally-symmetric (Albrecht *B*-term) modes are depolarized.[12] In the experiments presented in this chapter, effects from polarization are not observed. This is consistent with the lack of shifts in the vibrational mode frequencies. Both observations are indications of Raman activity through the Albrecht *B*-term mechanism.

4.3.4 Rapidly Damped Vibrational Coherence

Two time regions of vibrational dephasing are discernible in the oscillatory components observed in the dynamic-absorption spectrum from DTTCI in methanol. In addition to the long-lived vibrational coherence in the 1000–6000-fs region, we see vibrational coherence that is rapidly damped in the 200–1000-fs region (γ = 200 fs). The broad line shapes that would be expected from this rapidly-damped region are not observed in the frequency domain due to the Hanning window function used to obtain the Fourier-magnitude spectra. The Hanning window greatly reduces the intensity of this time

region, so the Fourier-magnitude spectra are dominated by the vibrational coherence observed in the 1000–6000-fs region.

The rapidly-damped vibrational coherence observed from DTTCI is similar to the rapidly-damped features observed from the dipyridine-bacteriochlorophyll a complex in the 200–600-fs region.[13] These features are assigned to an intermolecular mode between the bacteriochlorophyll molecule and the pyridine solvent molecule. A broad distribution of frequencies is required to describe the rapidly-damped character resulting from a disordered ensemble of solvated bacteriochlorophyll structures. We suggest that the rapidly-damped vibrational coherence observed from DTTCI is due to solvated DTTCI structures. Additional experiments studying the rapidly-damped character observed from DTTCI will be discussed in the following chapter.

4.4 References

(1) Carson, E. A.; Diffey, W. M.; Shelly, K. R.; Lampa-Pastirk, S.; Dillman, K. L.; Schleicher, J. M.; Beck, W. F. *J. Phys. Chem. A* **2004**, *108*, 1489–1500.

(2) Sahyun, M. R. V.; Serpone, N. *J. Phys. Chem. A* **1997**, *101*, 9877–9883.

(3) Sanchez-Galvez, A.; Hunt, P.; Robb, M. A.; Olivucci, M.; Vreven, T.; Schlegel, H. B. *J. Am. Chem. Soc.* **2000**, *122*, 2911–2924.

(4) Lakowicz, J. R. *Principles of Fluorescence Spectroscopy*; Second ed.; Kluwer Academic/Plenum Publishers: New York, 1999.

(5) Lampa-Pastirk, S.; Beck, W. F. *J. Phys. Chem. B* **2004**, *108*, 12602–12607.

(6) Cantor, C. R.; Schimmel, P. R. *Biophysical Chemistry. Part II: Techniques for the Study of Biological Structure and Function*; W. H. Freeman and Company: San Francisco, 1980.

(7) Siano, D. B.; Metzler, D. E. *J. Chem. Phys.* **1969**, *51*, 1856–1861.

(8) McMorrow, D.; Lotshaw, W. T. *Chem. Phys. Lett.* **1990**, *174*, 85–94.

(9) Orlandi, G.; Siebrand, W. *Chem. Phys. Lett.* **1975**, *30*, 352–354.

(10) Kessinger, M.; Michl, J. *Excited States and Photochemistry of Organic Molecules*; VCH Publishers, Inc.: New York, 1995.

(11) Schrötter, H. W. In *Raman Spectroscopy*; Szymanski, H. A., Ed.; Plenum Press: New York, 1970; Vol. 2, p 69–120.

(12) Woodward, L. A. In *Raman Spectroscopy*; Szymanski, H. A., Ed.; Plenum Press: New York, 1967; Vol. 1, p 1–43.

(13) Shelly, K. R.; Carson, E. A.; Beck, W. F. *J. Am. Chem. Soc.* **2003**, *125*, 11810–11811.

CHAPTER 5

DYNAMIC-ABSORPTION CONTOURS FROM DTTCI: 2. VIBRATIONAL COHERENCE FROM ORDERED AND DISORDERED POLAR-SOLVENT MODES

5.0 Introduction

Recent studies of the solvated electron by Tauber and Mathies[1,2] have shown that there are coupled solvent-chromophore vibrational modes. They suggest that these are the first pure observations of the vibrational coupling of the electronic transition of the solute with the vibrational modes of the solvent. Previously in the Beck group, vibronic coupling of bacteriochlorophyll a with pyridine solvent has been observed.[3] In this chromophore-solvent system, rapidly-damped vibrational coherence was observed.

We observe vibrational coherence from DTTCI in polar solvents that exhibits two different damping time scales. A rapidly-damped component is observed for 1500 fs and a long-lived component that continues for 5000 fs. In addition, a number of changes in the vibrational coherence is observed as a result of the $\pi \rightarrow \pi^*$ transition, including the appearance of new features in the 100-cm^{-1} and > 750-cm^{-1} regions and an increase in the relative area arising from the rapidly damped portion. We suggest that these results can be explained by a change in the shape of the π-electron density.

5.1 Experimental

5.1.1 Sample Preparation

DTTCI was obtained from Exciton and used as received. Samples were dissolved in methanol (Spectrum, spectrophotometric grade), acetonitrile (EM Science, HPLC grade) or dimethylsulfoxide (DMSO; Spectrum, reagent grade) to obtain an absorbance of 0.4–0.6 at λ_{max} for a 1-mm path length; the DTTCI solution was passed through a 0.22-μm filter prior to use.

5.1.2 Continuous-Wave Spectroscopy

Absorption spectra were obtained with 2-nm spectral band pass at 22°C with a Hitachi U-2000 spectrophotometer and LabVIEW (National Instruments) routines.[4] Fluorescence spectra were acquired with a Hitachi F-4500 fluorescence spectrophotometer (2.5-nm excitation at 755 nm and 5-nm emission band pass).

5.1.3 Femtosecond Spectroscopy

For the experiments presented in this chapter, the Murnane-Kapteyn oscillator, described in chapter two, was adjusted to produce 12-fs pulses ($sech^2$) with a band width of 820-cm^{-1} (fwhm) centered at 800 nm. Samples for femtosecond spectroscopy were held at room temperature (22°C) in a fused-silica flow cuvette with 1-mm path length. The flow rate was 6 mL/min. The absorption spectrum of the sample was monitored for changes arising from photochemistry or permanent photobleaching.

5.2 Results

5.2.1 Continuous-Wave Spectroscopy

The absorption and fluorescence spectra of DTTCI in methanol, DMSO and acetonitrile at room temperature are shown in figure 5.1. The spectra are plotted as $A(\nu)/\nu$ and $F(\nu)/\nu^3$, respectively with normalization to unit area. The integrals of these quantities report the dipole strength, the square of the transition-dipole moment.[5,6] The fluorescence spectra can be described by a single lognormal lineshape, while the absorption spectra are best described by a sum of two lognormal lineshapes [7,8]. Fit parameters listed in table 5.1 describe the center of the v = 0 line (ν_{00}), mode progession for the v = 1 line ($\Delta\nu$) and the half-width of lineshape ($width_{00}$). DTTCI in DMSO exhibits a large solvatochromatic shift to the red and a change in linewidths when compared to the other solvents.

The spectrum from the Murnane-Kapteyn oscillator (11 480–13 343 cm^{-1}, with peak intensity at 12 580 cm^{-1}) overlaps with most of the fluorescence spectra, but only the red tail of the absorption spectra for methanol and acetonitrile. The laser spectrum overlaps with more of the absorption spectrum of DTTCI in DMSO due to the solvatochromatic shift. As used in the short-pulse dynamic-absorption experiments, the probe spectrum overlaps with much of the stimulated-emission spectrum but a smaller portion of the ground-state depletion spectrum.

5.2.2 Dynamic-Absorption Experiments

The dynamic-absorption spectrum from DTTCI in each solvent was acquired as a set of single-wavelength transients spanning most of the 110-nm range of transmitted probe

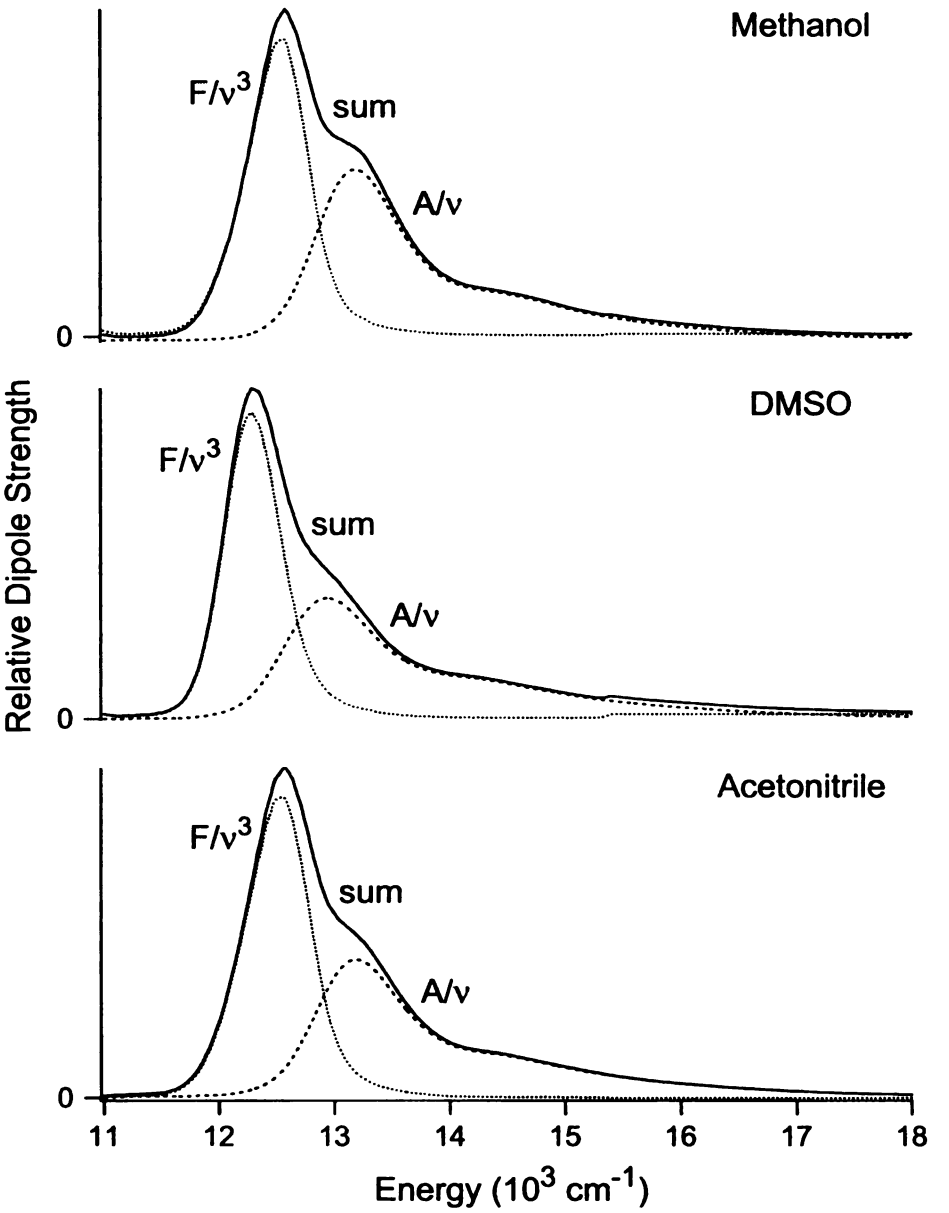

Figure 5.1. Continuous-wave fluorescence-emission spectra (dotted line), absorption spectra (dashed line) and their sum (solid line) from DTTCI in methanol (top), DMSO (middle) and acetonitrile (bottom), plotted as relative dipole strengths. Spectra are normalized to unit area. The fluorescence spectra were excited at 755 nm (13 250 cm^{-1}).

Table 5.1. Fit Parameters for the Absorption and Fluorescence Spectra of DTTCI in the Three Solvents.

Parameter		Methanol	DMSO	Acetonitrile
Absorption	ν_{00} (cm^{-1})	13289	13090	13312
	$width_{00}$ (cm^{-1})	714	841	773
	$\Delta\nu$ (cm^{-1})	1504	1629	1561
Emission	ν_{00} (cm^{-1})	12529	12301	12519
	$width_{00}$ (cm^{-1})	442	399	444

wavelengths from the Murnane-Kapteyn oscillator. The spacing of the probe wavelengths matched the spectral band pass of the monochromator (4 nm). The contour representations of the dynamic-absorption surfaces from DTTCI in each of the solvents are shown in figure 5.2. The anti-phase character of the contour surfaces, as described in chapter 3, was used to determine the ground-state depletion and excited-state emission regions, as described previously in chapter three.[4]

5.2.3 Ground-State Vibrational Coherence Analysis.

Figure 5.3a shows a contour line from the ground-state turning-point region of DTTCI in methanol centered at 790 nm. The contour line exhibits vibrational dephasing on two time scales. A rapidly-damped oscillatory signal is observed in the 0–1500-fs region of the contour line and a long-lived oscillatory signal that continues through the 2000–6000-fs region of the contour line.

The 2000–5000-fs region of the contour line was fit to a sum of damped cosinusoids:

$$I(t) = \sum_i A_i \exp\left(-\frac{t}{\gamma_i}\right) \cos(\omega_i t + \phi_i) \qquad (5.1)$$

Intensities A_i, frequencies ω_i, damping times γ_i and phases ϕ_i were optimized using the program pro Fit (Quansoft). The fit obtained for the long-lived oscillatory signal is a fair representation of that portion of the contour line (see figure 5.3b). A reverse-predicted signal was calculated using the fit parameters listed in table 5.2. As shown in figure 5.3c, the reverse-predicted signal is a poor representation of the early-time portion of the contour line. A difference signal was calculated by subtracting the reverse-predicted signal from the contour line. The difference signal, shown in figure 5.3d, represents the

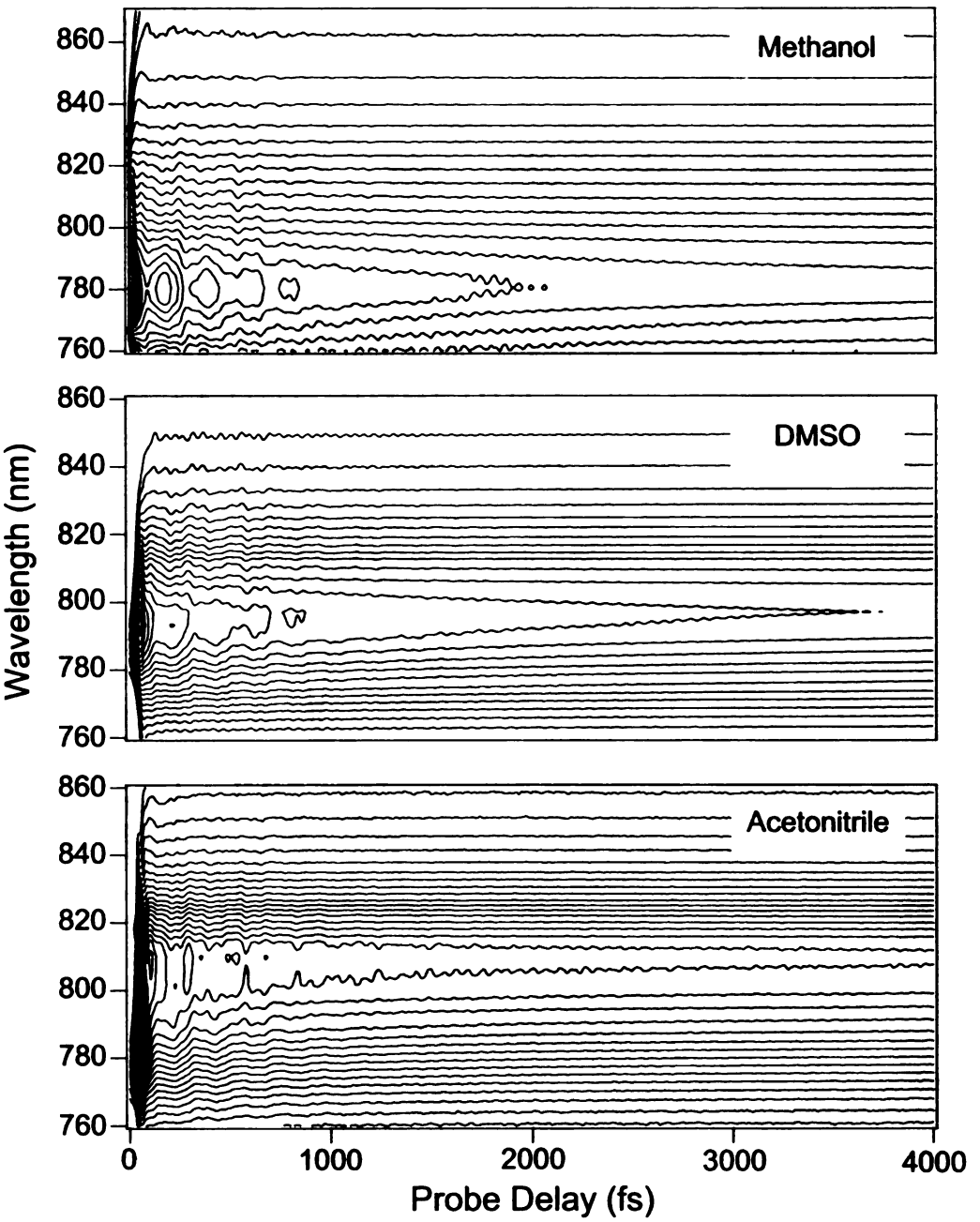

Figure 5.2. Dynamic-absorption contours of DTTCI in methanol (top), DMSO (middle) and acetonitrile (bottom).

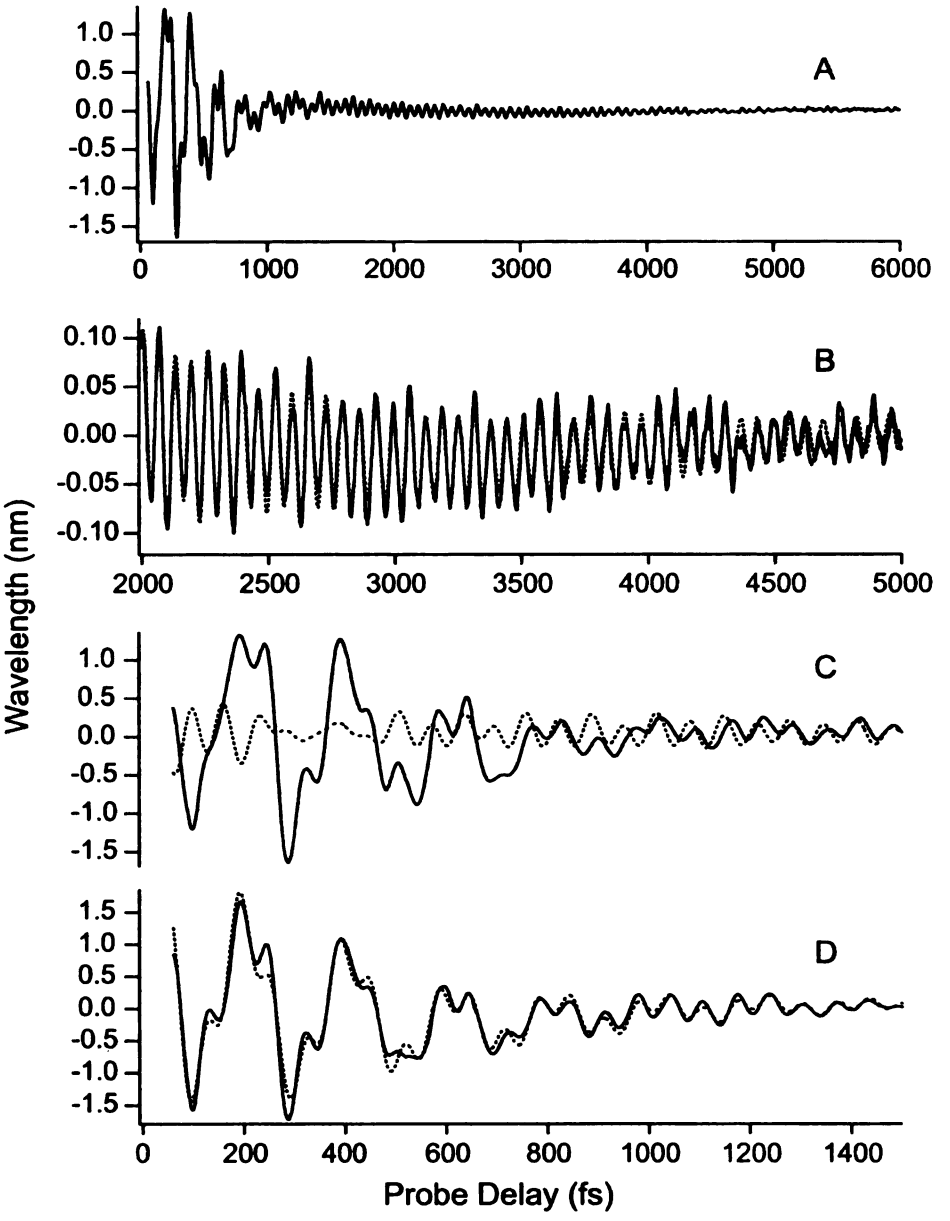

Figure 5.3. Isolation of rapidly-damped ground-state vibrational coherence from the dynamic-absorption contour observed at 790 nm from DTTCI in methanol: a.) contour line over 0–6000 fs range; b.) expanded view over 2000–5000-fs region and a fit to a sum of damped cosinusoids (dotted line); c.) expanded view over 0–1500-fs region and reverse-predicted signal (dotted line); d.) difference between contour line and reverse-predicted signal and a fit to a sum of damped cosinusoids (dotted line).

Table 5.2. Frequencies, Relative Amplitudes, Damping Constants and Phases for Oscillatory Components Observed in the Ground-State Contour Line at 790 nm from the Dynamic-Absorption Spectrum of DTTCI in Methanol.

Frequency (cm^{-1})	Amplitude[a]	Damping Constant (fs)	Phase
7	0.46	2256	1.17
161	0.06	2072	0.02
195	0.12	1269	-0.21
263	0.81	872	0.20
400	0.40	903	-0.33
483	0.35	1548	-2.89
508	1.00	2045	-2.88
538	0.70	1040	2.44
560	0.34	943	-2.05

[a] Relative to the amplitude of the 508-cm^{-1} component.

rapidly-damped oscillatory signal from the contour line. The difference signal was fit to another sum of damped cosinusoids (see equation 5.1) with short damping times. The fit parameters are listed in table 5.3. The sum of the long-lived and rapidly-damped fits almost completely describes the oscillatory character of the contour line, as shown in figure 5.4.

The synthetic spectra shown in figure 5.5 were obtained from the parameters in tables 5.2–5.3 using a sum of Lorentzian lineshapes:[9]

$$I(\omega) = \sum_i \frac{A_i}{4\gamma_i^2(\omega - \omega_i)^2 + 1} \tag{5.2}$$

Figures 5.5a and 5.5b represent the best estimates for the modulation frequencies ω_i, intensities A_i and damping times γ_i for the long-lived and rapidly-damped oscillatory signals from DTTCI in methanol that would be retrieved by Fourier analysis. The spectrum shown in figure 5.5c is the sum of the magnitude spectra from the long-lived and rapidly-damped oscillatory signals. The contribution from the rapidly-damped oscillatory character is shaded. A significant contribution from the rapidly-damped oscillations is observed in the low-frequency region. Small shifts in frequency are also observed when comparing the long-lived and rapidly-damped fit magnitude spectra.

Figure 5.6a shows the contour line from the ground-state turning-point region of DTTCI in DMSO centered at 808 nm. Again, the 2000–5000-fs region of the contour line was fit to a sum of damped cosinusoids (figure 5.6b) and the rapidly-damped component was obtained as the difference between the contour line and the reverse-predicted model (figure 5.6c) and fit to a sum of damped cosinusoids (figure 5.6d). The sum of the damped-cosinusoidal fits over the 2000–5000-fs region of the contour line and the

Table 5.3. Frequencies, Relative Amplitudes, and Damping Constants and Phases for Oscillatory Components Observed in the Ground-State Rapidly-Damped Vibrational Coherence at 790 nm from the Dynamic-Absorption Spectrum of DTTCI in Methanol.

Frequency (cm^{-1})	Amplitude[a]	Damping Constant (fs)	Phase
21	4.08	487	-0.27
94	4.23	210	0.82
163	11.65	365	0.00
508	2.92	668	-0.62

[a] Relative to the amplitude of the 508-cm^{-1} component in Table 5.2.

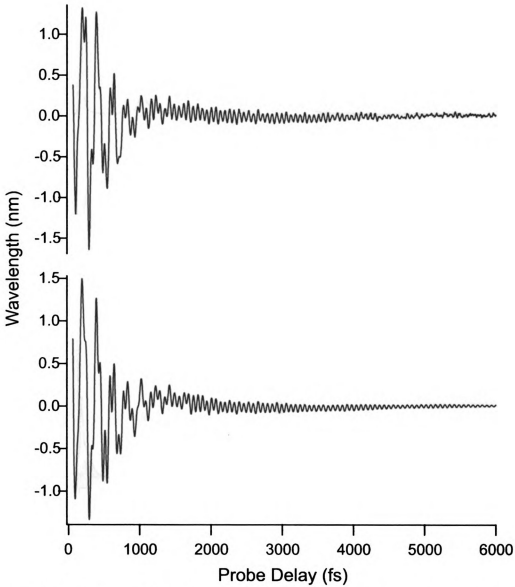

Figure 5.4. *Top*: Dynamic-absorption contour line observed at 790 nm from DTTCI in methanol. *Bottom*: Sum of damped-cosinusoidal fits over 2000–5000-fs region of contour line (see figure 5.3b) and 0–1500-fs region of difference signal (see figure 5.3d).

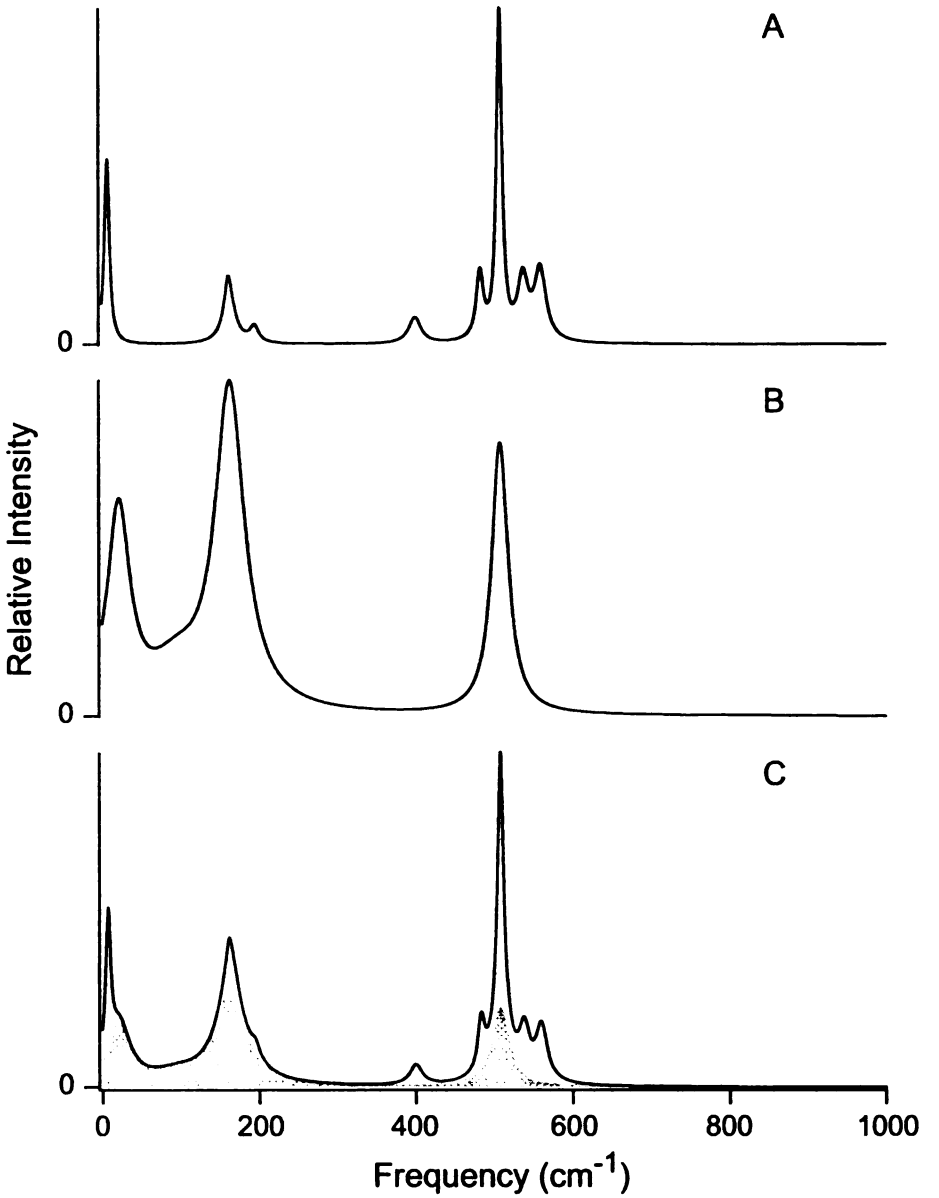

Figure 5.5. Magnitude spectra from the ground-state vibrational-coherence from DTTCI in methanol: a.) synthetic spectrum from the fitted 2000–5000-fs region; b.) synthetic spectrum from the fitted 0–1500-fs region of the difference signal; c.) sum of a and b with the shaded region showing contribution from b. Lorentzian lineshapes were generated from fit parameters (tables 5.2–5.3) using equation 5.2. Spectra are normalized to full scale for the most intense feature.

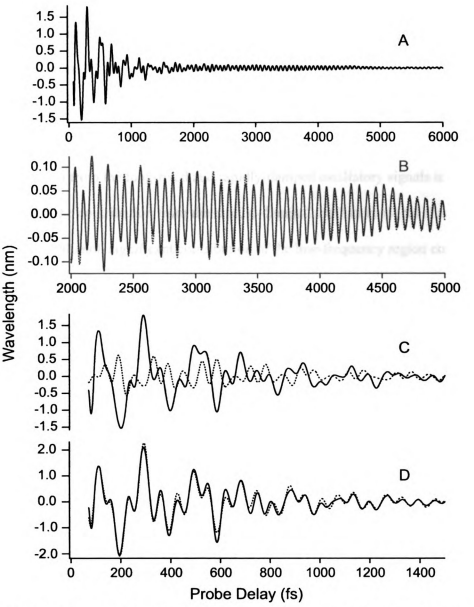

Figure 5.6. Isolation of rapidly-damped ground-state vibrational coherence from the dynamic-absorption contour observed at 808 nm from DTTCI in DMSO: a.) contour line over 0–6000 fs range; b.) expanded view over 2000–5000-fs region and a fit to a sum of damped cosinusoids (dotted line); c.) expanded view over 0–1500-fs region and reverse-predicted signal (dotted line); d.) difference between contour line and reverse-predicted signal and a fit to a sum of damped cosinusoids (dotted line).

0–1500-fs region of the difference signal almost completely describes the oscillatory character of the contour line, as shown in figure 5.7.

Figures 5.8a and 5.8b represent the best estimates for the spectra that would be retrieved by Fourier analysis from the long-lived and rapidly-damped oscillatory signals from DTTCI in DMSO using the fit parameters in tables 5.4–5.5. The sum of the magnitude spectra from the long-lived and rapidly-damped oscillatory signals is shown in figure 5.8c with the contribution from the rapidly-damped oscillatory signal shaded. As observed with methanol, significant contribution of the low-frequency region comes from the rapidly-damped oscillations and frequency shifts are observed when comparing the magnitude spectra.

Figure 5.9a shows the contour line from the ground-state turning-point region of DTTCI in acetonitrile centered at 820 nm. Again, the 2000–5000-fs region of the contour line was fit to a sum of damped cosinusoids (figure 5.9b) and the rapidly-damped component was obtained as the difference between the contour line and the reverse-predicted model (figure 5.9c) and fit to a sum of damped cosinusoids (figure 5.9d). The sum of the damped-cosinusoidal fits over the 2000–5000-fs region of the contour line and the 0–1500-fs region of the difference signal almost completely describes the oscillatory character of the contour line, as shown in figure 5.10.

Figures 5.11a and 5.11b represent the best estimates for the spectra that would be retrieved by Fourier analysis from the long-lived and rapidly-damped oscillatory signals from DTTCI in acetonitrile using the fit parameters in tables 5.6–5.7. The sum of the magnitude spectra from the long-lived and rapidly-damped oscillatory signals is shown in figure 5.11c with the contribution from the rapidly-damped oscillatory signal shaded. As

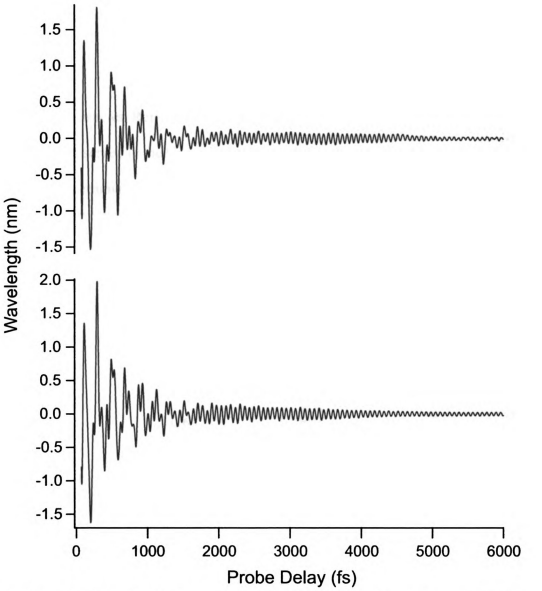

Figure 5.7. *Top*: Dynamic-absorption contour line observed at 808 nm from DTTCI in DMSO. *Bottom*: Sum of damped-cosinusoidal fits over 2000–5000-fs region of contour line (see figure 5.6b) and 0–1500-fs region of difference signal (see figure 5.6d).

Table 5.4. Frequencies, Relative Amplitudes, and Damping Constants for Oscillatory Components Observed in the Ground-State Contour Line at 808 nm from the Dynamic-Absorption Spectrum of DTTCI in DMSO.

Frequency (cm^{-1})	Amplitude[a]	Damping Constant (fs)	Phase
17	0.12	2211	2.23
165	1.65	776	-1.53
195	0.05	2629	-2.17
270	0.49	1293	-2.24
392	0.61	961	0.54
486	0.63	1154	-2.34
509	1.00	2990	0.12
519	0.53	1678	0.54
535	0.06	1922	1.03
684	1.18	633	-0.34

[a] Relative to the amplitude of the 509-cm^{-1} component.

Table 5.5. Frequencies, Relative Amplitudes, and Damping Constants for Oscillatory Components Observed in the Ground-State Rapidly-Damped Vibrational Coherence at 808 nm from the Dynamic-Absorption Spectrum of DTTCI in DMSO.

Frequency (cm^{-1})	Amplitude[a]	Damping Constant (fs)	Phase
31	3.19	198	2.97
165	9.56	483	2.88
270	3.30	552	1.61
414	13.67	126	-2.40
516	6.59	641	-2.62

[a] Relative to the amplitude of the 509-cm^{-1} component in Table 5.4.

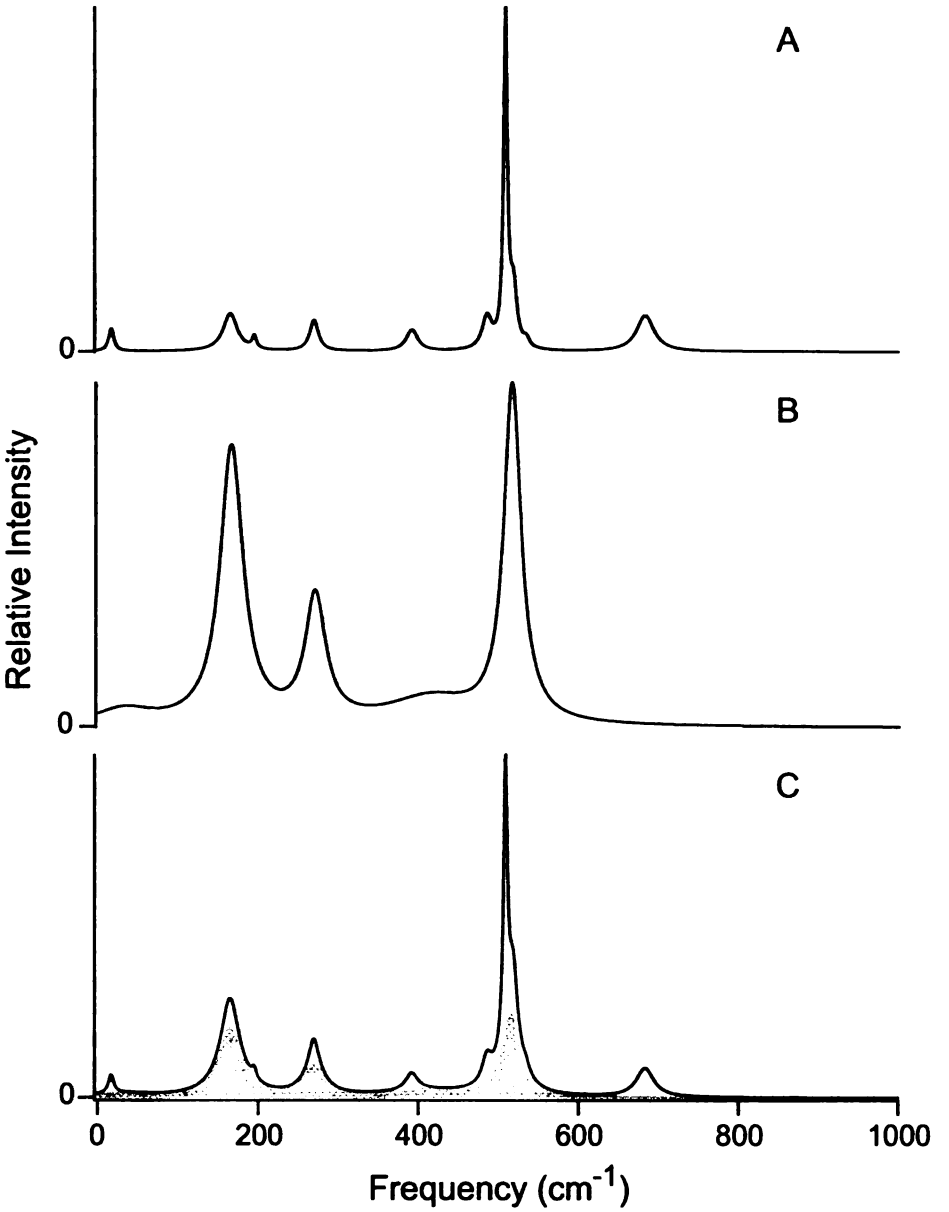

Figure 5.8. Magnitude spectra from the ground-state vibrational-coherence from DTTCI in DMSO: a.) synthetic spectrum from the fitted 2000–5000-fs region; b.) synthetic spectrum from the fitted 0–1500-fs region of the difference signal; c.) sum of a and b with the shaded region showing contribution from b. Lorentzian lineshapes were generated from fit parameters (tables 5.4–5.5) using equation 5.2. Spectra are normalized to full scale for the most intense feature.

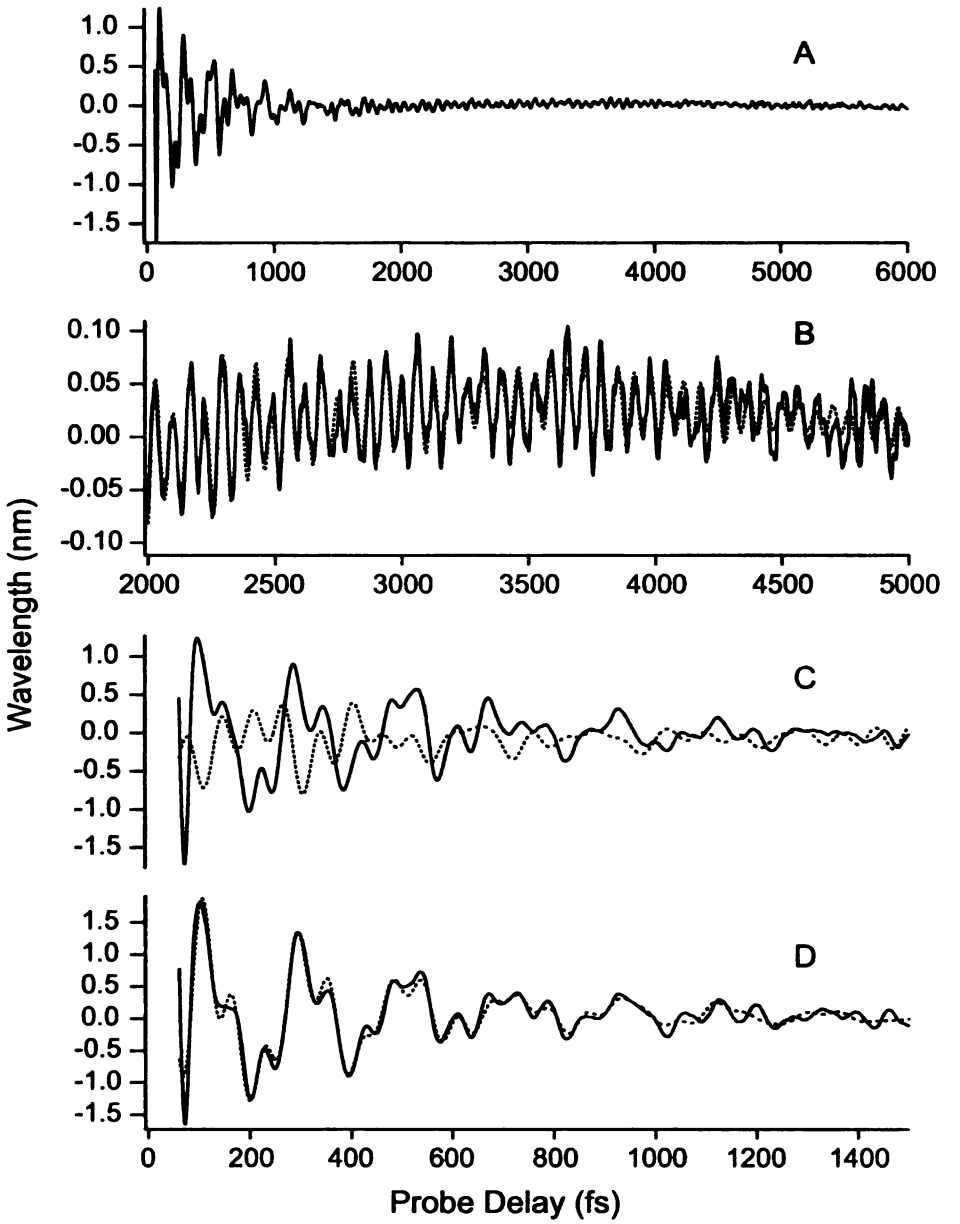

Figure 5.9. Isolation of rapidly-damped ground-state vibrational coherence from the dynamic-absorption contour observed at 820 nm from DTTCI in acetonitrile: a.) contour line over 0–6000 fs range; b.) expanded view over 2000–5000-fs region and a fit to a sum of damped cosinusoids (dotted line); c.) expanded view over 0–1500-fs region and reverse-predicted signal (dotted line); d.) difference between contour line and reverse-predicted signal and a fit to a sum of damped cosinusoids (dotted line).

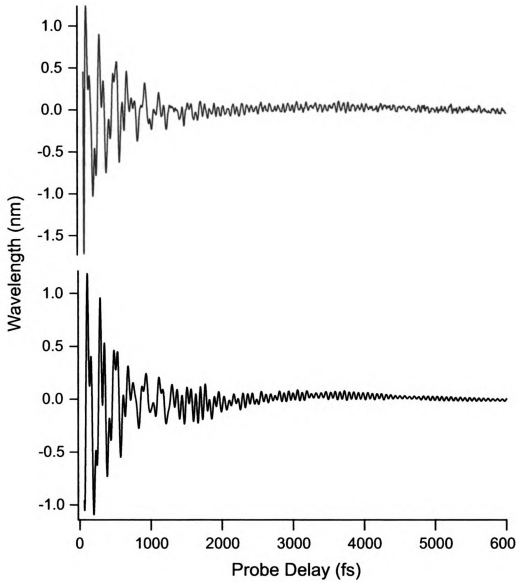

Figure 5.10. *Top*: Dynamic-absorption contour line observed at 820 nm from DTTCI in acetonitrile. *Bottom*: Sum of damped-cosinusoidal fits over 2000–5000-fs region of contour line (see figure 5.9b) and 0–1500-fs region of difference signal (see figure 5.9d).

Table 5.6. Frequencies, Relative Amplitudes, and Damping Constants for Oscillatory Components Observed in the Ground-State Contour Line at 820 nm from the Dynamic-Absorption Spectrum of DTTCI in Acetonitrile.

Frequency (cm^{-1})	Amplitude[a]	Damping Constant (fs)	Phase
5	1.01	2956	-2.44
154	3.73	574	-0.15
202	0.10	2529	-2.64
262	1.48	1070	0.22
394	1.52	876	-0.05
493	1.84	1047	0.56
511	1.00	2675	0.36
539	0.89	1415	2.27
562	0.43	1454	-2.25

[a] Relative to the amplitude of the 511-cm^{-1} component.

Table 5.7. Frequencies, Relative Amplitudes, and Damping Constants for Oscillatory Components Observed in the Ground-State Rapidly-Damped Vibrational Coherence at 820 nm from the Dynamic-Absorption Spectrum of DTTCI in Acetonitrile.

Frequency (cm^{-1})	Amplitude[a]	Damping Constant (fs)	Phase
12	2.50	824	2.00
161	11.30	492	3.10
202	4.04	406	-0.67
398	2.56	556	2.38
529	9.59	312	-2.21

[a] Relative to the amplitude of the 511-cm^{-1} component in Table 5.6.

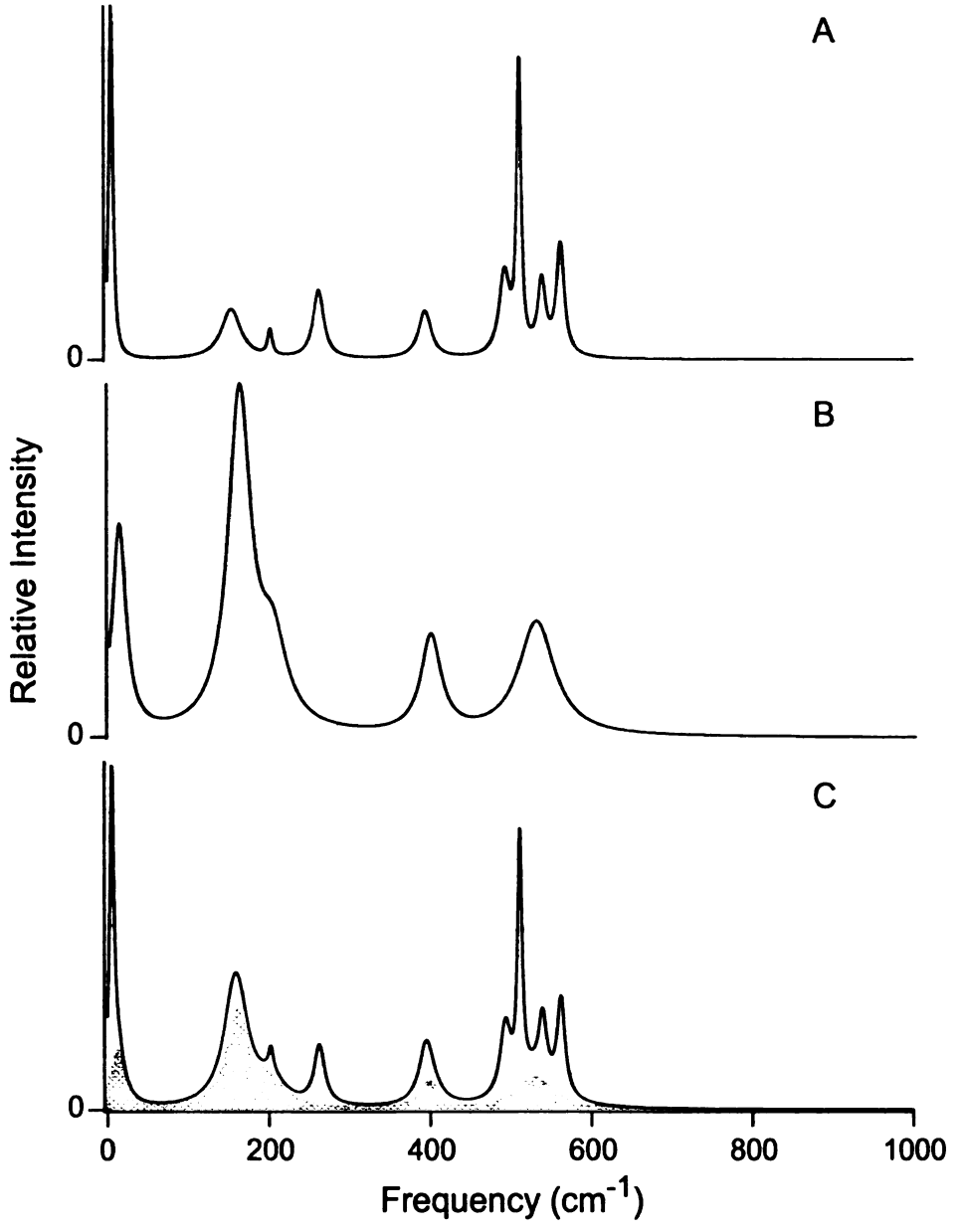

Figure 5.11. Magnitude spectra from the ground-state vibrational-coherence from DTTCI in acetonitrile: a.) synthetic spectrum from the fitted 2000–5000-fs region; b.) synthetic spectrum from the fitted 0–1500-fs region of the difference signal; c.) sum of a and b with the shaded region showing contribution from b. Lorentzian lineshapes were generated from fit parameters (tables 5.6–5.7) using equation 5.2. Spectra are normalized to full scale for the most intense feature.

observed with methanol, significant contribution of the low-frequency region comes from the rapidly-damped oscillations and frequency shifts are observed when comparing the magnitude spectra.

Comparison of the synthetic spectra from each of the solvents shows that both the long-lived and rapidly-damped oscillatory components are different for each solvent. DMSO has much smaller contribution from the $<40cm^{-1}$ frequency, unlike methanol and acetonitrile which have significant contribution from this frequency. The frequencies needed to fit the long-lived oscillatory signals in each of the solvents are slightly shifted from one another.

5.2.4 Excited-State Vibrational Coherence Analysis.

Figure 5.12a shows the contour line from the excited-state region of DTTCI in methanol centered at 840 nm. Again, the 2000–5000-fs region of the contour line was fit to a sum of damped cosinusoids (figure 5.12b) and the rapidly-damped component was obtained as the difference between the contour line and the reverse-predicted model (figure 5.12c) and fit to a sum of damped cosinusoids (figure 5.12d). The sum of the damped-cosinusoidal fits over the 2000–5000-fs region of the contour line and the 0–1500-fs region of the difference signal almost describes the oscillatory character of the contour line, as shown in figure 5.13.

Figures 5.14a and 5.14b represent the best estimates for the spectra that would be retrieved by Fourier analysis from the long-lived and rapidly-damped oscillatory signals from DTTCI in methanol using the fit parameters in tables 5.8–5.9. The sum of the magnitude spectra from the long-lived and rapidly-damped oscillatory signals is shown in

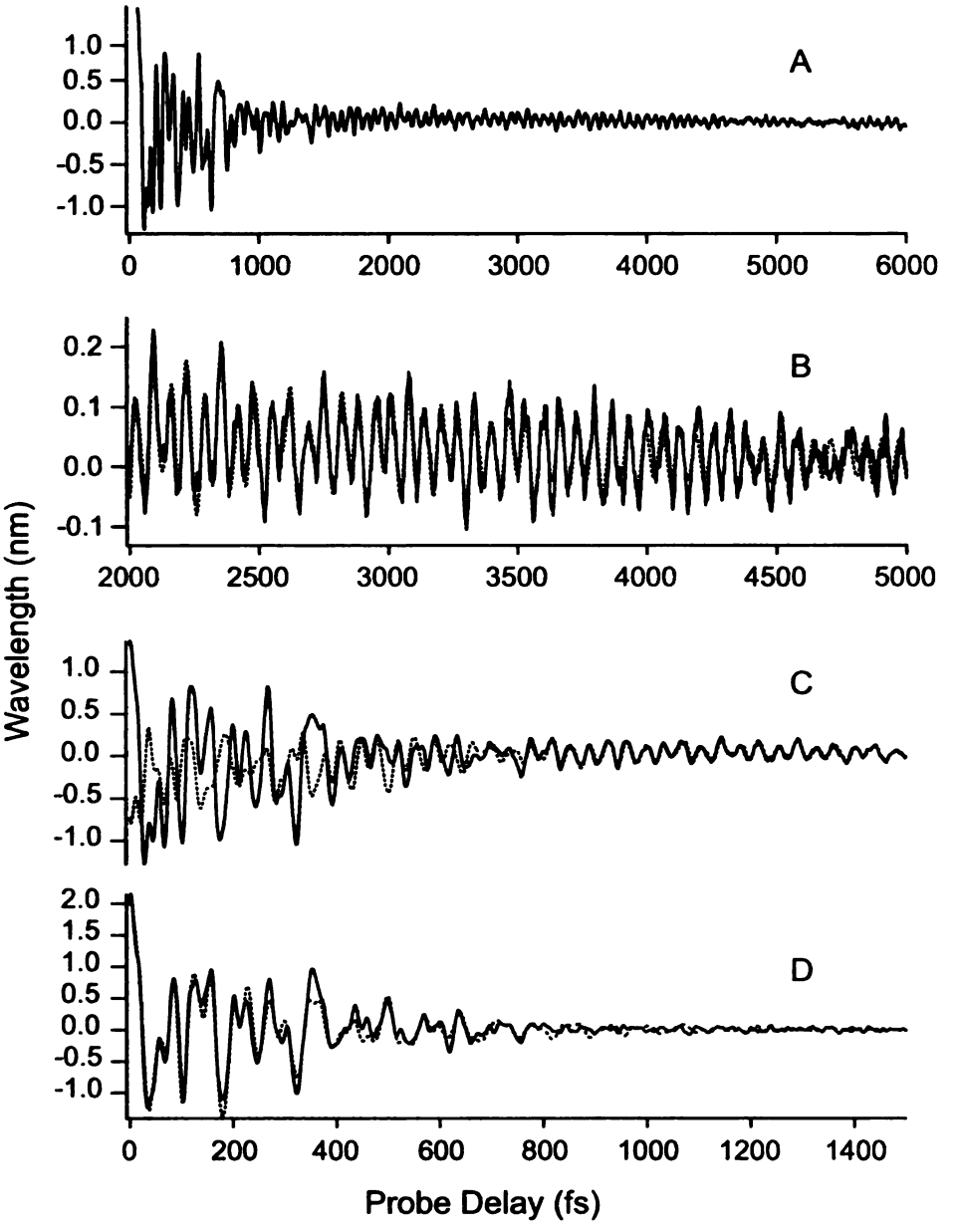

Figure 5.12. Isolation of rapidly-damped excited-state vibrational coherence from the dynamic-absorption contour observed at 840 nm from DTTCI in methanol: a.) contour line over 0–6000 fs range; b.) expanded view over 2000–5000-fs region and a fit to a sum of damped cosinusoids (dotted line); c.) expanded view over 0–1500-fs region and reverse-predicted signal (dotted line); d.) difference between contour line and reverse-predicted signal and a fit to a sum of damped cosinusoids (dotted line).

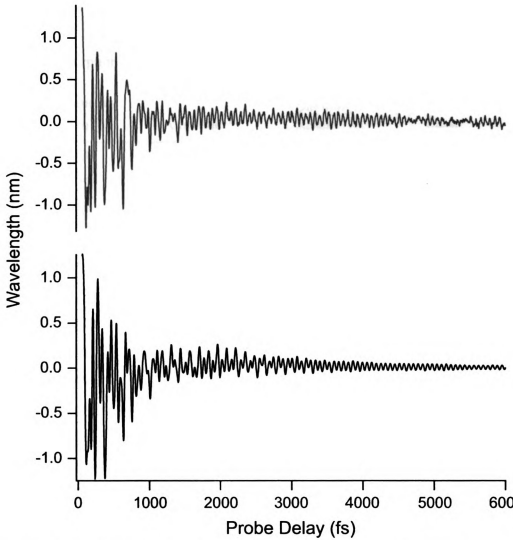

Figure 5.13. *Top*: Dynamic-absorption contour line observed at 840 nm from DTTCI in methanol. *Bottom*: Sum of damped-cosinusoidal fits over 2000–5000-fs region of contour line (see figure 5.12b) and 0–1500-fs region of difference signal (see figure 5.12d).

Table 5.8. Frequencies, Relative Amplitudes, Damping Constants and Phases for Oscillatory Components Observed in the Excited-State Contour Line at 840 nm from the Dynamic-Absorption Spectrum of DTTCI in Methanol.

Frequency (cm^{-1})	Amplitude[a]	Damping Constant (fs)	Phase
3	1.82	1718	2.86
5	1.22	1544	1.60
36	0.35	1111	2.01
154	0.57	1149	-0.25
229	0.03	2369	0.03
256	0.72	1373	-0.25
270	1.39	843	0.87
381	0.31	1163	1.34
464	0.18	943	-0.39
482	0.11	3485	-0.65
510	1.00	2693	0.12
539	0.59	1268	-1.66
557	0.57	997	2.31
733	0.11	1307	-2.59
814	0.66	855	0.36
868	0.31	1088	1.87
878	0.28	914	1.30

[a] Relative to the amplitude of the 510-cm^{-1} component.

Table 5.9. Frequencies, Relative Amplitudes, and Damping Constants and Phases for Oscillatory Components Observed in the Excited-State Rapidly-Damped Vibrational Coherence at 840 nm from the Dynamic-Absorption Spectrum of DTTCI in Methanol.

Frequency (cm^{-1})	Amplitude[a]	Damping Constant (fs)	Phase
155	4.38	474	1.95
264	5.07	656	-3.05
394	1.36	648	0.97
506	6.52	311	1.22
559	1.34	812	-0.48
600	1.47	380	-0.03
643	2.11	254	0.41
812	0.95	448	1.84

[a] Relative to the amplitude of the 508-cm^{-1} component in Table 5.8.

figure 5.14c with the contribution from the rapidly-damped oscillatory signal shaded. As observed with DTTCI in methanol in the ground state, significant contribution of the low-frequency region comes from the rapidly-damped oscillations and frequency shifts are observed when comparing the magnitude spectra.

Figure 5.15a shows the contour line from the excited-state region of DTTCI in DMSO centered at 840 nm. Again, the 2000–5000-fs region of the contour line was fit to a sum of damped cosinusoids (figure 5.15b) and the rapidly-damped component was obtained as the difference between the contour line and the reverse-predicted model (figure 5.15c) and fit to a sum of damped cosinusoids (figure 5.15d). The sum of the damped-cosinusoidal fits over the 2000–5000-fs region of the contour line and the 0–1500-fs region of the difference signal almost completely describes the oscillatory character of the contour line, as shown in figure 5.16.

Figures 5.17a and 5.17b represent the best estimates for the spectra that would be retrieved by Fourier analysis from the long-lived and rapidly-damped oscillatory signals from DTTCI in DMSO using the fit parameters in tables 5.10–5.11. The sum of the magnitude spectra from the long-lived and rapidly-damped oscillatory signals is shown in figure 5.17c with the contribution from the rapidly-damped oscillatory signal shaded. As observed with DTTCI in DMSO in the ground state, significant contribution of the low-frequency region comes from the rapidly-damped oscillations and frequency shifts are observed when comparing the magnitude spectra.

Figure 5.18a shows the contour line from the excited-state region of DTTCI in acetonitrile centered at 840 nm. Again, the 2000–5000-fs region of the contour line was fit to a sum of damped cosinusoids (figure 5.18b) and the rapidly-damped component was

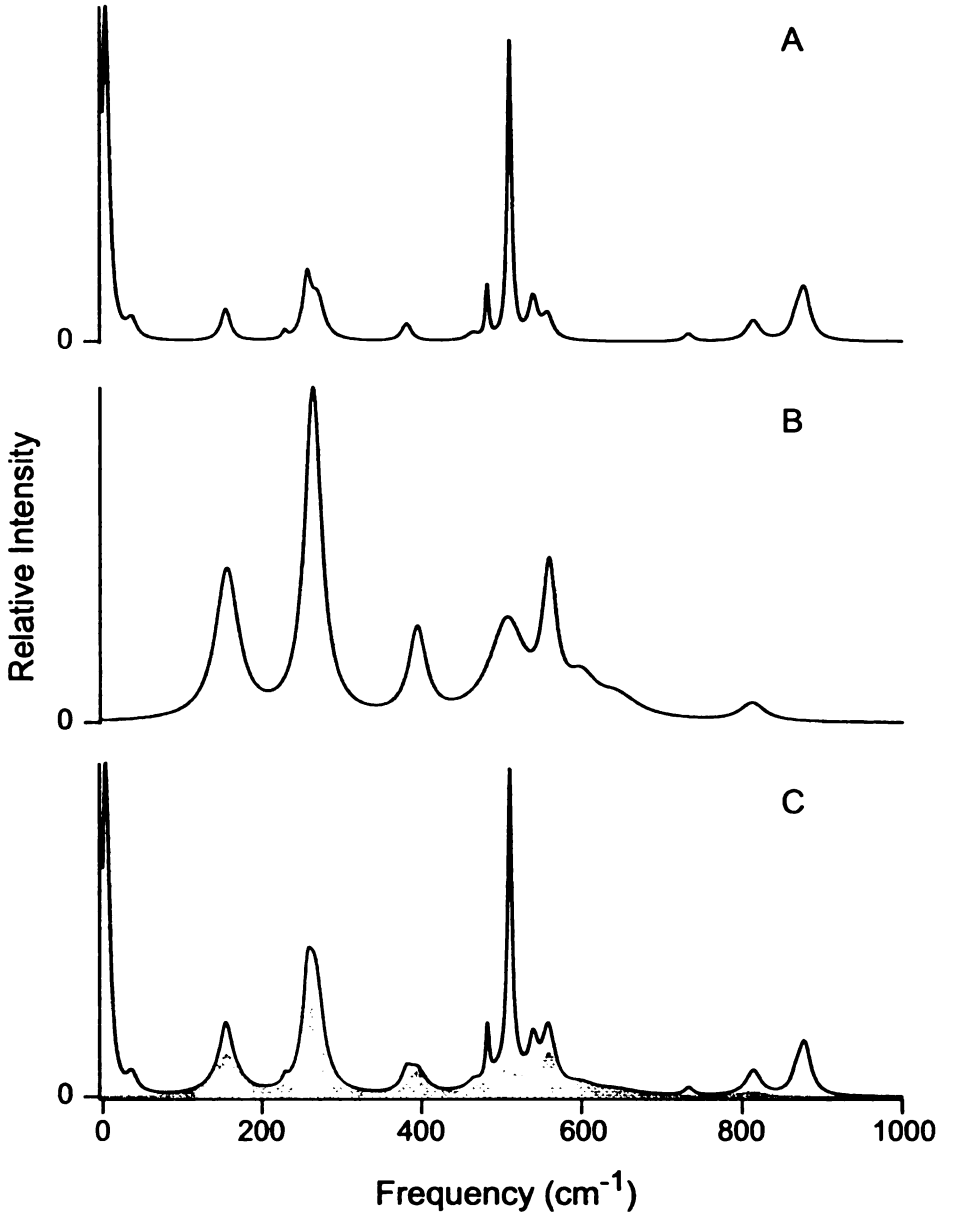

Figure 5.14. Magnitude spectra from the excited-state vibrational-coherence from DTTCI in methanol: a.) synthetic spectrum from the fitted 2000–5000-fs region; b.) synthetic spectrum from the fitted 0–1500-fs region of the difference signal; c.) sum of a and b with the shaded region showing contribution from b. Lorentzian lineshapes were generated from fit parameters (tables 5.8–5.9) using equation 5.2. Spectra are normalized to full scale for the most intense feature.

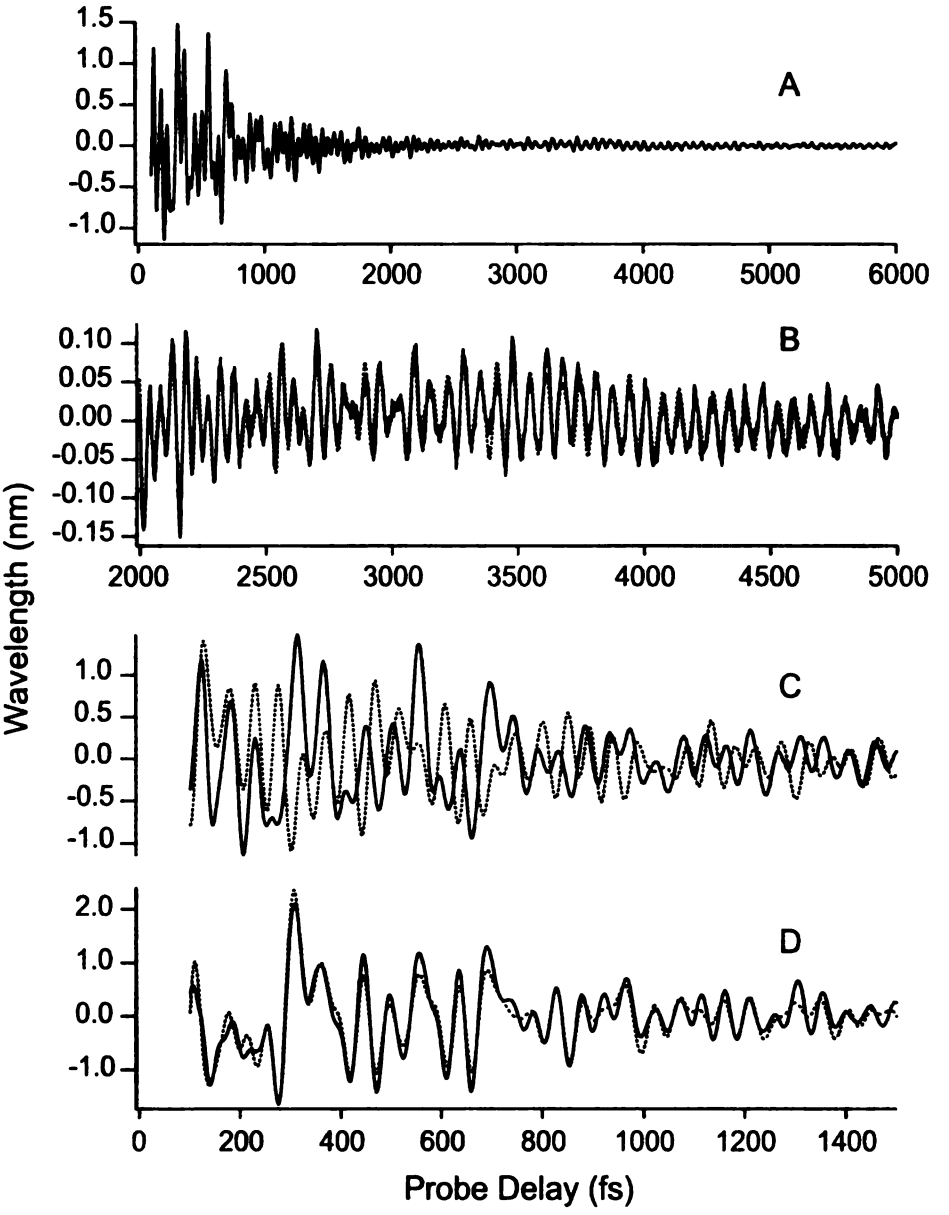

Figure 5.15. Isolation of rapidly-damped excited-state vibrational coherence from the dynamic-absorption contour observed at 840 nm from DTTCI in DMSO: a.) contour line over 0–6000 fs range; b.) expanded view over 2000–5000-fs region and a fit to a sum of damped cosinusoids (dotted line); c.) expanded view over 0–1500-fs region and reverse-predicted signal (dotted line); d.) difference between contour line and reverse-predicted signal and a fit to a sum of damped cosinusoids (dotted line).

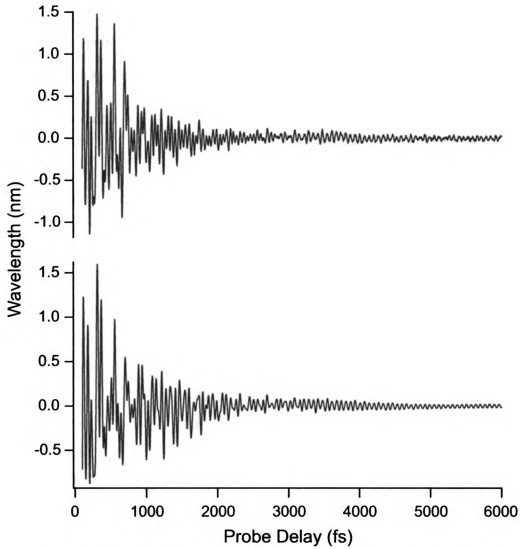

Figure 5.16. *Top*: Dynamic-absorption contour line observed at 840 nm from DTTCI in DMSO. *Bottom*: Sum of damped-cosinusoidal fits over 2000–5000-fs region of contour line (see figure 5.15b) and 0–1500-fs region of difference signal (see figure 5.15d).

Table 5.10. Frequencies, Relative Amplitudes, Damping Constants and Phases for Oscillatory Components Observed in the Excited-State Contour Line at 840 nm from the Dynamic-Absorption Spectrum of DTTCI in DMSO.

Frequency (cm^{-1})	Amplitude[a]	Damping Constant (fs)	Phase
10	1.06	1822	-0.56
100	7.30	475	-3.09
172	0.26	1890	0.37
193	0.19	2037	-0.62
272	3.26	760	0.78
439	0.19	1521	-1.65
499	2.36	1265	-0.10
509	1.25	1595	0.68
511	1.00	3654	3.10
543	2.81	805	-1.37
568	0.39	1440	0.50
700	10.22	794	-1.38
778	1.02	997	-1.36
820	2.12	856	-0.16
854	2.02	842	-0.23
872	0.25	1502	-0.57

[a] Relative to the amplitude of the 511-cm^{-1} component.

Table 5.11. Frequencies, Relative Amplitudes, and Damping Constants and Phases for Oscillatory Components Observed in the Excited-State Rapidly-Damped Vibrational Coherence at 840 nm from the Dynamic-Absorption Spectrum of DTTCI in DMSO.

Frequency (cm^{-1})	Amplitude[a]	Damping Constant (fs)	Phase
98	21.24	235	-0.13
171	9.33	640	-1.56
267	6.97	722	-2.61
404	6.40	448	-2.23
515	11.57	717	-1.47
700	8.09	920	2.45
825	4.16	373	-1.78
870	6.40	340	-2.12

[a] Relative to the amplitude of the 511-cm^{-1} component in Table 5.10.

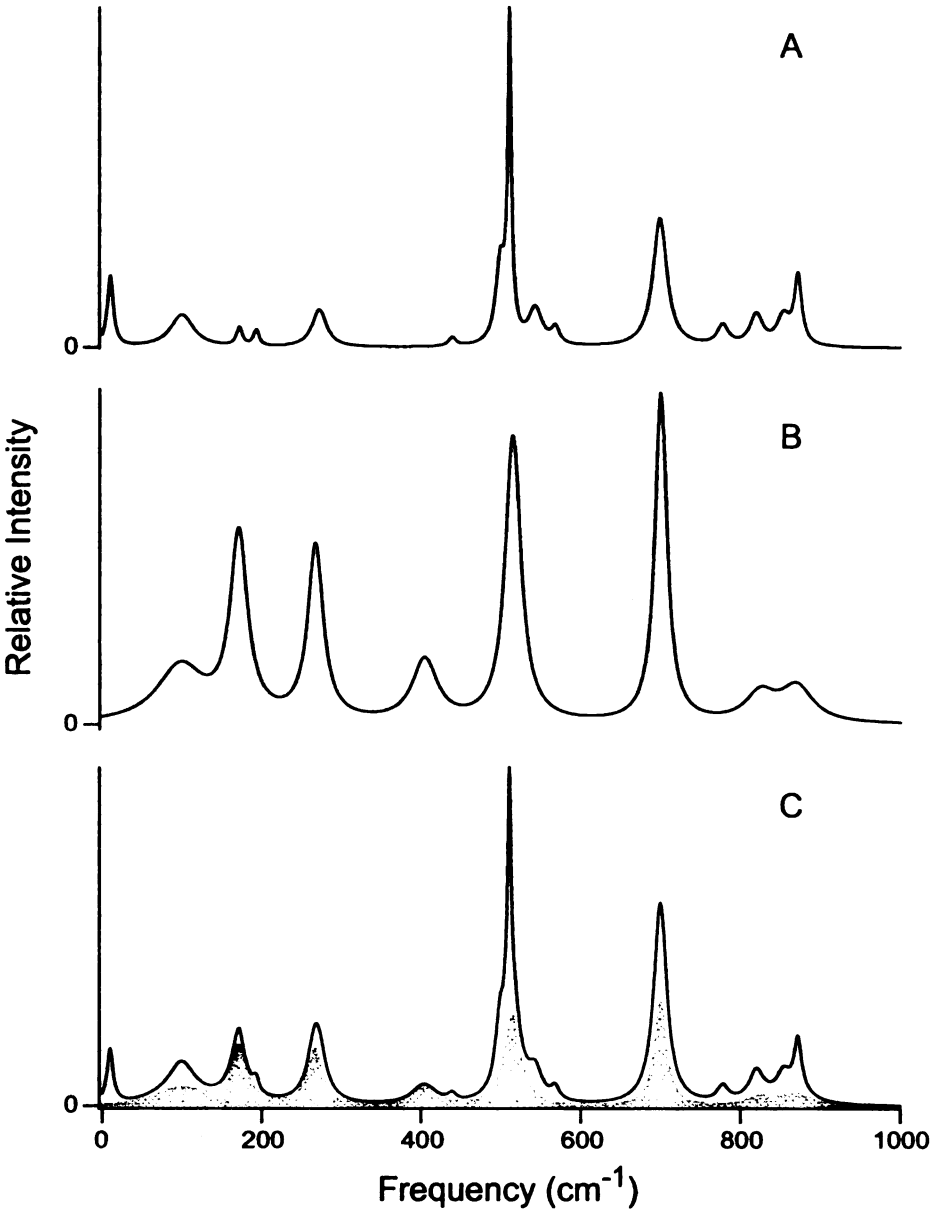

Figure 5.17. Magnitude spectra from the excited-state vibrational-coherence from DTTCI in DMSO: a.) synthetic spectrum from the fitted 2000–5000-fs region; b.) synthetic spectrum from the fitted 0–1500-fs region of the difference signal; c.) sum of a and b with the shaded region showing contribution from b. Lorentzian lineshapes were generated from fit parameters (tables 5.10–5.11) using equation 5.2. Spectra are normalized to full scale for the most intense feature.

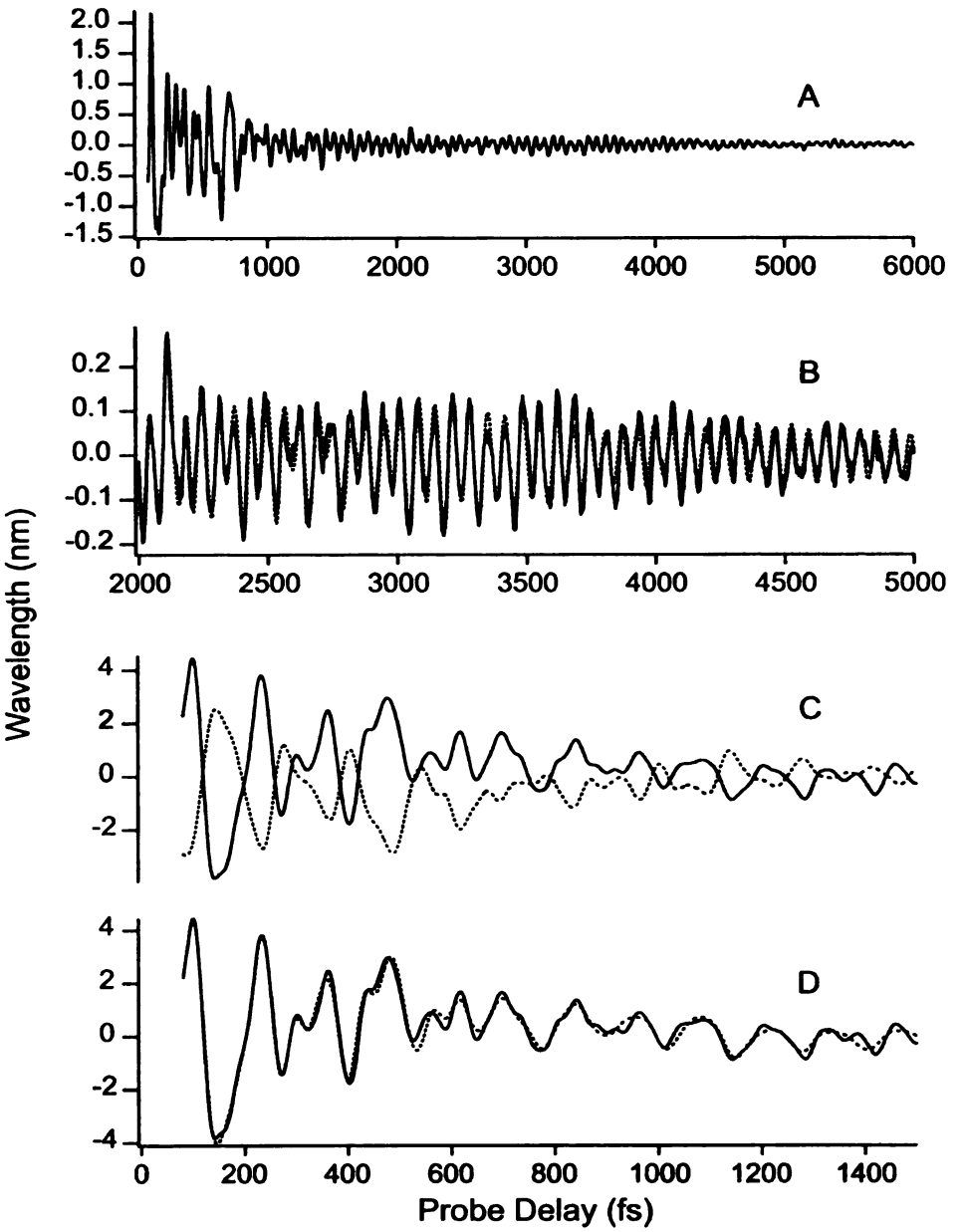

Figure 5.18. Isolation of rapidly-damped excited-state vibrational coherence from the dynamic-absorption contour observed at 840 nm from DTTCI in acetonitrile: a.) contour line over 0–6000 fs range; b.) expanded view over 2000–5000-fs region and a fit to a sum of damped cosinusoids (dotted line); c.) expanded view over 0–1500-fs region and reverse-predicted signal (dotted line); d.) difference between contour line and reverse-predicted signal and a fit to a sum of damped cosinusoids (dotted line).

obtained as the difference between the contour line and the reverse-predicted model (figure 5.18c) and fit to a sum of damped cosinusoids (figure 5.18d). The sum of the damped-cosinusoidal fits over the 2000–5000-fs region of the contour line and the 0–1500-fs region of the difference signal almost describes the oscillatory character of the contour line, as shown in figure 5.19.

Figures 5.20a and 5.20b represent the best estimates for the spectra that would be retrieved by Fourier analysis from the long-lived and rapidly-damped oscillatory signals from DTTCI in acetonitrile using the fit parameters in tables 5.12–5.13. The sum of the magnitude spectra from the long-lived and rapidly-damped oscillatory signals is shown in figure 5.20c with the contribution from the rapidly-damped oscillatory signal shaded. As observed with methanol, significant contribution of the low-frequency region comes from the rapidly-damped oscillations and frequency shifts are observed when comparing the magnitude spectra.

5.3 Discussion

5.3.1 Origin of Two Damping Time Scales

Two damping time scales are observed in both the ground- and excited-state vibrational coherence from DTTCI. This implies that there is not a structural change or time evolution of vibrational coherence due to reaction dynamics or photophysics. The difference in damping time scales is a result of interactions of the chromophore with solvent molecules.

The rapidly-damped vibrational components observed are thought to be intermolecular solvent–chromophore modes, which are shifted slightly from the slowly-

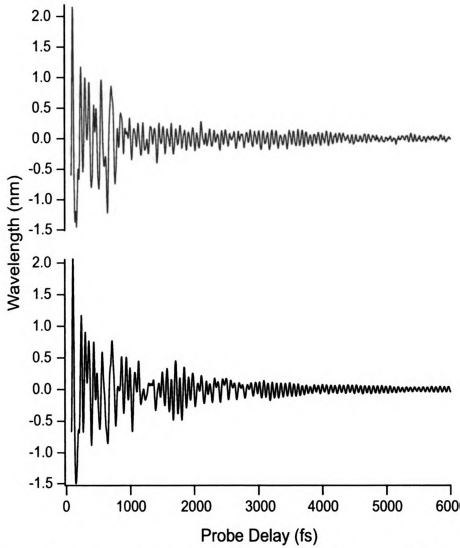

Figure 5.19. *Top*: Dynamic-absorption contour line observed at 840 nm from DTTCI in acetonitrile. *Bottom*: Sum of damped-cosinusoidal fits over 2000–5000-fs region of contour line (see figure 5.18b) and 0–1500-fs region of difference signal (see figure 5.18d).

Table 5.12. Frequencies, Relative Amplitudes, Damping Constants and Phases for Oscillatory Components Observed in the Excited-State Contour Line at 840 nm from the Dynamic-Absorption Spectrum of DTTCI in acetonitrile.

Frequency (cm^{-1})	Amplitude[a]	Damping Constant (fs)	Phase
16	11.00	561	-0.99
21	1.07	1142	-2.12
73	3.18	500	-2.17
171	6.61	516	-0.98
235	6.90	557	0.00
257	1.21	1236	-0.09
273	4.78	696	2.50
278	0.29	1363	2.70
467	1.81	1055	-0.62
484	1.97	1306	-1.94
509	1	3079	1.00
538	0.48	1706	2.80
558	0.44	1506	-1.81
730	0.78	639	-0.66
815	0.23	1318	2.72
854	0.28	987	0.70
884	0.20	859	-0.83

[a] Relative to the amplitude of the 509-cm^{-1} component.

Table 5.13. Frequencies, Relative Amplitudes, and Damping Constants and Phases for Oscillatory Components Observed in the Excited-State Rapidly-Damped Vibrational Coherence at 840 nm from the Dynamic-Absorption Spectrum of DTTCI in acetonitrile.

Frequency (cm^{-1})	Amplitude[a]	Damping Constant (fs)	Phase
17	11.16	549	2.08
67	1.19	1000	-0.29
165	7.80	440	2.07
238	3.07	746	-2.07
268	12.17	575	-1.54
492	4.30	436	2.10
531	6.64	346	-1.22
718	2.38	334	1.34

[a] Relative to the amplitude of the 509-cm^{-1} component in Table 5.12.

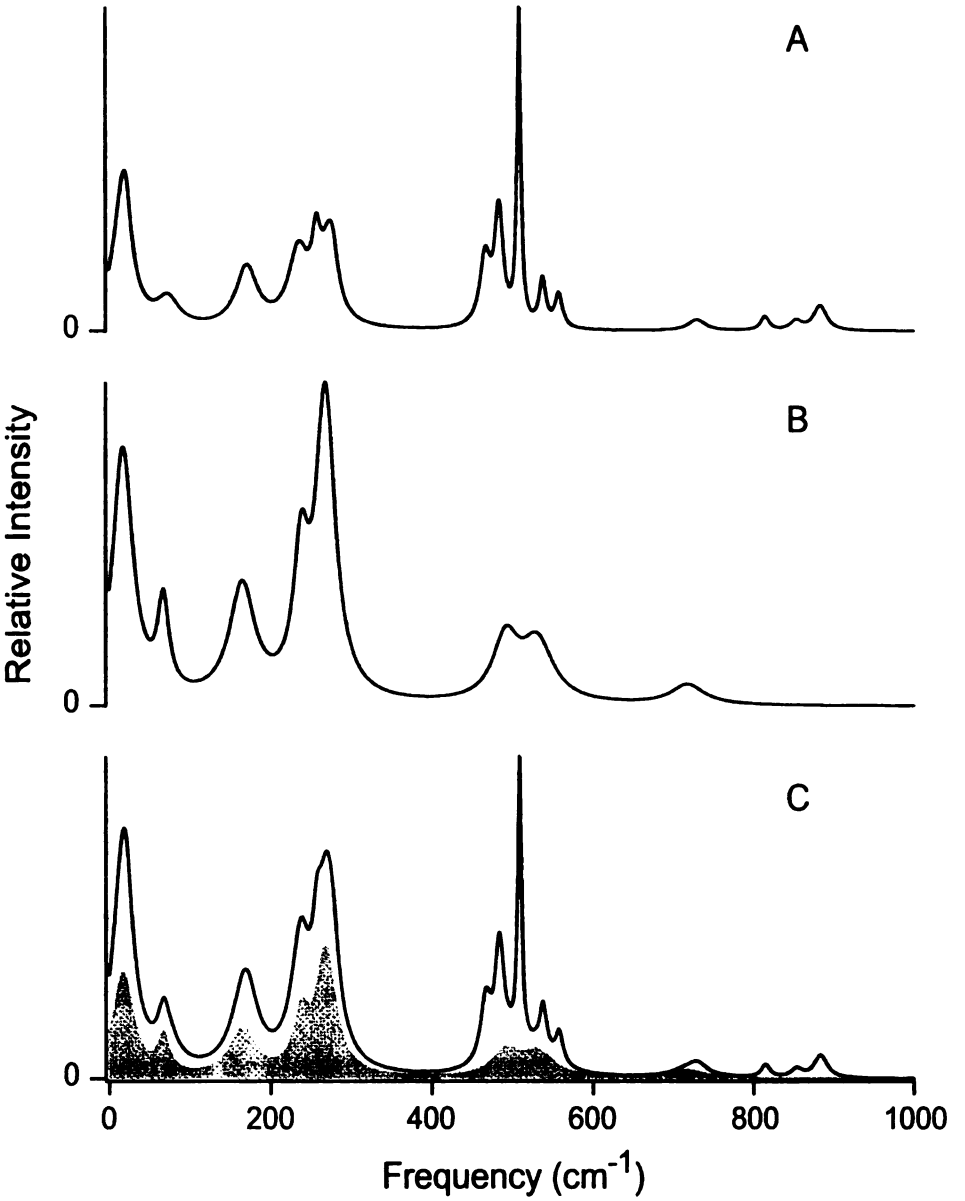

Figure 5.20. Magnitude spectra from the excited-state vibrational-coherence from DTTCI in acetonitrile: a.) synthetic spectrum from the fitted 2000–5000-fs region; b.) synthetic spectrum from the fitted 0–1500-fs region of the difference signal; c.) sum of a and b with the shaded region showing contribution from b. Lorentzian lineshapes were generated from fit parameters (tables 5.12–5.13) using equation 5.2. Spectra are normalized to full scale for the most intense feature.

damped components or the molecular modes of the chromophore. These rapidly-damped modes have lineshapes that are much broader when compared to the lineshapes of the slowly-damped components.

In addition to the rapidly-damped components, slowly-damped vibrational components are observed that are solvent dependent. In DMSO, an additional 700cm^{-1} mode is observed in both the ground and excited state which has similar damping times to the other slowly-damped molecular modes. These modes are thought to be strongly coupled solvent–chromophore modes. DTTCI is a charged species, the slowly-damped molecular modes observed are a result of a strong, ordered interaction between the charged chromophore and the polar solvent molecules.

5.3.2 Interactions of Electron Density with the Solvent Shell

The Mathies group has recorded resonance-Raman active modes of the solvated electron in water and alcohols.[1,2] The interaction of the electron with the first solvent shell causes a shift in a number of the solvent modes in addition to the intermolecular modes between the solvent and the electron.[1,2] We suggest that the observed rapidly-damped vibrational coherence in DTTCI is due to interaction of the delocalized π-electron density with the solvent shell.

5.3.3 Comparison of Ground- and Excited-State Vibrational Coherence

Comparison of the ground-state frequency spectra of DTTCI in methanol, DMSO and acetonitrile to the excited-state frequency spectra (see figures 5.21–5.23.) reveal additional modes appearing in the excited-state. We suggest that the $\pi \rightarrow \pi^*$ transition

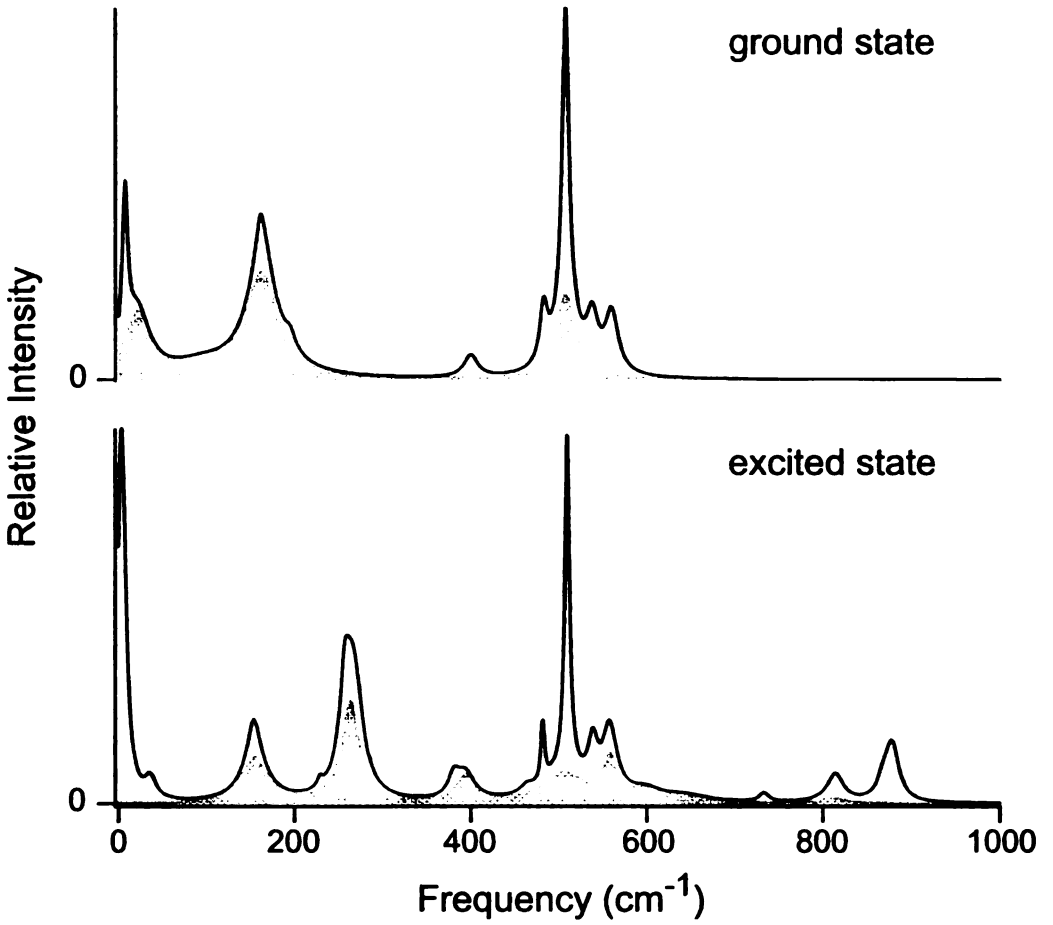

Figure 5.21. Comparison of the magnitude spectra from the ground-state (top) and excited-state (bottom) vibrational-coherence from DTTCI in methanol.

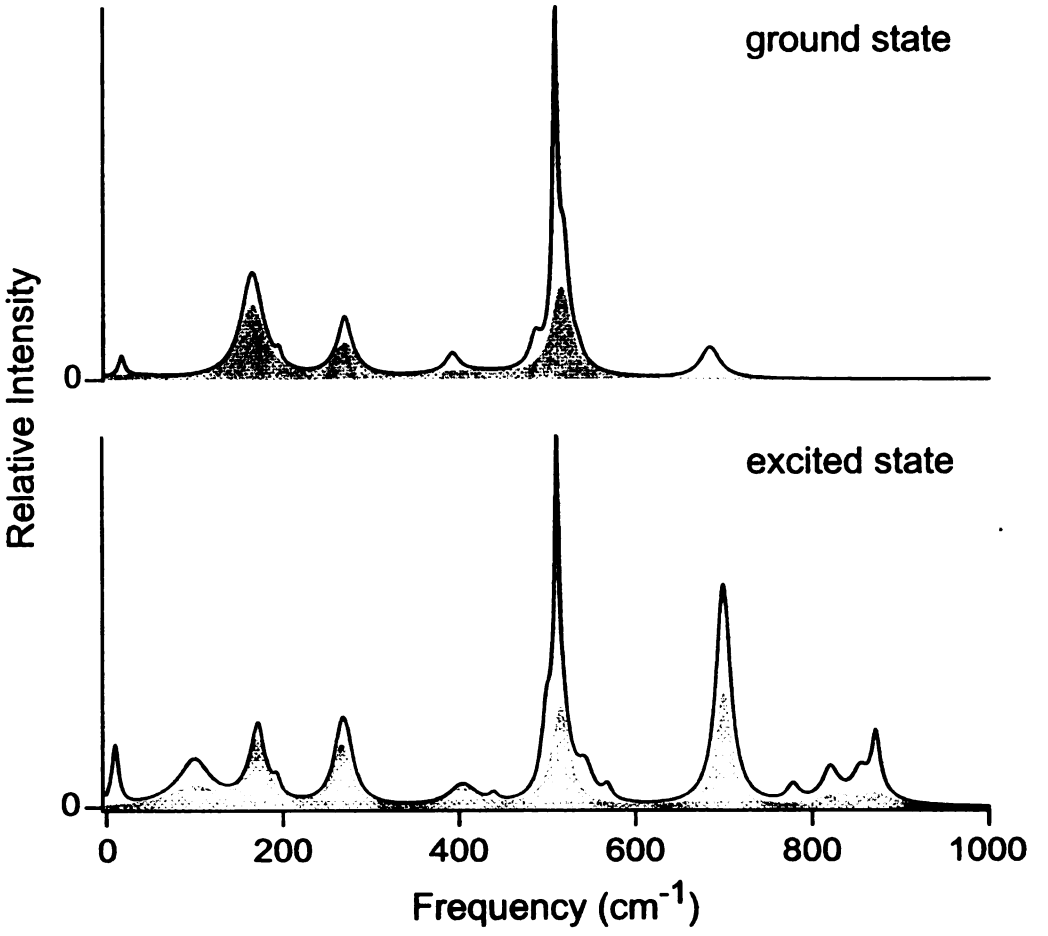

Figure 5.22. Comparison of the magnitude spectra from the ground-state (top) and excited-state (bottom) vibrational-coherence from DTTCI in DMSO.

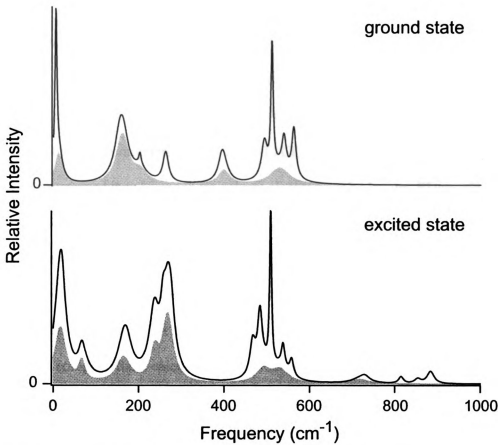

Figure 5.23. Comparison of the magnitude spectra from the ground-state (top) and excited-state (bottom) vibrational-coherence from DTTCI in acetonitrile.

causes the orbitals from the chromophore to extend further into the solvent creating an opportunity for more solvent–chromophore interactions. In the case of the solvated electron and a ground-to-excited transition, the electron has a round shape which changes to a p-orbital character.[10-14]

5.4 Future Work

Rapidly-damped vibrational coherence was also observed from IR144 in methanol. IR144 in other solvents should also be studied. A complete understanding of the interactions of the chromophore (IR144 and DTTCI) with solvent molecules is a difficult task. The structure of the chromophore-solvent system must be known. Electronic structure calculations and normal mode calculations can be used to assign vibrational modes of the chromophores. These calculations would also have to be done for the chromophore surrounded by a number of solvent molecules, simulating the first solvent shell. Because of the size of the molecules, these calculations are difficult. It might be beneficial to complete these calculations on a less-complicated model such as ethylene in a solvent shell.

The technique described in this work can be applied to biological systems of interest which have small Stokes shifts. Similar experiments on solvent–bacteriochlorophyll a interactions have been completed within the Beck group. These experiments have been extended to B777 and B820, as models for the photosynthetic reaction center. The chromophore–protein interactions in rhodopin would be another interesting system to study.

5.5 References

(1)Tauber, M. J.; Mathies, R. A. *Chem. Phys. Lett.* **2002**, *354*, 518–526.

(2)Tauber, M. J.; Mathies, R. A. *J. Am. Chem. Soc.* **2003**, *125*, 1394–1402.

(3)Shelly, K. R.; Carson, E. A.; Beck, W. F. *J. Am. Chem. Soc.* **2003**, *125*, 11810–11811.

(4)Carson, E. A.; Diffey, W. M.; Shelly, K. R.; Lampa-Pastirk, S.; Dillman, K. L.; Schleicher, J. M.; Beck, W. F. *J. Phys. Chem. A* **2004**, *108*, 1489–1500.

(5)Cantor, C. R.; Schimmel, P. R. *Biophysical Chemistry. Part II: Techniques for the Study of Biological Structure and Function*; W. H. Freeman and Company: San Francisco, 1980.

(6)Lakowicz, J. R. *Principles of Fluorescence Spectroscopy*; Second ed.; Kluwer Academic/Plenum Publishers: New York, 1999.

(7)Siano, D. B.; Metzler, D. E. *J. Chem. Phys.* **1969**, *51*, 1856–1861.

(8)Lampa-Pastirk, S.; Beck, W. F. *J. Phys. Chem. B* **2004**, *108*, 12602–12607.

(9)McHale, J. L. *Molecular Spectroscopy*; Prentice Hall: Upper Saddle River, New Jersey, 1999.

(10)Alfano, J. C.; Walhout, P. K.; Kimura, Y.; Barbara, P. F. *J. Chem. Phys.* **1993**, *98*, 5996–5998.

(11)Kimura, Y.; Alfano, J. C.; Walhout, P. K.; Barbara, P. F. *J. Phys. Chem.* **1994**, *98*, 3450–3458.

(12)Reid, P. J.; Silva, C.; Walhout, P. K.; Barbara, P. F. *Chem. Phys. Lett.* **1994**, *228*, 658–664.

(13)Walhout, P. K.; Alfano, J. C.; Kimura, Y.; Silva, C.; Reid, P. J.; Barbara, P. F. *Chem. Phys. Lett.* **1995**, *232*, 135–140.

(14)Silva, C.; Walhout, P. K.; Reid, P. J.; Barbara, P. F. *J. Phys. Chem. A* **1998**, *102*, 5701–5707.